Approval Sheet

Title of dissertation:	PHYSICAL CONDITIONS IN THE X-RAY EMISSION-LINE GAS IN THE SEYFERT 2 GALAXY NGC 1068
Name of Candidate:	Neetika Sharma Doctor of Philosophy, 2016
Dissertation and Abstract Approved:	Professor Jane Turner Department of Physics

Date Approved: 04/20/2016

ABSTRACT

Title of dissertation: PHYSICAL CONDITIONS IN THE X-RAY EMISSION-LINE GAS IN THE SEYFERT 2 GALAXY NGC 1068

Neetika Sharma, Doctor of Philosophy, 2016

Dissertation directed by: Professor T. J. Turner
Department of Physics

Active Galactic Nuclei (AGN) reside in the centers of many (10%) galaxies. The nuclear spectra exhibit a broad (from radio to gamma-rays) non-stellar continuum which exceeds the luminosity of the host. AGN are thought to be powered by accretion of matter onto a supermassive black hole (BH$\sim 10^6$-10^9 times the mass of the Sun). Since this activity takes place in a relatively small region ($<<$ 3 light years), the central engine of even the closest AGN cannot be imaged directly with current technology. Nevertheless, spectroscopic observations can help us constrain the conditions of the gas very close to the BH.

The scientific goal of my thesis is to examine the physical conditions in the circumnuclear regions of the Seyfert 2 galaxy NGC 1068. The soft X-ray spectrum comprises a multitude of emission lines including those of C, N, O, Ne, Mg, that arise in gas that is spatially extended over $\sim$ 1000 light years. Radiative recombination continuum widths indicate the gas is photoionized and I model it finding a two-zone solution with unusual abundances attributed to the star formation history of the galaxy. Also of interest are the Fe K complex of emission lines, spanning neutral to

highly ionized gas. These lines are produced in a separate, clumpy gas component, much closer to the BH.

PHYSICAL CONDITIONS IN THE X-RAY EMISSION-LINE GAS IN THE SEYFERT 2 GALAXY NGC 1068

by

Neetika Sharma

Dissertation submitted to the Faculty of the Graduate School of the University of Maryland, Baltimore County in partial fulfillment of the requirements for the degree of Doctor of Philosophy
2016

Advisory Committee:
Dr. Jane Turner, Chair/Advisor
Dr. Steve Kraemer
Dr. Kevin McCann
Dr. Markos Georganopoulos
Dr. Terrance Worchesky

Dedication

To
Srila Prabhupada
&
HH Bhakti Rasamrita Swami Maharaj

Acknowledgments

I am indebted to a great number of people without whom this dissertation would not have been possible.

First and foremost, I would like to extend my sincerest gratitude to my thesis advisor, Dr. Jane Turner, for her generous guidance, extreme patience, persistent support, and expertise in the field. I am grateful for her valuable comments on numerous revisions of this manuscript. It was a great pleasure working with her.

I would like to extend my deepest appreciation to Dr. Steve Kraemer for his precious time, advice and immense interest in my topic of research.

I owe my deepest thanks to Dr. Ian George for his invaluable years of mentorship.

I would like to thank Dr. Kevin McCann, Dr. Markos Georganopoulos and Dr. Terrance Worchesky for agreeing to serve on my thesis committee.

My special thanks to Dr. Kenji Hamaguchi, my first postdoc mentor, and Dr. Todd Pittman, the graduate program director.

I would like to extend my heartfelt gratitude to my family. Particularly, to my uncle, Naresh Sharma, my aunt, Anita Sharma, and my sister, Vishakha Sharma. Without their emotional and moral support, it was very hard to thrive in my doctoral work. To my friends, Amanda Dotson, Malachi Tatum and Joel Coley, thanks for the great company during all those years at UMBC. I will be remiss not to thank Lynne Griffith, Jennifer Salmi, Marsha Scott, Stacey Tignall, Paul Ciotta, and the UMBC Physics department.

I would like to acknowledge financial support from the Center for Research and Exploration in Space Science and Technology (CRESST).

Lastly, and most of all, I would like to thank the devotees of Lord Sri Sri Radha Madanmohan and His associates, for their unlimited prayers and blessings !

Table of Contents

List of Tables

List of Figures

List of Symbols

E	energy
T	temperature
k	Boltzmann constant
eV	electron volt
σ_{T}	Thomson cross section
c	speed of light
n	gas density
U	ionization parameter
$\mathrm{N_H}$	column density
C_f	Covering factor
$\mathrm{L_E}$	Eddington luminosity
$\mathrm{M}_\odot$	solar mass
$\mathrm{L}_\odot$	solar luminosity
$\dot{\mathrm{M}}$	mass loss rate
$\mathrm{R_g}$	gravitational radius
$\mathrm{R_s}$	Schwarzschild radius
$\mathrm{m_p}$	proton mass
μ	reduced mass
i	ionization state
A	atomic state
kpc	kiloparsec
Z	atomic number

List of Abbreviations

AGN	Active Galactic Nuclei
ASCA	Advanced Satellite for Cosmology and Astrophysics
AU	Astronomical Units
ACIS	Advanced CCD Imaging Spectrometer
ANS	Astronomical Netherlands Satellite
BH	Black hole
BLR	Broad Line Region
CCD	Charge-Coupled Device
EW	Equivalent width
ESA	European Space Agency
EXOSAT	European X-ray Observing Satellite
EPIC	European Photon Imaging Camera
FITS	Flexible Image Transport System
FWHM	Full Width at Half Maximum
FPA	Focal Plane Arrays
FPM	Focal Plane Module
GEMS	Gravity and Extreme Magnetism Small Explorer (GEMS)
GTI	Good Time Intervals
HEAO	High Energy Astronomy Observatory
HRC	High Resolution Camera
HST	Hubble Space Telescope
HETG	High Energy Transmission Gratings
HEG	High Energy Gratings
HXD	Hard X-ray Detector
HRMA	High Resolution Mirror Assembly
IPAC	Infrared Processing and Analysis Center
JAXA	Japanese Scientific Space Agency
LETG	Low Energy Transmission Gratings
MEG	Medium Energy Gratings
MOS	Metal-Oxide Semi-conductors

List of Abbreviations cont.

NLR	Narrow Line Region
NASA	National Aeronautics and Space Administration
NIST	National Institute of Standards and Technology
NED	NASA/IPAC Extragalactic Database
ODF	Observations Data Files
OSO	Orbiting Solar Observatory
PHA	Pulse Height Analyzer
PI	Pulse Invariant
PPS	Pipeline Processing System
RGS	Reflection Grating Spectrometers
RFC	RGS Focal Camera
RRC	Radiative Recombination Continua
SED	Spectral Energy Distribution
SOC	Science Operation Center
SAS	Science Analysis System
SXS	Soft X-ray Spectrometer
VLTI	Very Large Telescope Interferometer
XMM	X-ray Multi Mirror
XNLR	X-ray Narrow Line Region
XIS	X-ray Imaging Spectrometers

Chapter 1: Introduction

1.1 Setting the scene

A supermassive black hole (SMBH, of mass 10^6 - 10^9 $M_\odot$[1], Ho et al. 2000) lies at the center of virtually every galaxy (e.g. Ferrarese & Ford 2005; Kormendy & Richstone 1995), including our own Milky Way (Schödel et al., 2002). Most of these are in a dormant state. However, in a census of galaxy characteristics, a significant fraction ($> 10\%$, Maiolino & Rieke 1995) of galaxies is clearly different from "normal" spiral and elliptical galaxies (see Figure 1.1). Specifically the centers of these galaxies ("active galactic nuclei", hereafter AGN) are much more luminous than normal galaxies (and in most cases far out-shine the host galaxy). For instance, the bolometric luminosity (summed over the entire spectral energy distribution) of our Milky Way integrated out to a radius of 30 kpc is 10^{43} ergs s^{-1}, primarily from stars, (e.g. Binney & Merrifield 1998), as compared to AGN that emit a luminosity within the range 10^{43} - 10^{47} ergs s^{-1} from a very small volume i.e. $<<1$ pc^3 (e.g. Krolik 1999, references therein).

An 'active' black hole (BH) is powered by accretion of matter, probably from the host galaxy. Numerical models show that this infalling material forms a disk,

[1] The mass of the Sun, $M_\odot = 2\times10^{33}$ g

the so-called ‘accretion disk’. Some of the accreting material is pushed back out into the host galaxy (see later for details). This ‘returned material’ may be a significant part of the also called “AGN feedback”, and may play a very important role in the co-evolution of galaxies and their SMBHs. The production of the energy, and the matter/energy flow between the galaxy nucleus and host are key to understanding the processes at work in extreme physical conditions, and the growth of structure in the Universe (e.g. Jogee 2006). However, the birth and growth of these BHs in the Universe and their links to the host galaxy are not fully understood. Neither are the details of their fuel supply, and why some BHs are “active” while others are not.

AGN have been studied at all wavelengths of the electromagnetic spectrum, from radio to gamma-rays. A significant fraction (5–40%) of the total bolometric luminosity is produced in X-rays (Ward et al., 1987). Furthermore, most of the X-ray emission is produced in the regions very close to the central BH (within a few gravitational radii, r_g), characterized by very high temperatures and luminosities, whereas other emission e.g. optical radiation is produced at larger distances ($\sim 10^5$ times larger than the X-ray emitting region) from the BH. Given their origin very close to the central SMBH, and the fact they can penetrate large column densities of material, X-ray data provide the clearest view of physical processes and the conditions of gas very close to the central black hole.

1.2 The History of AGN

1.2.1 Earliest discoveries

It has been more than a hundred years since "spiral nebulae" were first recognized to exhibit a peculiar point-like source at their center (Fath, 1909). Subsequent observations revealed that the spectra of many sources contain strong emission lines not seen in the composite stellar spectra of most other "normal galaxies". The origin of these lines remained a mystery for many years. Indeed, it was not until 1927 that the brightest two of these lines (at wavelengths of 5007Å, 4959Å) were identified in planetary nebula, with electron transitions within twice ionized oxygen (hereafter [O III], Bowen 1927). The reason behind the long delay in the identification of these 'strange' lines was that they are not the result of traditional electric-dipole ("permitted") transitions as an electron in an excited oxygen ion, but rather the result of non-dipole ("forbidden") de-excitations of electrons. These are evident in very low density gas (e.g. number density $<< 10^6$ cm^{-3}). Such low densities are barely achievable in the laboratory today in ultra-high vacuum systems.

In 1943, in a small survey of galaxies, Carl Seyfert discovered a class of objects in which these similar kinds of emission lines were observed (Seyfert, 1943). These objects are now commonly referred to as Seyfert Galaxies and are considered a subclass of a broader range of objects known as AGN. However, it was not until the 1960s (when X-ray astronomy started flourishing) that Seyfert Galaxies and other AGN became the major area of study which continues to this day.

1.3 Classification of AGN

As stated above, strong emission lines are prominent features of AGN in the optical band. Even in the earliest observations of AGN it was realized that these lines had significant widths which, when interpreted as due to Doppler broadening, correspond to material moving at speeds of hundreds to thousands of kilometers per seconds. AGN can be grouped into two classes, those with strong "broad" ($>$ 1000 km s^{-1}) and "narrow" ($<$ 1000 km s^{-1}) permitted emission lines, and narrow forbidden emission lines, and those with only narrow permitted and forbidden emission lines. The regions responsible for the line emission with these two different kinematic characteristics are traditionally known as the broad- and narrow-line regions (usually referred to as the BLR and NLR respectively). AGN showing the broad lines are classified as "Type 1" and AGN showing only the narrow lines are classified as "Type 2". In the case of Seyfert galaxies these correspond to "Seyfert 1s" and "Seyfert 2s", respectively, (e.g. Antonucci 1993). Detailed spectral analysis indicates the gas responsible for these two types of lines not only has different kinematical properties but also has different gas densities. Forbidden line emission is hardly observed in the BLR due to the much higher electron densities for collisional excitation (e.g. Osterbrock 1985). As described below, the ionization state of the material in both regions is thought to be powered by the intense radiation field associated with the "central engine" of the AGN.

Other components of the circumnuclear material may include so-called winds, i.e. mass outflows which have signatures in X-ray, UV and optical spectra (e.g.

Crenshaw et al. 2003; Turner & Miller 2009) and a dusty molecular “torus” thought to exist at a larger radius than the X-ray reprocessing gas (see section 1.4). [Some AGN also contain powerful radio jets of outflowing relativistic particles, but as these are not a significant component of Seyfert galaxies and they are not considered further here].

1.4 The Unified Model of AGN

In the mid 1980s, it was realized that the different observational characteristics exhibited by different subclasses of AGN could be explained by all objects having similar structures within the innermost regions but viewed from different directions. This is the basis of “The Unified Model” (Miller & Antonucci, 1983) as illustrated in Figure 1.2. (It should be noted that in this figure the circumnuclear regions are not drawn to scale). The basic premise is that some regions such as the BLR and the continuum source can be obscured if our direct line-of-sight is close to the equatorial plane defined by the torus while others, such as the NLR, are not. This is the viewpoint for the artist’s impression shown in Figure 1.2, in which the BLR is hidden by the torus which is optically thick. We would classify such AGN as Type 2 objects. In contrast, if our line-of-sight is much closer to the normal to this plane then there is little obscuration. Thus, emission from both the BLR and NLR can be observed, such AGN would be classified as Type 1 objects. These two cases are often referred to as “edge-on” and “face-on” objects, respectively. As noted above, the effects of the intense radiation field of the central source can be seen via its effect on material thought to exist on a size-scale of hundreds of light seconds. The BLR is thought to exist $\sim$ 10-100 light days (Netzer & Peterson, 1997) from the continuum source. The width of the broad optical lines is thought to be indicative of relatively high orbital velocities for the emitting gas clouds, which implies they exist relatively close to the active nucleus. From consideration of the broad-lines observed, and their relative intensities, it is generally believed these BLR clouds have densities $\sim 10^8$ cm^{-3} (which is determined from the suppression of forbidden lines).

The torus remains poorly understood. Indeed, it is probably not a single structure at all -rather it may be a toroidal distribution of gas clouds through which the reprocessed gas can be observed (see chapter 6 for more details). The main requirement for a torus is that there is dust present to obscure the BLR emission from edge-on observers. The inner boundary of this toroidal region therefore can be estimated from the dust sublimation radius. Given the luminosity of the central engine in most AGN, that inner boundary lies within the range 1-10 pc (Gallimore et al., 2006).

The NLR extends typically over a size scale of hundreds of parsecs (Kraemer & Crenshaw, 2000), however, in some cases the gas extends very far from the nucleus ($\sim$ 4 kiloparsec away), having much narrower emission lines of FWHM ≤ 50 km s^{-1} and is referred to as the extended narrow line region (ENLR, Crenshaw et al. 2010; Unger et al. 1987). This makes the NLR the only structure which can be (just) spatially resolved in the nearest AGN (e.g. the NLR of NGC 1068 has an extent of $\sim 2''$ compared to the resolution of HST/STIS of $0.05''$ at a waveband of 1200-10000

Å, Crenshaw & Kraemer 2000). At such distances, the typical orbital speeds of clouds would be lower (consistent with the observed lines widths of FWHM a few hundred km s^{-1}) and, as noted previously, the existence of forbidden lines constrains the gas density to $\leq 10^6$ cm^{-3}.

1.5 The Basic Physics of AGN

1.5.1 A few key features of a black hole

1. Schwarzschild radius (R_s): It represents the mathematical surface of a non-rotating BH or in other words, the outer horizon where one can witness the occurrence of an event, it is also called an event horizon. Material that falls inside this event horizon can not escape and is trapped indefinitely. The Schwarzschild radius of a body of mass M is defined as $R_s = \frac{2GM}{c^2}$, where 'G' is the Gravitational Constant, 'M' the mss of the black hole and 'c' the speed of light. This expression can be derived by equating the gravitational potential energy to the kinetic energy of an escaping test particle of velocity c (speed of light) and mass m. This Schwarzschild solution is appropriate for the simplest, non-rotating black hole which is defined by a single parameter, mass M. The Kerr metric, using the field equations of general relativity, provides a solution for rotating black holes, characterized by angular momentum, in addition to mass M. The innermost stable circular orbit of the Kerr black hole is smaller ($1.235r_g$) than that of the Schwarzschild black hole ($6r_g$), and so emission can be seen from closer to the black hole.

2. Efficiency: There has been tremendous progress in understanding the phys-

ical characteristics and processes at work in AGN since their discovery in 1905. The source of the prodigious amount of energy released (billions times that of the Sun, $L_\odot$) in AGN is believed to be the accretion of matter onto a SMBH - "the central engine". The basic idea is that the gravitational potential energy lost by the infalling material is converted into kinetic energy and ultimately radiated into photons. This process is thought to take place in a flattened accretion disk surrounding the BH that forms due to the initial angular momentum of the infalling material. However, the exact details of the processes involved (in particular the "viscous drag" experienced by the particles and transfer of angular momentum between the particles) are still not fully understood.

Accretion is the most efficient way to produce radiation from the infalling matter. In fact, the large and persistent nuclear luminosities can only be explained by accretion onto a SMBH. The luminosity ($L_{acc} = \eta \dot{M} c^2$) produced depends on the efficiency (η) and the accretion rate ($\dot{M}$). An efficiency of 10% (a standard estimate e.g. Yu & Tremaine 2002) of the rest mass energy being converted into photons is much larger than the energy released during nuclear fusion that is only 0.7% of the rest mass energy.

3. The Eddington luminosity: There exists a maximum luminosity allowed for a given mass which is powered by steady state accretion. Assuming a spherically symmetrical accretion around the central source of mass 'M' emitting luminosity 'L', the accreting material to be fully ionized, mainly hydrogen, the net radiation force acting on the electron-proton pairs at a distance 'r' is given by $f_{rad} = \frac{L\sigma_T}{4\pi r^2 c}$, where σ_T is the Thomson cross section. The radiation can push out the electron-proton

Figure 1.1: At left is the optical image of a 'normal' galaxy (face-on view) and at right is the multi-wavelength image of the 'active' galaxy Centaurus A (edge-on view). Tremendous radiation emerging from the center (at right) can be seen outshining the host galaxy. Image credit: HST NASA/ESA.

pairs against the total gravitational force $f_g = \frac{GMm_p}{r^2}$ as long as $f_g > f_{rad}$. In other words, the net inward force on an electron-proton pair is $f_g - f_{rad}$ which vanishes at the Eddington limit, $L_{Edd} = \frac{4\pi GMm_pc}{\sigma_T} \simeq 1.5 \times 10^{38}$ $(M/M_\odot)$ erg s^{-1}, where m_p is the proton mass. The outward radiation pressure would exceed the inward gravitational attraction at the luminosities greater than L_{Edd} and accretion would come to an end.

In this thesis, I concentrate on the detailed analysis and modeling of the X-ray emitting gas in the circumnuclear regions of a bright, nearby type 2 AGN NGC 1068 whose NLR gas can be resolved with the high-resolution space-based telescopes. Probing the NLR gas in the X-ray band provides constraints on the gas condition and, indirectly, on the underlying physics of the emission mechanism.

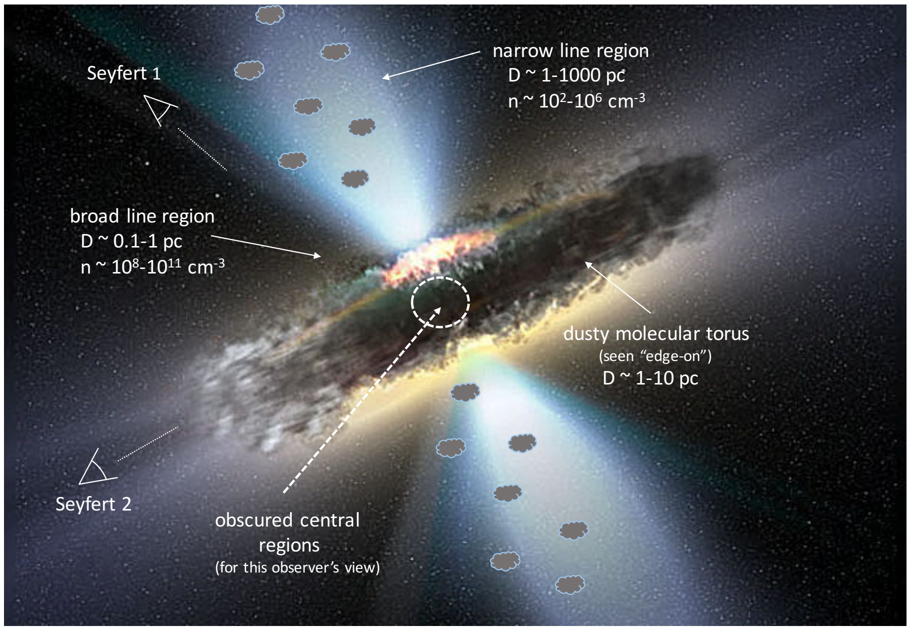

Figure 1.2: An artistic conception of the unified structure of AGN from the viewpoint of an observer in the equatorial plane of the doughnut-shaped obscuring "torus". The torus itself is shown as the dark band of nebulous material diagonally crossing the sketch. From this edge-on view the torus obscures the central black hole and innermost circumnuclear regions such as the accretion disk and broad line region (BLR) in most wavebands. However, the radiation field from the central engine is still evident due to its interaction with material above and below the torus such as that in the ionization cone of the narrow line region (NLR). These cones are the smallest structures able to be resolved in even the nearest objects using the current technology. The AGN viewed from this perspective would be classified as a type 2 object. The topic of this thesis is a study of NGC 1068, which is a type 2 object. The inner regions are visible to an observer well above the equatorial plane of the torus and would be classified as a type 1 object. Adapted from an image courtesy of APOD NASA/ESA.

Chapter 2: X-ray astronomy and the Instrumentation

2.1 Introduction to X-ray astronomy

X-ray astronomy is a branch of high-energy astrophysics dealing with the phenomena of very high energy processes taking place in the Universe. Earth's atmosphere absorbs X-rays, hence X-ray observations of astronomical objects must be performed from the space-based observatories, rockets and balloons.

An X-ray photon carries much higher energy than an optical photon (by a factor of 1000 or more), thus the conventional normal incidence reflecting mirrors cannot be used to focus X-rays since they can easily penetrate or be absorbed by such materials. However, X-rays can reflect if they strike a smooth surface at small grazing angles, just as a stone can be bounced off the surface of water instead of being dropped straight in. The critical angle, below which total external reflection occurs for X-rays, varies as $\sqrt{\mathrm{Z}}/\mathrm{E}$, where Z is the atomic number and E is the energy of the incoming X-ray photon. Thus, the angle of reflection has to be smaller for the higher energy X-rays, and high Z materials (gold, platinum and iridium) are good reflectors for X-rays of energy 0.1-10 keV. After reflecting off the mirrors, X-rays are registered on a detector to obtain as much information as possible e.g., the position of the X-ray photons (in detector or sky coordinates), their energy ("pulse height analyzer" PHA or "pulse invariant" PI 'channel', discrete energy bin), their arrival time, etc. At the same time, X-rays from other sources e.g. charged-particle background, X-ray diffuse background, cosmic rays, etc., are also registered on the detector which contaminate the X-ray data of the source of interest. These unwanted X-ray events ('noise') must be screened out before analyzing the X-ray data in order to understand the properties of the target of interest, and to maximize the ratio of signal over noise (S/N).

Part of the X-ray data analysis process requires consideration of the instrument calibration, and calibrated quantities may or may not be dependent upon time, the former requiring observation-dependent calculations to be performed as part of the data processing. Some key calibration quantities, which are useful for the analysis described in this thesis, are: the point spread function of an instrument which describes the spread of photons on the detector pixels and determines the shape and size of the image, the response matrix file (RMF) which parametrizes the probability that a photon of a given energy is registered in a channel and the ancillary response file (ARF) which describes the effective area of a telescope and the focal plane instrument as a function of photon energy.

2.2 History of X-ray astronomy

X-ray astronomy had its genesis in the aftermath of World War II, when the Naval Research Laboratory aimed to detect radio waves above the atmosphere by flying sounding rockets carrying radiation detectors. It was discovered then that the radio waves were being disrupted by high-energy radiation produced by solar flares (Friedman et al., 1951). Subsequently, X-ray emission from the solar corona was studied in detail. In 1962, Riccardo Giacconi and a team at American Science and Engineering flew a rocket to study X-ray fluorescence from the moon and serendipitously discovered an extra-solar X-ray source in the Scorpious region, later named Sco X-I (a binary with a neutron star, Giacconi et al. 1962). Following this, non-solar X-rays were detected from supernova remnants and many other binary sources.

2.2.1 Missions prior to 1997

The first earth-orbiting satellite devoted to X-ray astronomy, *Uhuru*, was launched in 1970. In its All Sky Survey, *Uhuru* (1970 - 1973) observed hundreds of X-ray emitting celestial objects, over the energy band of 2 - 20 keV. In its lifetime, *Uhuru* detected over 300 individual sources, mostly galactic binaries and about a dozen AGN (Forman et al., 1978).

In the 1970s, X-ray astronomy flourished with results from more X-ray satellites: *Copernicus*, *Ariel-V* (from the UK), Astronomical Netherlands Satellite (*ANS*), Observing Solar Observatory (*OSO-8*) e.g. Tucker et al. (1973). The High Energy Astronomy Observatory 1 (*HEAO-1*), launched by NASA in 1977, was the first of a series of missions dedicated to a detailed study of X-ray sources and the X-ray background, surveyed in the 0.2 -10 MeV range. In the X-ray survey, *HEAO-1* detected 22 emission-line AGN which exhibited strong Fe II emission in their optical spectra (Remillard et al., 1993). After the end of the *HEAO-1* mission in 1979, the second of this series of large scientific payloads, *HEAO-2*, renamed *The Einstein Observatory* in honor of his centennial, provided the first astronomical satellite with X-ray imaging capability, covering an energy band of 0.2 -20 keV.

The Einstein Observatory brought about a big revolution in X-ray astronomy by using the combination of an X-ray telescope and an imaging proportional counter. *Einstein* observed a large sample of stars, galaxies, clusters of galaxies, binaries and AGN. A highlight in the field of AGN was the detection of X-ray spectral variations in the quasar MR 2251-178 which provided the first evidence for ionized circumnuclear gas reprocessing the X-ray continuum in AGN (Halpern, 1984). *The Einstein Observatory* moved X-ray astronomy forward by providing images of diffuse emission and extended objects. Moreover, it was the first mission to facilitate a guest observer program. The lifetime of *The Einstein Observatory* was from November 1978 to April 1981.

In the 1980s, while X-ray astronomy was in a quiescent state in the USA, the European Space Agency (ESA) contributed *EXOSAT* while the Japanese Scientific Space Agency (JAXA) contributed the *Hakucho*, *Tenma* and *Ginga* satellites. Equipped with large-area proportional counters and channel multiplier array (CMA), *EXOSAT* observed rapid flux variability; for example rapid variability was observed in $\sim 40\%$ of AGN studied by Green et al. (1993). Utilizing its broad bandpass, *EXOSAT* also allowed for advances in spectroscopy, e.g. the detection of an excess of the soft-band X-ray flux ('soft excess') relative to the 2-10 keV continuum level in $\sim 50\%$ of AGN (Turner & Pounds, 1989).

The *ROSAT* (the ROentgen SATellite) was a German-US-UK collaboration, manufactured by Germany and launched by the United States in 1990. *ROSAT* was under operation until 1999. ROSAT (0.1–2.5 keV) performed a full-sky survey, generating a catalog of more than 100,000 X-ray sources which included almost all astronomical objects e.g. comets, stars, X-ray binary stars, neutron stars, supernovae, black holes, etc. A surprising discovery was the detection of X-rays from comets. *ROSAT* detected many distinct absorption features in AGN spectra e.g. an oxygen K edge at 0.8 keV was detected in Seyfert 1 galaxy MCG-6-30-15, which indicated the presence of 'warm' (highly ionized) absorbing material (Nandra & Pounds, 1992). Furthermore, this absorption feature was found to be variable on timescales of a day to weeks which indicated the changes in the absorbing gas opacity (Fabian et al., 1994; Otani et al., 1996). Many other individual strong features were found in Seyfert galaxies which indicated the presence of multiple zones of ionized gas (e.g. Mihara et al. 1994; Nandra et al. 1993; Pounds et al. 1994; Ptak et al. 1994; Turner et al. 1993; Yaqoob et al. 1994).

A new era of advanced technology emerged with the invention of X-ray sensitive charge-coupled devices (CCDs). The first satellite to carry these devices into space was Japan's Advanced Satellite for Cosmology and Astrophysics (*ASCA*), launched in 1993 in collaboration with NASA. The Solid-State Imaging Spectrometers (SIS, Burke et al. 1993) provided a larger effective area than *ROSAT* for energies > 2 keV, and a broad bandpass from 0.1 to 10 keV with an improved spectroscopic resolution of 320-450 eV (FWHM) between 0.6 - 1.2 keV. *ASCA* allowed a study of strong emission line features e.g. Fe Kα, which had been unresolved in previous observations with proportional counters. One of the key observations was the strong spectral curvature around 6 keV in many Seyferts which was interpreted by some to be an Fe K emission line, broadened and redshifted by relativistic effects in the vicinity of the event horizon (Fabian et al., 2000). However, other interpretations were made by using models of complex absorption (e.g. Gondoin et al. 2001; Reeves et al. 2004; Turner et al. 2005). In the spectral and temporal analysis of a sample of 24 Seyfert galaxies, Turner et al. (1997) discussed various important X-ray parameters e.g. the flux variability, the absorbing columns and Fe Kα emission. It was found that a few Seyfert 2s had similar flux variability characteristics to those of Seyfert 1s. Reynolds (1997) and George et al. (1998) studied the absorption properties of AGN and showed that 60% of Seyfert 1 galaxies exhibited the soft X-ray spectral features of an ionized gas having column $N_H \sim 10^{21}$ - 10^{23} cm^{-2} and ionization parameter $\xi \sim 10$ - 50 erg cm s^{-1}. After operating successfully for over 7 years, the end of the *ASCA* mission came in 2000 due to terminal damage from a geomagnetic storm.

From 1995 to 2012, NASA's Rossi X-ray Timing Explorer (*RXTE* was operational, utilizing large proportional counters (2–60 keV) that gave the satellite a high sensitivity. It was designed to study the time variability of X-ray sources, and achieved unprecedented time resolution down to microseconds. *RXTE* allowed construction of power density spectra (PDS) over a broader range of temporal frequencies than had been previously possible. For example, Edelson & Nandra (1999) observed the highly variable Seyfert 1 galaxy NGC 3516 and constructed an X-ray fluctuation PDS which showed the flattening of the power-law slope from -1.74 at short timescales to -0.73 at longer timescales.

The Italian-Dutch satellite *BeppoSAX* was launched in 1996, covering an energy range of more than three decades 0.1 - 300 keV. Orr et al. (1997) studied the spectral variation in the energy range 0.1 - 4 keV of MCG-6-30-15 and observed rapid changes in the absorption near O VIII K-edge, which further confirmed the presence of a complex absorber in MCG-6-30-15. *BeppoSAX* also observed gamma-ray bursts, which are considered to be the most powerful explosions in the Universe since The Big Bang.

2.2.2 Missions launched since 1999

Moving on to the great X-ray observatories of this age, NASA's *Chandra* observatory (launched in July 1999) and ESA's *XMM-Newton* observatory (December 1999) are both operational at the time of writing. The *Suzaku* observatory (July 2005 - Sept. 2015) from JAXA completed its last year of operation while this thesis was being written. Recently launched in June 2012, the Nuclear Spectroscopic Telescope Array (*NuSTAR*), provides the first focusing optics in the high energy X-ray band (3 - 79 keV). *NuSTAR* observes the hard X-ray sky with more sensitivity and a lower background level than that of the collimated or coded mask instruments (that have operated in this energy band). Thus, *NuSTAR* provides new constraints on X-ray reprocessing in AGN. The technical details of these observatories are discussed in the following sections.

Launched on Feb. 17, 2016, *Hitomi*, from a collaboration between JAXA and

NASA, will provide the highest energy resolution ever achieved at E $>$ 3 keV. It has four focusing telescopes: two Soft X-ray Telescopes (SXTs) cover medium energy X-rays from 0.3 to 12 keV, and two Hard X-ray Imaging detectors (HXTs) extend the energy range from 5 to 80 keV with energy resolution 2 keV (FWHM) at 60 keV (Takahashi et al., 2014). Using the Soft Gamma-ray detector (SGD), the energy coverage further extends to 600 keV, with energy resolution 4 keV (FWHM) at 40 keV. A key instrument aboard *Astro-H* is the Soft X-ray Spectrometer (SXS) which provides unprecedented high-resolution spectroscopy (ΔE $<$ 7eV, FWHM at 6 keV) with its state-of-the-art X-ray calorimeter spectrometer, and is highly sensitive over 0.3 - 12 keV.

2.3 X-ray satellites used in this thesis

For my analysis of the Seyfert 2 galaxy NGC 1068, I have utilized data obtained by: *XMM-Newton*, *Chandra*, *Suzaku* and *NuSTAR*. In the following sections, I detail the science instruments aboard these satellites along with the corresponding data extraction tasks.

2.3.1 *XMM-Newton*

XMM, the largest (10-meter long) science spacecraft ever launched by ESA, was placed into orbit December 10, 1999. In its highly elliptical 48-hour orbit, *XMM* has an apogee 114,000 km and a perigee 7000 km. Due to its highly eccentric orbit, the instruments onboard allow a long continuous observation before the spacecraft enters into the radiation belt at perigee. *XMM* has a very high pointing accuracy of 0.25″ over a 10-sec interval (at 95% confidence level). *XMM* has an effective area 4650 cm^2 at 1 keV (see Figure 2.1).

XMM carries three X-ray telescopes consisting of 58 Wolter I grazing incidence mirrors with an angular resolution of FWHM $\sim$ 6 arcseconds. These are arranged on the Mirror Support Platform (MSP) along with an Optical Monitor (Figure 2.2) and therefore, the desired field of view can be observed simultaneously at X-ray and optical/UV wavelengths. Located at the other end of a 7 meter long X-ray telescope tube, is the Focal Plane Assembly (FPA) occupied by two Reflection Grating Spectrometer (RGS) focal plane cameras and three European Photon Imaging Camera (EPIC) imaging detectors. The focal plane instruments are further described below.

2.3.1.1 EPIC MOS and pn

EPIC facilitates sensitive imaging observations of the X-ray sky using two types of X-ray CCD camera: Metal Oxide Semi-conductor (MOS) and pn semi-condcutor (named according to its topology, using n-type and p-type materials) CCDs. The RGS instruments on board also disperse their spectra onto two additional MOS CCDs. Half of the incident light is diverted towards the RGS detectors such that about 44% of the photon flux is gathered at MOS cameras. The pn camera, at the focus of the third X-ray telescope receives an unobstructed beam of incoming flux. With different CCDs configurations, readout times and modes of operation, the two types of EPIC cameras provide a field of view of $\sim$ 30 arcmin with a spectral resolution $\frac{E}{\Delta E} \sim$ 20-50 and cover an energy range from 0.15 to 15 keV.

2.3.1.2 OM

Mounted on the MSP next to the three X-ray telescopes, the Optical Monitor is a 30 cm Ritchey-Chretien telescope with a focal length of 3.8 m. The optical/UV telescope has an unprecedented capability to observe the sky in optical/UV waveband simultaneously. It operates within wavelengths of 170 nm to 650 nm, and covers 17 arcmin^2 of the X-ray field of view. The telescope provides a resolving power of $\sim$ 180 and is highly sensitive. It can operate in two modes: the imaging mode provides 2-D images with long exposure times ($>$ 800s), and the fast mode produces high time resolution images over small areas. The OM also contains a set of broadband filters used for color discrimination e.g. the filters in U, V and B bands operate in the wavelength range 300-390 nm, 510-580 nm and 390-490 nm, respectively.

2.3.1.3 RGS

Each of the two Reflection Grating Spectrometers, located at the exit point of the two X-ray telescopes, comprises a stack of 182 gratings (Figure 2.3). The array of gratings deflect half of the light to the CCD detectors situated off-axis on the focal plane, as illustrated in Figure 2.3. The undeflected light is intercepted by EPIC in the telescope focal plane. The gratings are rotated in a Rowland circle to form a toroidal shaped surface. The dispersed spectra are detected by the nine back-illuminated CCDs located on the Rowland circle, as RGS focal camera (RFC) in Figure 2.3. Unfortunately, due to the failure of CCD7 and CCD4, the wavelength ranges of 11 - 14 Å and 20 - 24 Å are bereft of data in RGS 1 and 2, respectively.

The wavelength of an X-ray photon on the detector is given by the following dispersion equation:

$m\lambda = d(\cos\beta - \cos\alpha)$,

where m is the spectral order, d is the groove spacing, α and β are the angles of the incoming and outgoing rays, respectively (Figure 2.4). The wavelengths are measured with an accuracy of 7 mÅ. The instrument covers soft X-ray range of 6 - 38 Å (2.1 - 0.3 keV) with a maximum area of 140 cm^2 at 15 Å. Its configuration and features aim to provide the detection of the K-shell transitions of carbon, nitrogen, oxygen, neon, magnesium, silicon and L-shell transitions of Fe.

2.3.1.4 Data Analysis

XMM data are provided in two main directories: (1) The Observation Data Files (ODF) directory contains the basic files (2) The Pipeline Processing System (PPS) directory provides processed 'data products'. The basic files are the instrument science files and housekeeping files, provided "FITS" format (Flexible Image Transport System). Extracted from the telemetry packets, ODF science files are uncalibrated (cannot be directly used for the data analysis) and are stored in their raw form.

In the process of transforming the ODF into the required PPS scientific products for each instrument, a number of tasks are performed. The first step involves the selection of correct source coordinates of the target source, and computation of an extraction region centered on the source. Typically for AGN, circular extraction regions are used for the source and background spectra, with radii $40''$ and $1'$, respectively. To compute the background, the extraction cell is placed away from the source (usually on the same detector chip) to exclude the source photons and any other targets in the field of view. Subsequent tasks to generate the spectrum and their corresponding files differ for each instrument. Most commonly, after obtaining a calibrated, cleaned and filtered event file with good time events, the source and background spectra are extracted with their corresponding RMFs and ARFs (for their definitions see section 2.1). Many other important processed data products e.g. the positions and brightnesses of detected sources, images, light curves, etc., are provided in the PPS. The processed, calibrated events files can be analyzed using the various software tools (e.g. FTOOLS[1]) for imaging and spectral analysis.

2.3.2 *Chandra*

Chandra, formerly known as the Advanced X-ray Astrophysics Facility (AXAF), has been orbiting Earth since its launch in July 23, 1999 by NASA. *Chandra* has a spatial resolution of 0.5 arcsec (FWHM), the highest spatial resolution achieved by an X-ray observatory to date. Its high resolving power is equivalent to clearly reading a stop sign from a distance of 12 miles. The science instruments utilize an

[1]https://heasarc.gsfc.nasa.gov/ftools/ftools_menu.html

energy range from 0.1 to 10 keV with an effective area of 200 cm^2 (ACIS-S) at 1.5 keV (see Figure 2.5). The telescope covers a field of view of 30 arcmin. In a 64-hours highly-eccentric orbit, *Chandra* travels more than one third of the way to the moon and flies 200 times higher (relative apogee) than Hubble. During its passage near the radiation belts (altitude $\sim$ 60,000 km), *Chandra* ceases to accumulate data for 20% of its orbital period, and the observing efficiency is maintained at $\sim$ 75% of total orbit time, as limited by other orbital constraints. The *Chandra* telescope uses 8 Wolter type-I mirrors nested on High Resolution Mirror Assembly (HRMA). The incoming flux of X-ray photons, reflected by these mirrors, is focused on a detector placed $\sim$ 30 feet away (Figure 2.6). A layout of the spacecraft's major components is illustrated in Figure 2.7.

2.3.2.1 HRC and ACIS

The two focal plane instruments, the High Resolution Camera (HRC) and the Advanced CCD Imaging Spectrometer (ACIS) detect the reflected X-rays from the mirrors. These are situated at the end of the optical bench (Figure 2.7). HRC makes use of Micro-Channel Plates and consists of two detectors devoted to imaging analysis (HRC-I), and spectral analysis (HRC-S) only when used with low energy gratings to detect the dispersed photons. HRC has the largest field-of-view ($\sim 30'$x$30'$) of any detector onboard and an unparalleled capability to make images with high spatial resolution ($< 0.5''$). ACIS contains sophisticated CCDs to simultaneously produce the high-resolution images and moderate-resolution spectra. The ten ACIS CCDs can be configured in a number of ways, most commonly a 2x2 array for imaging and 1x6 for spectroscopy (Figure 2.8).

2.3.2.2 The High Resolution Spectrometers

There are two high resolution spectrometers: the High Energy Transmission Grating Spectrometer (HETG) and the Low Energy Transmission Grating Spectrometer (LETG). The gratings (made of gold) used in HETG and LETG are moved back and forth behind the mirrors to focus the deflected X-rays onto a detector. The regular spacing of the grating bars is finer in HETG (0.2 μm) than in LETG (1 μm). LETG can be used in conjunction with ACIS-S with much lower quantum efficiency of $< 60\%$ and a smaller usable energy range of 0.08 - 0.2 keV. LETG provides the best resolution spectroscopy at low energies between 0.07 - 0.15 keV.

HETG (Canizares et al., 2005) spans a range of 0.4 - 10 keV (31 - 1.2 Å) with a resolving power of $\frac{E}{\Delta E} \sim 1000$. It itself includes two distinct sets of gratings: the High Energy Grating (HEG) and the Medium Energy Grating (MEG). To distinguish them from each other, these gratings are mounted on the same structure but at different angles such that X-rays are dispersed in a form of shallow X with its center at the zeroth order (undispersed light). Two arms of the X are HEG and MEG (see Figure 2.9). A few properties of HEG and MEG are compared in the following table:

	HEG	MEG
Energy Range	0.8 - 10.0 keV	0.4 - 5.0 keV
Wavelength Range	15 - 1.2 Å	31 - 2.5 Å
Resolution	0.012 Å FWHM	0.023 Å FWHM
Wavelength Accuracy	±0.001 Å	±0.002 Å

2.3.2.3 Data Analysis

The *Chandra* archived data for an HETG/ACIS grating observation are downloaded in two directories: primary and secondary. The most important data products for this analysis are event files, having different levels e.g. 0, 1, 1.5 and 2. Level 0 event files are very raw, carrying telemetry information. Level 1 files contain the basic information, e.g. physical coordinates, detector PHA, energies, etc., of X-ray events. In the level 1.5 files, the zeroth-order centroids, grating spectral orders and the diffracted coordinates are determined. Finally, the level 2 event files are created by assigning the grades to each event, and then good time intervals (GTIs) are applied at the end. The primary directory contains all the files that can be directly used for the data analysis, e.g., level 2 event files but with default parameters, whereas the secondary directory carries the level 1 event files which were a starting point of reprocessing in this analysis.

The final data products, level 2 spectral files (PHA2), were created using the data analysis tools from CIAO 4.6 (*Chandra* Interactive Analysis of Observations). Beginning with the level 1 event file, the first two steps involved locating the zeroth-order position and the grating arms (HEG, MEG) using "TGDETECT2" and "TG_CREATE_MASK", respectively. In "TG_CREATE_MASK", the spatial regions of each grating arm were defined by assigning new zeroth_order positions (physical X and Y coordinates) and widths. The wavelengths and grating orders of the dispersed photons were computed using "TG_RESOLVE_EVENTS". After applying good grades (equal to 0, 2, 3, 4 and 6) and GTIs filters on the diffracted events, the level 2 event file ("evt2") was created. Ultimately, the grating spectral file (PHA2) was binned and extracted from "evt2" file using "TGEXTRACT". The corresponding RMFs and ARFs for each grating and order were produced by "MKGRMF" and "FULLGARF", respectively.

2.3.3 *Suzaku*

The Japanese spacecraft *Suzaku*, launched on July 10, 2005 through an international collaboration between Japan and the United States, flew at a low altitude of 568 km (apogee) at an inclination of 31.9 degrees. Its orbit was nearly circular with an orbital period of $\sim$ 96 minutes. The spacecraft had an observational constraint of pointing in a single direction for 1/4 of the day. Thus, a large number of sources were occulted by Earth in 1/3 of its orbit resulting in an observing efficiency $\sim$ 45%. The instruments in operation onboard *Suzaku* (Figure 2.10) were: four X-ray Imaging Spectrometers (XISs) with imaging CCDs and one non-imaging Hard X-ray Detector (HXD), and all of them were able to work simultaneously. XISs covered an energy range of 0.4 - 12 keV with an energy resolution of $\sim$ 130 eV (FWHM) at 6 keV. HXD extended the energy range from 10 - 600 keV using two types of sensors: the PIN diodes (10 -70 keV) and the GSO crystal scintillators (40 - 600 keV). The energy resolution of both hard band instruments was very low (e.g. 4.5 keV FWHM for the PIN diodes, and $7.6/\sqrt{\mathrm{E}}\%$ FWHM for the GSO) compared to that of XISs. *Suzaku* offered moderate resolution constraints on the important Fe K-shell features (6-7 keV) along with the most sensitive measurement of the spectral curvature above 10 keV.

2.3.3.1 Data Analysis

The XIS calibrated event files were obtained by running the standard pipeline processing. The cleaned event files were screened to exclude the data obtained during certain time intervals of passage through the South Atlantic Anomaly (SAA, a region of high particle flux). Good events with grades 0, 2, 3, 4, and 6 were used, while hot and flickering pixels were removed using the SISCLEAN script. [A grade is defined by certain pattern of pixels, having charge accumulated above a threshold value.] Data with Earth Elevation Angle (ELV) less than 5^o and magnetic cut-off rigidity (COR) less than 6 GeV were also rejected. The XIS source spectra were extracted from circular extraction region of $170''$ radius centered on the source, using XSELECT. The background spectrum was extracted from a source-free region on the same chip, avoiding the calibration sources. The RMFs and ARFs were extracted for the HXD nominal pointing. Similarly, PIN and GSO spectral, background and response files were generated following the standard data reduction techniques[2].

[2]http://heasarc.gsfc.nasa.gov/docs/suzaku/analysis/abc/

2.3.4 *NuSTAR*

Launched by NASA on June 13, 2012, *NuSTAR* is the first space-based hard X-ray imaging observatory that operates in the energy band from 4 to 79 keV. The *NuSTAR* instruments utilize a Wolter I design comprised of 133 concentric mirror shells. The two co-aligned hard X-ray telescopes focus the X-rays onto the solid-state detectors separated by a 10 meter mast (see Figure 2.11) that was extended from the spacecraft after launch. The solid-state detectors of each focal plane module (FPMA & FPMB) are surrounded by an anti-coincidence shield which reduces the background above 10 keV. Thus, they provide more than two orders of magnitude improvement in sensitivity in contrast to previous high-energy missions e.g. *XMM* and *Chandra*. The X-ray optics of the instruments provides an angular resolution of $18''$ FWHM. The focal plane instruments are designed to achieve a good energy resolution of 400 eV at 10 keV and 0.9 keV at 60 keV. It has the largest effective area in the high energy range, as compared to other X-ray satellites in Figure 2.1.

2.3.4.1 Data Analysis

The *NuSTAR* data analysis tasks, within the NuSTARDAS software (v1.4.1) package, are performed in three levels. In the first two stages, the calibrated, cleaned and screened event files were produced by running the task NuPIPELINE. The source and background spectra for both FPMA and FPMB were extracted using circular regions of radii $80''$, along with their corresponding RMFs and ARFs, using the task NuPRODUCTS. The background spectra were obtained from a region far away from the source but on the same detector. In this analysis, I used spectra between 3 and 55 keV. The upper limit for useful data was set by systematic uncertainties found during on-orbit calibration.

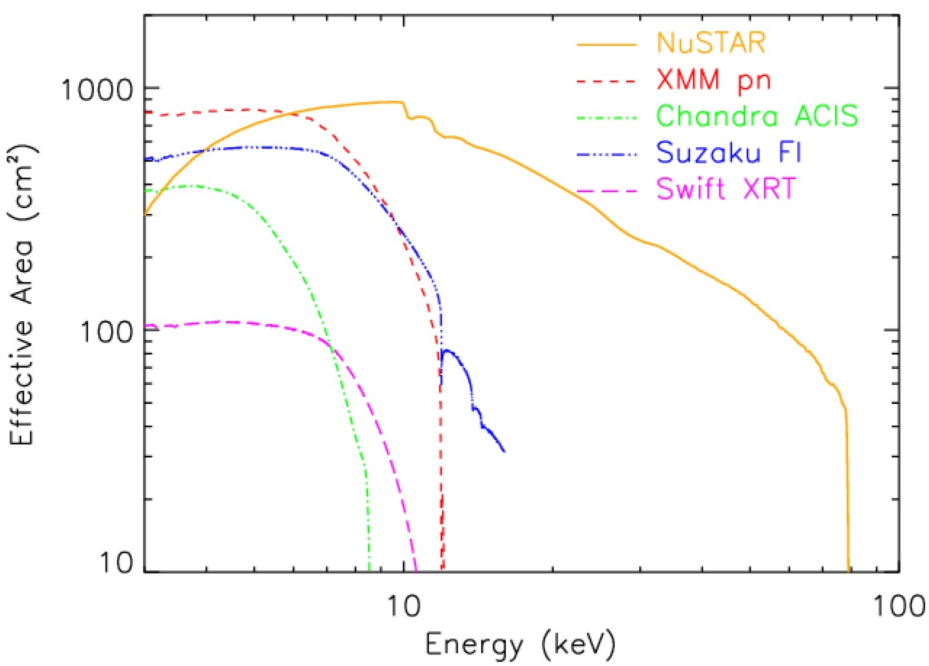

Figure 2.1: A comparison of effective areas of different instruments, Harrison et al. (2013)

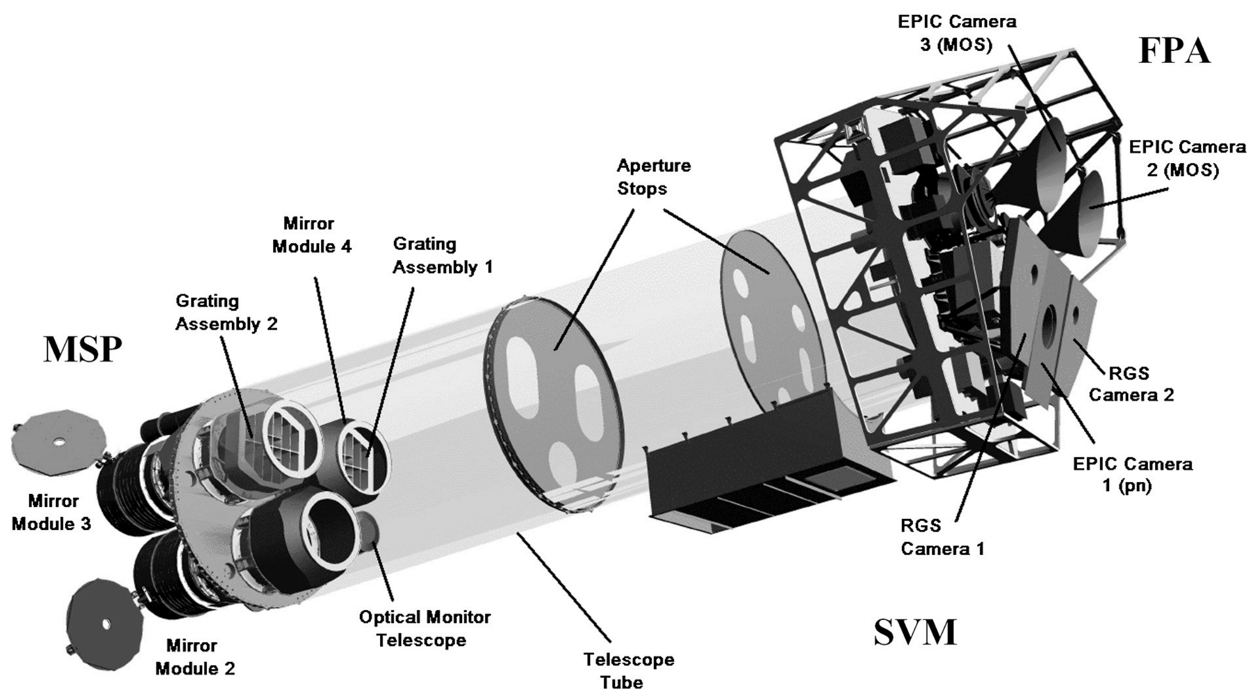

Figure 2.2: The *XMM-Newton* observatory. Image courtesy: ESA

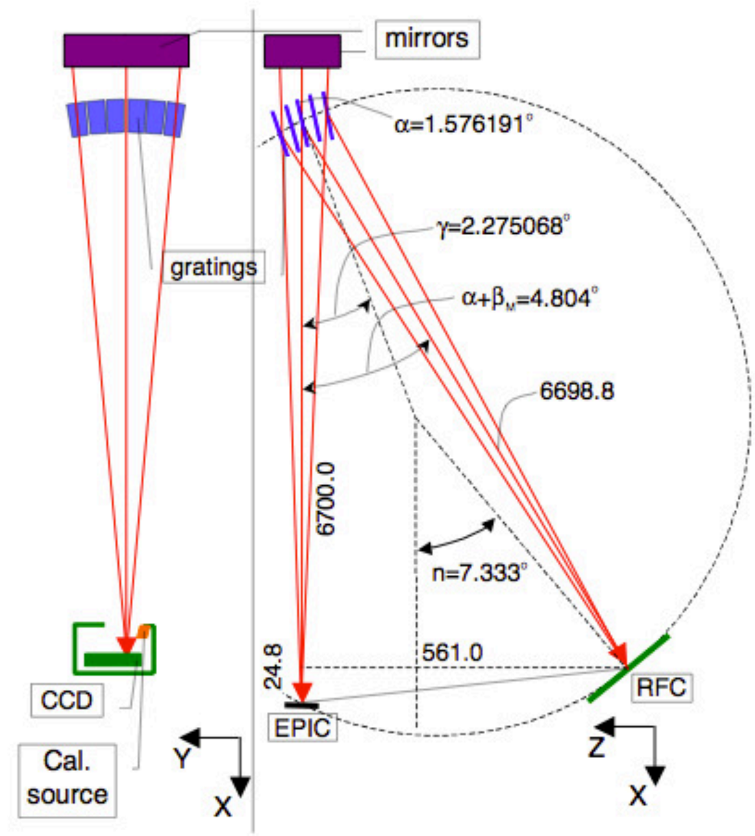

Figure 2.3: RGS layout. Image courtesy: ESA

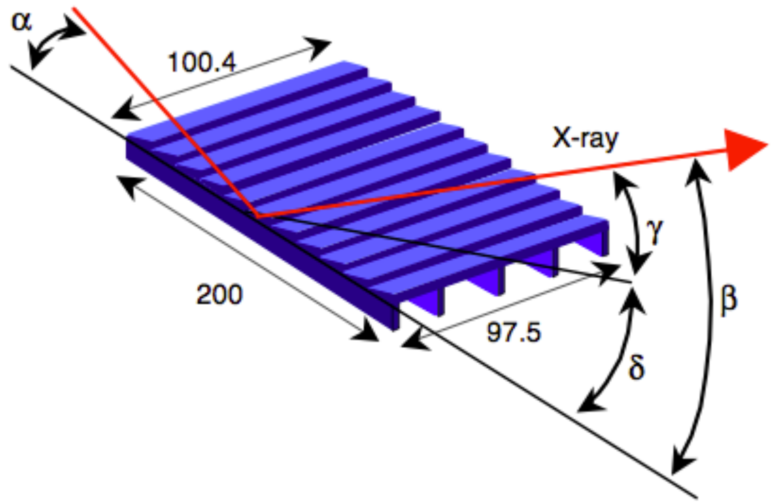

Figure 2.4: Gratings used by RGS. Image courtesy: ESA

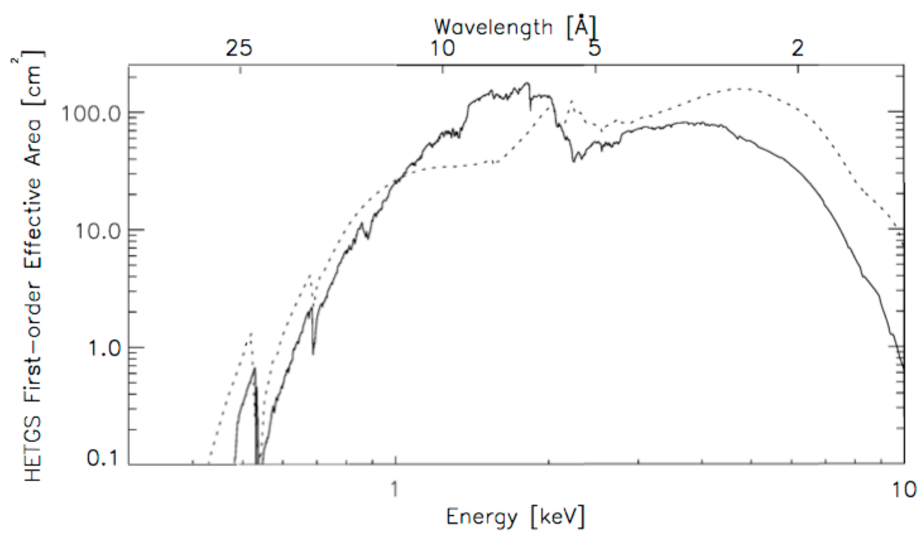

Figure 2.5: The HETG first-order (solid curve) and zeroth-order (dotted curve) effective area. Image courtesy: NASA/GSFC

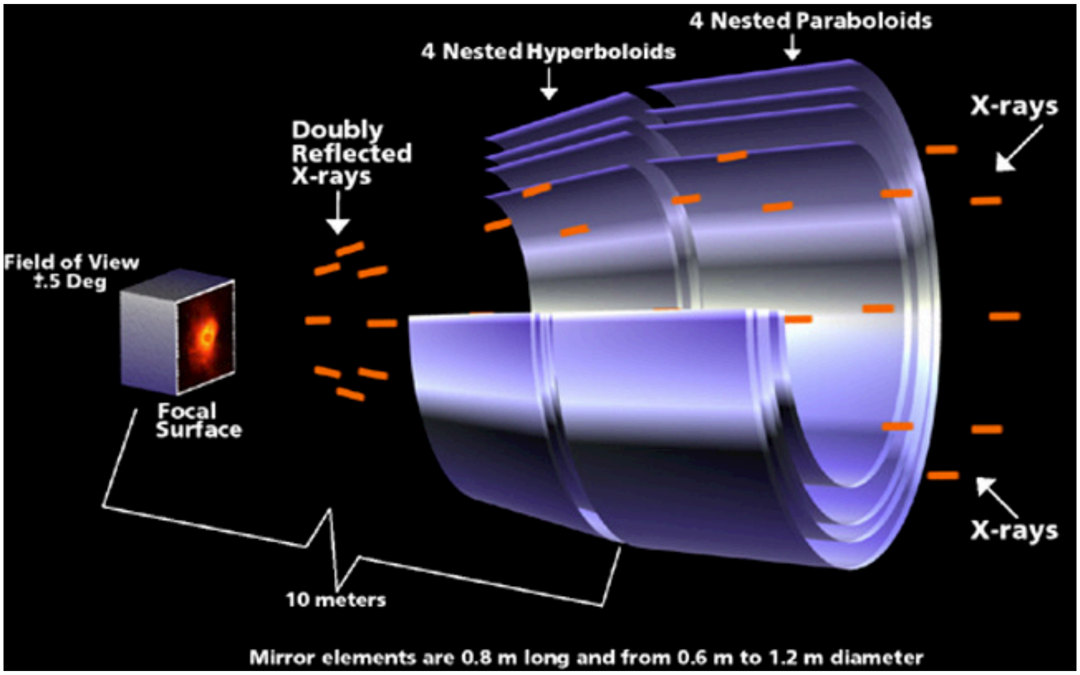

Figure 2.6: The geometry of the mirrors onboard *Chandra*. Image courtesy: NASA

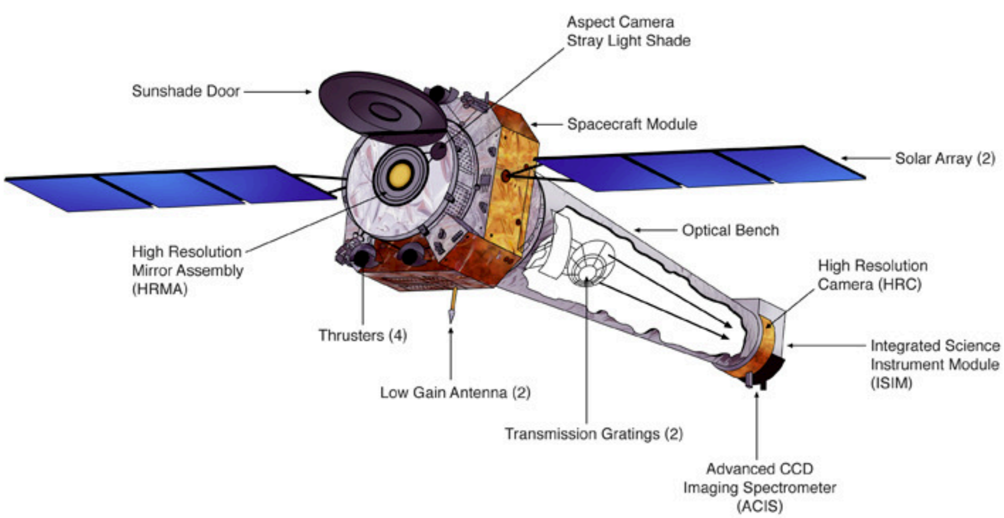

Figure 2.7: *Chandra*. Image courtesy: NASA

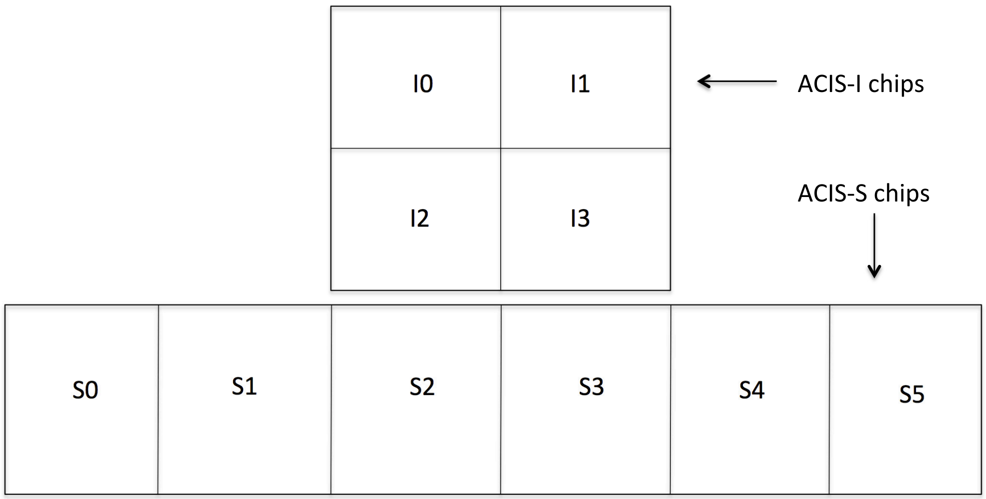

Figure 2.8: The configurations of the chips used in ACIS-I and ACIS-S.

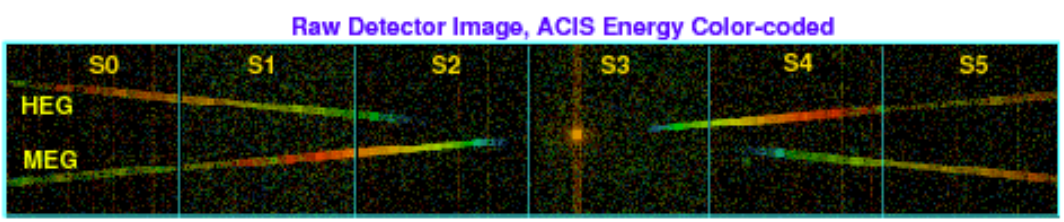

Figure 2.9

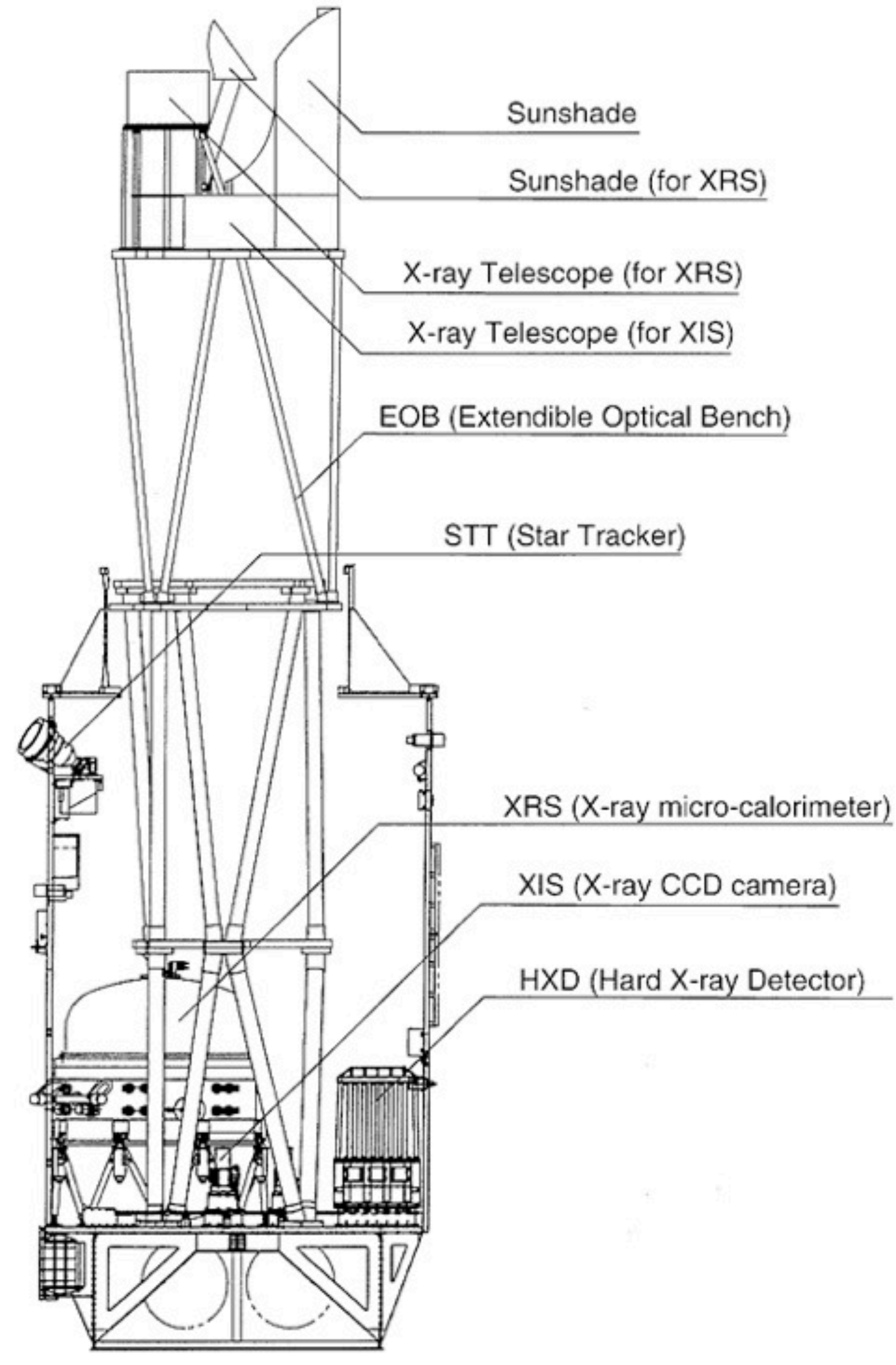

Figure 2.10: A schematic layout of *Suzaku*. Image courtesy: JAXA

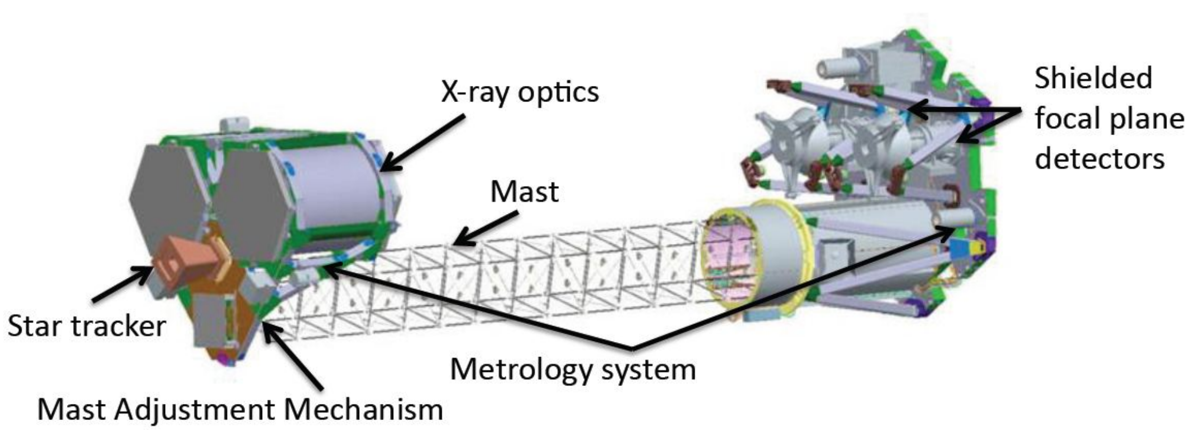

Figure 2.11: The *NuSTAR* observatory. Image courtesy: NASA/GSFC

Chapter 3: Photoionization Models for Astronomical Data

3.1 Photoionized gas in the X-ray regime

3.1.1 Physics of the photoionized gas

In the circumnuclear regions of AGN, gas is heated and ionized by the central continuum. A large number of diverse spectral features are produced by this reprocessing, which offer great insight into the physics of the active nucleus and the material lying in its vicinity. Depending upon the different physical conditions (density, temperature, ionization parameter, etc.) in the circumnuclear gas, a variety of physical processes take place. Those most relevant to this work are discussed in this chapter, using standard notation (from Dopita & Sutherland 2003), e.g. "A" represents an atomic specie, "$*$" denotes the excited state of an atom, "i" stands for the ionization state, and E is the energy released or absorbed in the process.

Photoionization: This results from the ejection of an electron from an atom after the absorption of a photon, which can be described as follows:

$$\mathrm{A}^{i} + h\nu \longrightarrow \mathrm{A}^{(\mathrm{i+1})+} + \mathrm{e}^{-} + \Delta\mathrm{E} \qquad (1)$$

Since some amount of energy, E, is being added to the system, photoionization contributes to gas heating. By further increasing the energy of the incoming photon, the electrons from the inner shell of an atom can be removed, and these L- and K-shell transitions are sometimes referred to as inner shell photoionization, which may be followed by another mode of ionization, Augur ionization as described below (3) and (4). Auger ionization can affect the intensities of some weak emission lines.

$$\mathrm{A}^{i} + h\nu \longrightarrow \mathrm{A}_{**}^{(\mathrm{i+1})+} + \mathrm{e}^{-} + \Delta\mathrm{E}_1 \qquad (2)$$

$$\mathrm{A}_{**}^{(i+1)} \longrightarrow \mathrm{A}_{*}^{(\mathrm{i+m+1})} + \mathrm{e}^{-} + \Delta\mathrm{E}_2 \qquad (3)$$

$$\mathrm{A}_{*}^{i+m+1} \longrightarrow \mathrm{A}^{\mathrm{i+m+1}} + \mathrm{h}\nu_1 + \mathrm{h}\nu_2 .... \qquad (4)$$

where m is the principal quantum number. "$**$" represents the highly excited atom.

Observationally, the presence of strong forbidden lines (relative to the resonance and inter-combination lines) in He-like triplets indicates the dominance of photoionization in the gas. Forbidden lines are produced in low density regions ($< 10^7$ cm^{-3}) where electrons can stay in their excited states for relatively long periods of time (several minutes or more). However, in high density regions, collisions occur on much shorter time scale (10^{-8} s), e.g. in collisionally excited gas, ions and electrons frequently collide to deexcite the atom back to the ground state without radiating away a photon.

Resonance lines are emitted due to the normal electric dipole transitions having very high transition probability of 10^8-10^9 s^{-1}. At low enough densities the inter-combination and forbidden lines are produced by electric quadrupole and magnetic dipole transitions with probabilities of the order of 10^2 and 10^{-3} s^{-1} or less, respectively.

Quantum mechanically, the resonance lines are produced by permitted transitions whilst, as the name suggests, the forbidden lines are produced by forbidden transitions. According to the standard selection rules of Quantum Mechanics, the change in the angular quantum number "l" is 1 for the resonance line, 0, 1 for the inter-combination lines, and 0, 2 for the forbidden lines (see Figure 3.1).

Under certain physical conditions, He-like triplets, composed of resonance (r), inter-combination (i) and forbidden line (f) components, are produced in the photoionized gas. The line ratios of $\frac{f}{i}$ and $\frac{f+i}{r}$ can be used to determine the electron density and temperature, respectively, as shown by Gabriel & Jordan (1969) and Porquet & Dubau (2002).

Radiative Recombination : This is the inverse process of photoionization. An electron is captured by an ion to one of its bound energy levels and the excess energy is released in the form of an energetic photon. In some cases, the atom rests in its excited state by capturing an electron and then radiated back to its ground state as shown below:

$$\mathrm{A}^{i} + \mathrm{e}^{-} \longrightarrow \mathrm{A}_{*}^{(\mathrm{i}-1)+} + \mathrm{h}\nu \qquad (5)$$

$$\mathrm{A}_{*}^{(i-1)+} \longrightarrow \mathrm{A}^{(\mathrm{i}-1)+} + \mathrm{h}\nu_1 + \mathrm{h}\nu_2 + \mathrm{h}\nu_3 \ldots\ldots\ldots\ldots\ldots\ldots \qquad (6)$$

(5) represents the radiative recombination continuum where the energy of the radiated photon equals the kinetic energy of the incoming electron which is not quantized and thus a continuous spectrum is formed. Photons in (6) illustrate the discrete quantum transitions giving rise to the recombination lines.

Dielectronic Recombination : This is the process of interaction of an ion with a free electron. In many situations, dielectronic recombination becomes more important than radiative recombination. If the energy of the incoming free electron is above the ionization limit, then it can excite a core electron of the ion. To make it easy to understand, the ionization state of a specie can be represented by the principal quantum number, n and the angular quantum number, l.

$$\mathrm{A}^{i+}(1\mathrm{s},....) + \mathrm{e}^- \longrightarrow \mathrm{A}_*^{(\mathrm{i}-1)+}(\mathrm{n}_1\mathrm{l}_1;\mathrm{n}_2\mathrm{l}_2) \qquad (7)$$

$$\mathrm{A}_*^{(i-1)+}(\mathrm{n}_1\mathrm{l}_1;\mathrm{n}_2\mathrm{l}_2) \longrightarrow \mathrm{A}_*^{(\mathrm{i}-1)+}(\mathrm{n}_3\mathrm{l}_3;\mathrm{n}_2\mathrm{l}_2) \qquad (8)$$

$$\mathrm{A}_*^{(i-1)+}(\mathrm{n}_3\mathrm{l}_3;\mathrm{n}_2\mathrm{l}_2) \longrightarrow \mathrm{A}^{(\mathrm{i}-1)+}(\mathrm{n}_3\mathrm{l}_3;\mathrm{n}_4\mathrm{l}_4) + \mathrm{h}\nu_1 + \mathrm{h}\nu_2........ \qquad (9)$$

(7) shows the recombination of an electron, where the recombined ion is left in its excited state. Now the recombined ion has one electron in the autoionizing state $\mathrm{n}_1\mathrm{l}_1$ and the other in the excited state $\mathrm{n}_2\mathrm{l}_2$. In the next step (8), the ion first stabilizes itself by radiating the excited electron back to its ground state $\mathrm{n}_3\mathrm{l}_3$. Finally, the recombined but still excited ion cascades down to its ground state through discrete quantum transitions, as shown in (9).

Collisional Ionization: This process represents the collision of an electron and ion with sufficient energy that a bound electron is ejected. Since energy is removed from the incoming electron, therefore this process acts as a gas coolant.

$$\mathrm{A}^{i+} + \mathrm{e}^- \longrightarrow \mathrm{A}^{(\mathrm{i}+1)+} + 2\mathrm{e}^- - \Delta\mathrm{E} \qquad (10)$$

This occurs in high-density regions, in contrast to photoionization. In collisional ionization, electrons are mainly responsible for any change in the physical conditions, whereas in photoionized gas most of the work is done by photons. Due to the large atomic densities and thus highly probable transitions, there exists a dynamic balance between collisional ionization and the recombination of the ions to their ground state by radiative decays. In a gaseous region dominated by collisional ionization, strong resonance and weak forbidden lines are seen.

Charge Exchange: This process involves the collision between two ions where an electron is exchanged between them. The charge exchange process can be illustrated by the following reactions:

$$A^{(i+1)+} + H^0 \rightleftharpoons A^{i+} + H^+ + \Delta E \qquad (11)$$

$$A^{(i+1)+} + He^0 \rightleftharpoons A^{i+} + He^+ + \Delta E \qquad (12)$$

In the reverse reaction, E is the energy required to push the two charged species within a certain distance such that the charge-exchange can take place between them.

3.2 The Photoionization code CLOUDY

To constrain and simulate the physical conditions of the X-ray narrow line region (XNLR) gas, I used a sophisticated photoionization code CLOUDY (version C10.00, Ferland et al. 2013). In this code, the emission line intensities are calculated by solving the equations of thermal and statistical equilibrium, the equations to balance the heating and cooling processes, and the radiative transfer equations. The process of heating includes photoionization heating and Compton heating, whereas its inverse i.e. cooling process (removal of energy), includes radiative recombination, bremsstrahlung, and radiative deexcitation of bound levels. The emission line intensities, calculated from the radiative transfer solution, depend on a number of parameters that can be varied within a certain range. The most important parameters that influence the line intensities are: abundances, incident continuum, geometry, ionization parameter, column density and hydrogen density. Some additional parameters can be considered depending on the desired output.

3.2.1 Abundances

CLOUDY assumes, as a default, solar abundances (Asplund et al., 2005) of the first 30 elements (from the periodic table). Abundances used here are determined from the solar photosphere and meteorites, and can be changed by the user. These abundances are calculated relative to that of the sum of hydrogen in atomic, ionic and molecular form.

3.2.2 Geometry

The geometrical shape of the clouds and the surrounding gas in AGN is another important aspect that influences the results significantly. CLOUDY considers two types of geometry: open and closed. The open geometry assumes a plane parallel slab of gas. The closed geometry considers a sphere of gas, as in the case of planetary nebula or H II regions, where the central object is very small in comparison to the surrounding nebulae. In the model for this study, we assumed an open geometry. CLOUDY divides a cloud into thin concentric shells, called zones. The radius of a zone is the distance from the central engine to the center of that zone. In the plane parallel geometry, the radial location of the cloud is far larger than the thickness of the cloud (Figure 3.2). The thickness or depth (R) of a cloud is the distance between the illuminated and shielded face of the cloud.

3.2.3 Continuum

The only source that heats and ionizes the surrounding gas in AGN is considered to be the continuum from the central engine of AGN. The shape of the spectral energy distribution (SED) must be specified from 10^{-8} Ryd to 7.354x10^6 Ryd, as required by CLOUDY.

After striking the illuminated face of the cloud, the incident continuum gets absorbed, scattered or transmitted through the assumed thickness of the gas cloud. The side of the cloud facing the central source of continuum photons is the illuminated face of the cloud, whereas the opposite side of the cloud is the shielded face. As the names suggest, the illuminated face is always more ionized and much hotter than the shielded face. As shown in Figure 3.2, the following kinds of continua are considered in CLOUDY:

(1) Reflected Continuum: This is sometimes also called the reflected spectrum. This is the continuum that is being reflected back from the illuminated face of the cloud towards the central source itself. The reflected continuum is calculated for the open geometry only. This continuum also includes the diffuse continuum directed towards the central source of ionization. The diffuse continuum is as described below.

(2) Diffuse continuum: This is the radiation field that is emitted within the cloud (see Figure 3.2). In photoionized gas, the diffuse continuum is far weaker than the reflected continuum. It is most common in stellar atmospheres where the scattering of the incoming photons is highly probable.

(3) Transmitted continuum: This is the total continuum including both the attenuated incident continuum and the diffuse continuum, and is transmitted out from the shielded face of the cloud, away from the continuum source.

3.2.4 Hydrogen density

The hydrogen density "n" represents the total number of hydrogen atoms in the units of cm^{-3}. CLOUDY assumes the total hydrogen density that includes the density of hydrogen in its ionic, molecular and atomic form. In this study, the hydrogen density is one of the key parameters that can be varied within a specific range.

3.2.5 Column density

In general, the cloud is assumed to have a cylindrical shape. As explained before, CLOUDY divides a gas cloud into multiple zones, setting their thickness to be very small such that physical conditions remain constant within a zone. The column density is the total number of particles observed per squared centimeter in the cloud and is given by $N_H = \int nf(r)dr$, where f(r) is the filling factor (the fraction of the volume occupied by the gas), and r is the distance to the cloud.

3.2.6 Ionization Parameter

The ionization parameter (U) is the dimensionless ratio of the ionizing photons that strike the illuminated face of a cloud to the total number of hydrogen atoms.

The following expression defines the ionization parameter:

$$U = \frac{Q}{4\pi R^2 nc}$$

where Q is the total number of continuum photons (per second) emanating from the central source, R (cm) is the radius of the gas cloud, n is the hydrogen density (cm^{-3}) and c is the speed of light (cm s^{-1}).

A large ionization parameter means that more ionizing photons strike the illuminated side of a cloud. The ionization parameter can directly be linked with the degree of ionization inside the cloud. As U increases, more photons strike the illuminated face of the cloud and hence, more ions are produced in the very first zone of the cloud. As we move down to the last zone of the cloud, the ionizing photons encounter more neutral atoms and absorption and because of that the ionizing flux is reduced. Consequently, the ionization drops as a function of radial depth into the cloud. The ionization parameter plays a key role in determining the fractional ionization of ions and their line intensities.

3.3 The Photoionization code XSTAR

XSTAR computes the physical conditions and emission spectra of photoionized gas, and operates in a similar fashion to CLOUDY, however, with differences in the assumptions, atomic database (especially of Fe lines), computational procedure, etc. It assumes a spherical geometry of a gas cloud with the continuum source at the center radiating isotropically. XSTAR becomes more useful, in comparison to CLOUDY, in the treatment of radiative transfer processes for the excited levels of the heavy elements e.g. Fe. However, XSTAR does not assume resonant photoexcitation in its current models, which can effect the line emission of first row ions. XSTAR and CLOUDY do not consider a full treatment of Compton scattering, which can further lead to an overestimation of the scattered continuum at large densities ($>10^{24}$ cm^{-2}). From a variety of input parameters that can be considered in a model construction, the most important are:

(1) Ionization parameter: XSTAR defines the ionization parameter $\xi = \mathrm{L/nR^2}$ (different from CLOUDY), where L is the luminosity of the incident radiation (integrated from 1 to 1000 Ry), n the hydrogen density and R the distance from the continuum source. The steady state of the gas is maintained while calculating the physical conditions in an assumed spherical shell of a gas cloud, i.e. the timescales affecting the radiative transfer solution are very small compared to those for the variation in gas density and incident radiation.

(2) Abundances of elements: XSTAR includes solar abundances (relative to H) of the first 30 elements in the periodic table. The user has an option to change these abundances relative to H otherwise the default abundances are assumed as provided in Grevesse & Sauval 1998. The elements are arranged in the increasing order of nuclear charge and ions in the increasing order of their free charge. XSTAR does not attempt to calculate the ionization for the elements with abundances less than 10^{-15} relative to H.

(3) Radiation Temperature or Alpha: This is parametrized in the units of 10^7 K or keV for a blackbody or bremsstrahlung model respectively. In case of power-law model, it is used to define the power law index, α (in energy).

(4) Covering factor: This parameter determines the geometry which can mimic a complete sphere or partially covering the continuum source. The default value is 1.

(5) Gas density: This is defined as the hydrogen nucleus density (n) and the default value is 1 cm $^{-3}$.

To mimic an X-ray illuminated cloud, XSTAR determines the state of the gas by defining its temperature and the ionic level populations as a function of distance from the continuum source. While deriving the conditions in a gas cloud, the physical processes accompanied by their inverse processes are balanced at every level of an ion as briefly explained in section 3.2. The required quantities e.g. the luminosities of $\sim$ 10000 spectral lines are computed within an energy range of 0.1 eV - 20 keV. To fit the actual spectra, the ATABLE models are generated by "XSTAR2XSPEC" which is a perl script and a major component of XSTAR, and are imported into the X-ray spectral fitting package XSPEC to analyze the data.

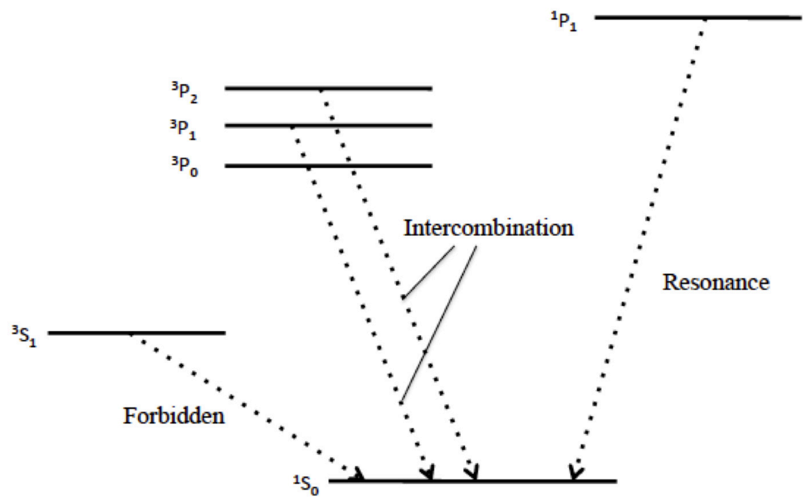

Figure 3.1: Energy state diagram.

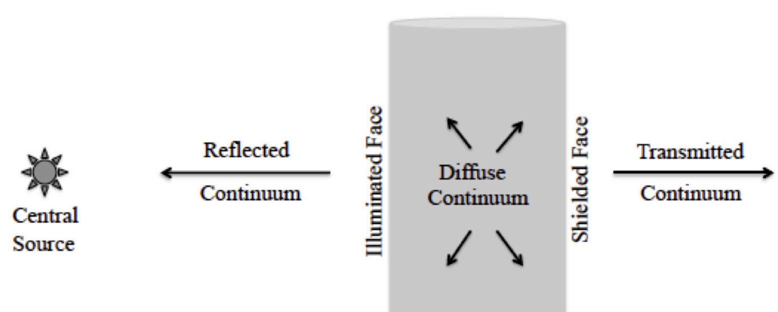

Figure 3.2: Geometrical representation of a slab of gas as assumed in CLOUDY.

Chapter 4: Probing the X-ray Emitting gas in NGC 1068 using *XMM*

4.1 Introduction to NGC 1068

NGC 1068, also known as M77, Arp 37, 3C71, is an early-type barred-spiral (R)SA(rs)b galaxy, located in the constellation Cetus (or Cetus-Aries cloud). It just falls on the celestial equator and hence can be observed from both hemispheres (Bland-Hawthorn et al., 1997). It is the first among six galaxies noticed by Carl Seyfert in 1943 and was observed in the optical waveband, using the Mount Wilson Observatory. NGC 1068 has an absolute blue magnitude of M_B = -21.0 and exhibits a special kind of morphology displaying a "bar within a bar" (Kormendy, 1979, 1982), which may be the structure responsible for the inward flows from galactic radii of $\sim$ 10 kpc to $\leq$ 10 pc (Shlosman et al., 1989). At the center of its host galaxy, a stellar or molelcular bar of size $\sim$ 3 kpc exists (Helfer & Blitz, 1995; Scoville et al., 1988), at the end of which there exist tightly-wound star-forming spiral arms (Planesas et al., 1991). Its bolometric spectrum, extending from radio to gamma rays, is as illustrated in Figure 4.1 (which was generated by using 140 references from NASA/IPAC Extragalactic Database, Bland-Hawthorn et al. 1997). A collage of different color images (in X-ray energy bands) of NGC 1068 is displayed in Figure 4.2.

Due to its proximity, the Seyfert 2 nucleus NGC 1068 is an extensively studied object. Redshift-independent distance estimates place the host galaxy between 10 and 16 Mpc away (e.g. Sofue 1991; Tully et al. 2009). To be consistent with the bulk of the current literature, here I adopt the mean value of 12.65 Mpc from NED[1], such that $1''$ is roughly equivalent to 60 pc. Ground-based narrowband images of the NLR in NGC 1068 show that the optical emission-line gas possesses a biconical morphology, roughly parallel to the major axis of the radio emission, extended northeast and southwest of the nucleus (Pogge, 1988). Narrow-band optical images obtained with the Hubble Space Telescope (HST) revealed that the inner NLR also possesses a biconical morphology (e.g., Evans et al. 1991) and comprises numerous knots and filaments. The hidden AGN is thought to be $0.3''$ south of the optical continuum peak (Capetti et al., 1997), AKA the "Hot Spot" (Kraemer & Crenshaw, 2000).

Optical and UV spectra of NGC 1068, in particular those obtained with the Space Telescope Imaging Spectrograph abroad HST, have been studied in detail e.g., Crenshaw & Kraemer (2000), Crenshaw & Kraemer (2000), Kraemer & Crenshaw (2000) and Kraemer & Crenshaw (2000). The optical emission is dominated by the Hot Spot, spectra of which show emission lines from an extreme range of ionization, e.g. [O I] 6300 to [Fe XIV] 5303 and [S XII] 7611; the latter two are likely the footprint of the X-ray emission line gas. The Hot Spot is also a source of strong

[1]The NASA/IPAC Extragalactic Database (NED) is operated by the Jet Propulsion Laboratory, California Institute of Technology, under contract with the National Aeronautics and Space Administration

scattered continuum radiation. Within 200 pc, on either side of the nucleus, the gas is somewhat less highly ionized, however strong N V 1240, C IV 1550, and [Ne V] 3426 are still present. Photoionization modeling has shown that the gas is ionized by the continuum radiation from the central source, although there are localized regions which show evidence for enhanced ionization due to shocks.

Both red- and blue-shifted emission lines are present on either side of the nucleus (Crenshaw & Kraemer, 2000). Based on kinematic modeling (Das et al., 2006), the observed velocities result from outflow along a hollow bicone, with a half opening angle of 40^o. The axis of the bicone is inclined 5^o with respect to the plane of the sky, with the NE side pointed towards the observer, which is consistent with the morphology of the HI 21 cm emission (Gallimore et al., 1994). The maximum de-projected outflow velocity is 2000 km s^{-1} with a peak 140 pc from the central nucleus, after which there is rapid deceleration to systemic. Although outflowing, photoionized gas is suggestive of radiative acceleration, the velocity profiles are not fully consistent with any simple form of AGN-driven flow (Das et al., 2007; Everett & Murray, 2007). The main issue is that the flow appears to accelerate much more gradually than predicted. One possibility is mass loading, perhaps in the form of interaction with more tenuous ambient gas.

In this chapter, I re-investigate the soft X-ray spectra obtained using the *XMM*/RGS in the context of photoionization models generated with CLOUDY (Ferland et al., 1998). The goals of this study include a reassessment of the physical processes responsible for ionizing the X-ray gas and a better understanding of the relationship between the X-ray emitter and other key components of the nuclear outflow. Progress on these questions will, in turn, lead to a better understanding of the energy and material transport between the active nucleus and the host galaxy.

4.2 X-ray studies

Absorption of the 2-10 keV X-ray continuum in Type 1 AGN by photoionized gas (now generally referred to as "warm absorbers") was first suggested by (Halpern, 1984). Although modification of the X-ray continuum by such an ionized absorber could account for the broad X-ray spectral properties of such sources, ASCA spectra of Seyfert 1 galaxies also revealed evidence for an unabsorbed component of emission (George et al., 1998), particularly in the soft X-ray band (energies < 1 keV). In their analysis of these, George et al. (1998) found that, in many cases, the fit statistics improved when a component of unabsorbed emission-line gas was included. In fact, Netzer (1993, 1996) had predicted that there would be strong soft-X-ray emission lines associated with warm absorbers. The unprecedented X-ray spectral resolution afforded by the XMM-Newton RGS and the Chandra/HETG and LETG have revealed a myriad of emission lines in NGC 1068 as predicted by Netzer (1993).

Furthermore, based on Chandra/HETG observations, Ogle et al. (2000) found extended soft X-ray emission in the Seyfert 1 galaxy, NGC 4151. As it is roughly spatially coincident with the optical [O III] emission and radio continuum, it likely arises in the NLR. Similarly, the NLR is the source of the soft X-ray emission in Seyfert 2 galaxies. For example, X-ray observations of NGC 1068 show an extended region of soft X-ray emitting gas, broadly coincident with the [O III] bicone (Ogle et al., 2003; Young et al., 2001). The extended emission component likely has contributions from both line emission and a small electron-scattered component of the X-ray continuum.

Previous analyses, based upon RGS (Kinkhabwala et al., 2002), Chandra/LETG (Brinkman et al., 2002) and HETG (Ogle et al., 2003) observations have revealed a multitude of emission X-ray lines in NGC 1068. Particularly prominent are strong H- and He-like lines of C, N and O. These are accompanied by weaker highly-ionized lines from Ne, Mg, Si, S and Fe. Chandra observations spatially resolved two peaks of X-ray emission, one centered on the nucleus and the other $3''$ - $4''$ to the NE. The overall emission-line spectrum was found to be consistent in both regions (Brinkman et al., 2002; Ogle et al., 2003). Ogle et al. (2003) suggested that the X-ray emitting gas in the NLR provided a view of the hidden Seyfert 1 nucleus in the scattered light, detected via spectropolarimetry (Miller et al., 1991). Consideration of the ensemble of line measurements has suggested that both photoionization and photoexcitation are important ionization processes for the X-ray emitter (Kinkhabwala et al., 2002; Ogle et al., 2003), with no clear evidence of a collisionally ionized component. However, none of these authors generated detailed photoionization models to analyze the physical properties of the emission-line gas.

More recently, Kallman et al. (2014) analyzed a 450 ks Chandra/HETG spectrum of NGC 1068, using photoionization models generated with the code XSTAR (Kallman et al., 2004). Overall, their results support the claims in Kinkhabwala et al. (2002) and Ogle et al. (2003), specifically that the emission-line gas is photoionized, with some evidence for photoexcitation, and the emission-lines are blue-shifted, indicative of outflows. They found evidence for multiple zones, characterized by a range of ionization parameters (log ξ = 0–3) and column densities. Furthermore, in order to fit the spectra, they allowed the oxygen and iron abundances to vary among the zones. However, they were unable to compare the emission lines of oxygen to those of nitrogen and none of carbon, since *Chandra* MEG has a low effective area at wavelengths > 25 Å (or <0.5 keV) where many of the strong lines of nitrogen and carbon are produced. As a result, Kallman et al. (2014) were unable to determine how their assumed abundances might result within the constraints of nucleosynthesis models. I will revisit these points in the later section.

4.3 A new analysis of XMM data

The observation of NGC 1068 reported here was made by XMM on 2000 July 29 - 30 (OBSIDs 011100101, 0111200201). The standard RGS and PN data products were extracted from the archive, having been produced by the XMM Science Analysis Software (SAS) v6.6.0. The RGS offers a useful bandpass 0.4 - 2.0 keV (6 - 31 Å). Due to the failure of RGS1 CCD7 and RGS2 CCD4 (soon after launch), there are no useful data over the wavelength range 11-14Å (0.9-1.2 keV) and 20-24 Å (0.51-0.62 keV) for RGS1 and RGS2, respectively. Subsequent reprocessing and analysis were performed using a more recent version of SAS[2] (v10.0.0) and various tasks from the *HEAsoft*[3] (v6.9) software suite.

In order to determine the RGS wavelength scale the position of the zeroth or-

[2]http://xmm.esac.esa.int/sas/

[3]http://heasarc.gsfc.nasa.gov/docs/software/heasoft.html

der must be determined. This is not possible using the RGS instrument alone. Thus, I used the *HEAsoft* "XRTCENTROID" task (within XIMAGE v0.2.9) to determine the centroid of the image from the co-aligned PN instrument in the RGS wavelength band. The centroid position was found to be at RA = $02^h42^m40.70^s$, DEC = -$0^o00'46.24''$ (J2000). I estimated the uncertainty of our centroid position to be $1.5''$ based upon repeated trials of the task, i.e., less than one image pixel ($1.6''$ on a side). This X-ray centroid position is consistent with that derived from *Chandra* observations of the source (Young et al. 2001) but is $6.3''$ away from the position assumed in the (SAS v6.6.0) processing of the RGS data that created the archived data products. (The processing software uses the position supplied by the principal investigator). I also noted that our centroid position is $5''$ away from the X-ray centroid position determined by Kinkhabwala et al. (2002) for this *XMM* observation, attributable to improvements in attitude determination software between the original processing of the data and the current archived version. As the RGS energy scale is determined by the angle a photon has been dispersed relative to the zeroth order position, this difference in attitude solution does not affect the line energy determination relative to that performed by Kinkhabwala et al. (2002). Further to the uncertainty on photon energy related to the statistical uncertainty in determination of the centroid and therefore the dispersion angle, there is an additional uncertainty in the absolute energy scale that corresponds to a 1σ uncertainty in velocity of 105 km s^{-1} at 20Å.

Given the above, I reprocessed the RGS data from both OBSIDs using SAS v10.0.0 to produce co-added source and background spectra for each RGS, based on our X-ray centroid position. The total exposure times were 84.7 ks and 82.5 ks for RGS 1 and 2 respectively. The mean source count rates (in the 0.4-2 keV band) were 0.568±0.003 cts/s and 0.516±0.003 cts/s for RGS 1 and RGS 2 respectively. The background comprised 20% of the total count rate.

4.4 Spectral Analysis

4.4.1 Initial line fitting

The source spectral (without background subtraction), background and response files obtained after reprocessing the data (as discussed above), were loaded into XSPEC (Arnaud, 2010) to create the background-subtracted source spectra from RGS 1 and 2, as shown in Figure 4.3 (orange color). This methodology allows XSPEC to perform the background subtraction and preserve the full statistical information (e.g. counts per bin) from the data. The RGS spectra contained > 10 counts in most of the channel range used allowing us to utilize the χ^2 statistic for fitting.

Inspection of the spectra revealed several prominent lines (Figure 4.3) including those from H-like and He-like transitions of O, C, N, Ne, Mg and Si. Of particular interest are the very prominent triplets that arise from He-like species, such as N VI, O VII and Ne IX, that can yield constraints on the gas density and excitation mechanism (Porquet & Dubau, 2002).

To extract the parameters for these lines, narrow sections of the data (within a specific energy range) were fit using XSPEC. Each line profile was modeled using a

Gaussian component whose flux, width and energy were allowed to vary (Table 4.1). The Galactic column density was accounted for in the spectral analysis by using the neutral absorption model TBABS (Wilms et al., 2000). The column density for the TBABS component was allowed to vary between 2.92 $\times 10^{20}$ cm^{-2} (Dickey & Lockman, 1990) and 3.53 $\times$ 10^{20} cm^{-2} (Kalberla et al., 2005), to account for the uncertainty in this quantity. The best-fit value of the Galactic column pegged at the high end of this range in the fit and, therefore was initially fixed at 3.53 $\times$ 10^{20} cm^{-2} (but see Section 4.6.1). The continuum close to each line was fit with a power-law component and the photon index was allowed to vary. The best fit line parameters are detailed in Table 4.1 for lines above the threshold of observed flux $> 10^{-6}$ photons cm^{-2} s^{-1}. I tabulated 1σ errors on each parameter (i.e., calculated at 68% confidence).

As expected, my measured emission-line fluxes are in good agreement with those of (Kinkhabwala et al., 2002). However, the RGS fluxes are $\sim$ 2 greater than those measured in *Chandra*/HETG spectra (Kallman et al., 2014; Ogle et al., 2003). The difference is due to the much larger extraction region for the RGS. To illustrate this, in Figure 4.4 I show the RGS and *Chandra*/HETG extraction windows, overlaid on a *Chandra*/ACIS image. Clearly, much of the X-ray emission-line region is outside the Chandra window.

Fe M- and L-shell transitions (Fe XIV to Fe XXIV) are heavily blended with H- and He - like lines of Ne (Figure 4.3), therefore the strengths of these lines could not be usefully constrained. The higher-order transition lines of Mg, Si and S are barely resolved due to the low sensitivity of the RGS in the wavelength regime (6-10 Å).

4.4.2 Kinematics

I have identified the observed lines using the expected laboratory energies from the National Institute of Standards and Technology (NIST), supplemented by the Kentucky atomic database (Table 4.2). Most of the emission lines show a significant blue-shift relative to the host galaxy (cz = 1137±3 km/s; Huchra et al. 1999), indicating an origin in outflowing gas, as previously found by other authors (e.g. Kinkhabwala et al. 2002).

Based on the strongest, most isolated lines from He-like N and O and H-like C, N, and O, we found two kinematic components, with the N VI and O VII f lines having more negative radial velocities than the N VII and O VIII Ly lines (See Figure 4.5). However, the velocities of the latter are consistent with those of the N VI and O VII r lines, within the uncertainties. Unfortunately, the Ne IX and Ne X lines are weaker and heavily blended with Fe lines, hence it is impossible to see if the same trend is present. Overall, the radial velocities are on the same order as that measured for [O III] 5007, v_{rad} =160 km s^{-1} (Crenshaw et al., 2010), which suggests that the X-ray and optical emission-line gas have similar kinematics. Note that these velocities are not de-projected (directed away from the line-of-sight) and the actual outflows may be much faster (e.g. Das et al. 2006). As I also note in Section 4.6.1, while the kinematics are consistent with distinct low and high ionization zones, their radial velocities cannot be well constrained with these data.

Velocity widths (FWHM) were determinable for a few strong lines (Table 4.2). The strongest lines, e.g., N VI f and O VII f are resolved using RGS, with velocity widths FWHM 926 and 1003 km s^{-1}, respectively. This is quite close to the value measured for [O III] 5007, FWHM 1060 km s^{-1} (Whittle, 1992), again indicative of similar kinematics for the X-ray and optical emission line gas. The values are in excess of the radial velocities and most likely result from the superposition of different kinematic components along our line-of-sight.

4.5 Photoionization Modeling

4.5.1 Inputs to the Models

Previous analyses for the soft X-ray emitting gas in NGC 1068 have used selected line measurements to explore the conditions in the emitting gas (Kinkhabwala et al., 2002). Here I aim to construct a self-consistent photoionization model for the X-ray emitter. To this end, I have made use of the photoionization code, CLOUDY version C10.00, last described by Ferland et al. (2013). As usual, my model results depend on the choice of input parameters, specifically: the spectral shape of the incident radiation or SED, the radial distances of the emission-line gas with respect to the central source, the number density of atomic hydrogen (n) and column density (N_H) of the gas, and its chemical composition. Given the large radial distances ($>$ 10s of pc) of the emission-line gas, I have assumed open, or slab-like, geometry. The models are parameterized in terms of the dimensionless ionization parameter U, the ratio of ionizing photons per nucleon at the illuminated face of the slab.

4.5.1.1 The Ionizing Continuum

I assumed an SED in the form of a broken power law $F_\nu = K\ \nu^\alpha$, with $\alpha =$ 1.0 below 13.6 eV, $\alpha = 1.7$ from 13.6 eV to 0.5 eV, and $\alpha = 0.8$ from 0.5 keV to 30 keV, where α is the energy index. I also included a low energy cut-off at 1 eV and a high energy cutoff at 100 keV.

Since our view of the central source is blocked in NGC 1068, I estimated the ionizing luminosity using an "isotropic" quantity, specifically the [O IV] 25.89μm emission line (see Meléndez et al. 2008). The [O IV] flux, detected with the *Infrared Space Observatory*-Short Wave Spectrometer, is approximately 1.9x10^{-11} ergs cm^{-2} s^{-1} (Lutz et al., 2000), which corresponds to a line luminosity $L_{oiv} \approx 10^{41.53}$ ergs s^{-1}. Using the linear regression fit to L_{oiv} and the 2-10 keV ($L_{2-10keV}$) luminosity for Seyfert 1 galaxies calculated by Melendez et al. (2007), we estimate $L_{2-10keV} \sim 10^{43.8}$ ergs s^{-1}, which, for a bolometric correction of ~ 30 (Awaki et al., 2001), yields $L_{\rm bol} \sim 10^{45.3}$ ergs s^{-1}. The corresponding mass accretion rate is $\dot{M} = \frac{L_{\rm bol}}{\eta c^2}$, or 0.35 $M_\odot$ yr^{-1}, for $\eta = 0.1$. Interestingly, given a black hole mass of 1.5x10^7 $M_\odot$ (Greenhill & Gwinn, 1997), the central source is radiating at approximately its Eddington limit. Based on these values and our assumed SED, I found the ionizing luminosity $L_{\rm ion} \sim 10^{44.2}$ ergs s^{-1} and $Q \sim 10^{54.4}$ photons s^{-1}.

4.5.2 Preliminary tests with CLOUDY

A multitude of emission lines of different ions are observed in the soft X-ray spectrum of NGC 1068. Comparing their observed intensities with those predicted by CLOUDY helps constrain the parameter space of an ion within a range of U and N_H. To obtain a first order understanding of the parameter space applicable to the emission line gas, I first ran CLOUDY in several regimes of interest and examined the line ratios from those runs. Most of the calculations were based on the various ions of oxygen (the most abundant element after H and He), which were compared with the ions of other elements.

4.5.2.1 Fractional ionization vs. Column density Plots

As a first step, to understand the distribution of ions of an atom in a cloud, the fractional ionizations of O I, O III, O VII and O VIII are plotted against the column density at two different values of U (Figure 4.6). The column density is analogous to the distance into the cloud, in other words, the highest column density (10^{24} cm^{-2}) is for the last zone, furthest from the continuum source. The observed intensities of O ions are predominantly produced at two values, U = 1, 10. In Figure 4.6, the first zones (low N_H) of the cloud are dominated by the highly ionized ions (e.g. O VII and O VIII), whereas penetrating further into the cloud (high N_H), the low ionized ions become more abundant. The physical meaning of these results is that at larger distances into the cloud more material is encountered that leads to more scattering and absorption of photons, and thus their chances of survival to the last zone of the cloud become very unlikely. By increasing U (more photon flux, Figure 4.7), the dominant region of a particular ion shifts towards higher N_H as the fully stripped ions occupy the inner zone of the cloud. Due to the higher flux of ionizing photons considered in Figure 4.7, the ionization region of neutral oxygen (O I) is suppressed by that of the highly ionized ions. Therefore, the dominant ion can be estimated at a particular value of the ionization parameter and the column density.

4.5.2.2 Line Intensity Contour Plots

As predicted by CLOUDY, the line intensity contours of He- and H-like ions of oxygen (Z=8) and magnesium (Z=12) are displayed in Figures 4.8, 4.9, and 4.10, 4.11 respectively.

In Figures 4.8 and 4.9, the red and blue contours represent the high and very low intensity levels (in units of ergs cm^{-2} s^{-1}), respectively. The parameter space of low U and high N_H indicates the dominant region of O VII ions, whereas at high U and low N_H highly ionized ions (e.g. O VIII) tend to prevail. This behavior corroborates the interpretation of fractional ionization plots. To observe a highly ionized specie, more ionizing photon flux is required at a given column density. On the contrary, for O VIII, which is a more highly ionized ion than O VII, the dominant region (red contours, Figure 4.9) exists at high column and high ionization parameter, since at low column fully stripped ions would prevail. The white space (at bottom right) in Figure 4.9 illustrates the prevailing region of low ionized ions, as the ionizing flux is inadequate to strip off more electrons.

A conspicuous feature in Figure 4.8 is the "sweet spot", where the sharp turn in the contour lines at U of 10^0 demonstrates the highest intensity of [O VII] within the specified range of N_H. A similar spot can be identified in the contours of Figure 4.9

but at higher U which is due to the higher ionization potential of O VIII as compared to that of [O VII].

Similar kind of tests were performed for the ions of C, N, Ne, Mg, etc. The contours of a high-Z specie (e.g. Mg) are shown in Figure 4.10. The intensity contours of He-like and H-like ions of magnesium, [Mg XI] and Mg XII, look similar to those of [O VII] and O VIII, respectively. The only noticeable difference is the occurrence of the sweet spots of [Mg XI] and Mg XII at higher ionization parameters than that of oxygen ions. To further constrain the parameter space of various ions, the contours of the intensity ratios are considered next.

4.5.2.3 Line Intensity Ratio Contours

To recap: the ionization parameter scales with the flux of ionizing photons produced by the central continuum and the column density is the number of particles in a given cylinder per unit area of the cloud. So far a number of diagnostic tests have been performed with CLOUDY to constrain the parameter space (as a function of U and N_H) of the prominent emission lines as observed in the soft X-ray spectrum of NGC 1068.

The intensity ratio contours of O VII *f*/O VIII are shown in Figure 4.12. The intensity ratio of O VII *f* to O VIII at a given column density decreases with an increase in the ionization parameter. The interpretation of this behavior is that at higher ionization parameter more photons are available to ionize O VIII as compared to O VII *f*, indicating the highly ionized gas is dominated by O VIII production.

Similarly, at a given ionization parameter, with an increase in the column density (means encountering more material in the line-of-sight), the intensity ratio of O VII *f*]/O VIII increases. This pattern shows that at higher column densities and low U, the lower ionized ions of oxygen (than O VII *f* and O VIII) exist. As a result more white space is seen at the bottom right in Figure 4.12. The contours of high-Z ions' ratios e.g. Ne IX *f*, Ne X, Mg XI *f* and Mg XII, follow a similar pattern to that discussed earlier for O VII *f* and O VIII. As illustrated in Figures 4.9 and 4.11, the sweet spots of the contours of high-Z ions occur at higher values of U. Also evident in Figures 4.13 and 4.14, the larger ratios of the ions of high-Z element exist at higher U values compared to the low-Z element. The intensity ratio contours of He-like and H-like ions of Ne and Mg are displayed in Figures 4.13 and 4.14.

To further constrain the physical parameters of the XNLR gas, one could proceed by comparison of the observed line intensities to those of predicted by CLOUDY. In the X-ray spectrum, strong emission lines of H- and He-like ions of C V β, C VI α, [N VI], N VII, O VIII, Ne IX *f*, Ne X, Mg XI *f* and Mg XII are observed. In the plots described next, their intensity ratios are normalized to that of [O VII] (being the strongest line with the largest line flux, as observed in the soft X-ray spectrum of NGC 1068).

The intensity contours of the ratios of the He- to H-like ions of four elements N, O, Ne and Mg are combined in Figure 4.15. For each element, the two intensity contours of the observed ratios, with its lower and upper limits within an error of 1σ, are shown. Due to a small difference between the ionization potentials of O and N, their ions' ratios tend to overlap on the same parameter space at different values of U and N_H. The ions of high-Z species e.g. Ne and Mg have an overlapping region around the higher ionization parameter of 10^1 and column density of 10^{21} - 10^{22} cm^{-2}. Measurements of the Ne lines are subject to some uncertainty, since these lines are heavily blended with Fe lines, as seen in the RGS spectra of NGC 1068.

4.5.3 Elemental Abundances

My initial approach was to find an approximate solution (U and N_H) for the gas by comparing the ratio of intensities of selected strong emission lines in the data with those predicted by the CLOUDY model, as described in Section 4.5.2. The line ratios selected were for the strengths of H-like and He-like ions relative to O VII *f* 22.10 Å (the latter was selected by virtue of being the strongest line detected in the RGS data), similar to the approach used in the analysis of the RGS spectrum of the Seyfert 1 galaxy NGC 4151 by Armentrout et al. (2007).

I first generated CLOUDY photoionization ATABLE models assuming solar abundances (Grevesse & Sauval 1998) and the parameter space constrained from the contour plots. This initial comparison revealed no single-zone gas solution that could adequately describe the observed line ratios. Specifically, models with solar abundances over-predicted the strongest oxygen lines, O VII *f* 22.10 Å and O VIII Ly, relative to the lines from other abundant elements/ions, in particular, and He-like carbon and nitrogen. Interestingly, in photoionized gas the X-ray emission lines from second-row elements are primarily produced by recombination or, for permitted transitions if the lines are optically thin, by photoexcitation. The other strong features in the RGS spectrum include radiative recombination continua (RRCs) which are obviously formed via recombination. Hence, the strengths of these features are quite sensitive to relative elemental abundances. Notably, it has been argued that optical and UV recombination lines are more reliable indicators of elemental abundances than collisionally excited forbidden lines, which are typically used to estimate elemental abundances in optical spectra, due to the sensitivity of the latter on temperature and density fluctuations (Peimbert, 1967).

In the analysis of RGS spectra of the Seyfert 1 NGC 3516, (Turner et al., 2003) found that the model fit was improved by assuming both super-solar N/O and sub-solar C/O abundance ratios. They argued that this was consistent with conversion of carbon to nitrogen via the CNO-cycle in intermediate mass stars (M $\leq$ 7 $M_\odot$; e.g. Maeder & Meynet 1989), and that fairly large N/O ratios, e.g., a few times solar, could occur in stars with initially roughly solar abundances. However, the NGC 1068 spectra also show strong carbon lines (see Figure 4.3), which are not consistent with the loss of carbon, at least if the overall abundances were approximately solar. In studies of H II regions in the Milky Way, evidence has been found for a C/O gradient, with a C/O ratio unity, while O/H ratio was roughly solar, at radial distances $\leq$ 7 kpc (e.g. Esteban et al. 2005). The enhancement of carbon in the Milky Way interstellar medium could be due to either stellar winds from massive stars, $8 \leq M/M_\odot \geq 80$ (Henry et al., 2000), or a combination of high-metallicity massive stars and low-metallicity low-to-intermediate mass stars, $0.8 \leq M/M_\odot \leq 8$ (Carigi et al., 2005). In either case, if the carbon were significantly enhanced in a star with otherwise solar abundances, the conversion of carbon-to-nitrogen described above could lead to both high C/O and N/O ratios while O/H evolved as Z/Z_o. Based on this, I assumed that metallicities of pro-genitor stars were solar (Asplund et al., 2005), although with C/O approximately 3 solar, as compared to the roughly twice solar values found by (Esteban et al., 2005). I further assumed that nucleosynthesis brings the overall metallicity to 1.5 solar, but with all the added carbon going into the production of nitrogen. The resulting abundances, with the log values, relative to H by number, are as follows: He: -0.83; C: -3.06; N: -3.36; O: -3.13; Ne: -3.90; Na: -5.59; Mg: -4.23; Al: -5.39; Si: -4.32; P: -6.42; S: -4.71; Ar -5.43; Ca: -5.49; Fe -4.33; and Ni: -5.61. Here the N/H and C/H ratios are 6 and 3.2 $\times$ solar, respectively, while the other heavy element abundance ratios are 1.5 $\times$ solar. It should be noted that Brinkman et al. (2002) suggested super-solar nitrogen abundance and Kallman et al. (2014) required non-solar heavy element abundances for their photoionization models. Based on the strong C and Fe emission in the RGS spectra, there is no evidence for depletion of these elements onto dust grains. Therefore I did not include cosmic dust in the models.

4.6 Spectral Fitting Results

The range in ionization states detected in these spectra suggests the presence of two distinct components of emission-line gas, therefore my approach was to generate two model grids with CLOUDY. Consideration of the ratio $\frac{\mathrm{NVI}f}{\mathrm{OVII}f}$ and $\frac{\mathrm{NeX}}{\mathrm{OVIII}}$ suggested that these zones lie in the ranges logU $\sim$ -1 to 0, $\log N_H \sim$ 20 - 22 and logU $\sim$ 0 - 2, $\log N_H \sim$ 20 - 23.

4.6.1 The Final Model

To refine my solution, the RGS spectra were compared to a model comprising two 'candidate' model zones. Based upon the initial results from the line ratio analysis (see Section 4.5.2.3), I re-ran CLOUDY with model step intervals of 0.1 in the log of U and N_H, across the ranges -2 < logU < 2 and 20 < logN_H < 24, using the elemental abundances noted above (in Section 4.5.3). Initially, the resonance lines of the He-like triplets (only) were underpredicted compared to the forbidden lines. Thus, to boost the strength of these resonance lines, we included micro-turbulence of 35 km s^{-1}. This corresponds to a FWHM = 82 km s^{-1}, which is significantly less than that of the resolved lines discussed in Section 4.4.2, which likely result from the superposition of kinematic components along our line-of-sight. Following Porter et al. (2006), I then created a FITS format ATABLE from the CLOUDY output. To facilitate a comparison of the model tables with the ensemble of line results we performed spectral fitting of the RGS data using our ATABLE.

My final model was comprised of two zones (LOWION and HIGHION), each absorbed by the Galactic line-of-sight column density, parameterized using TBABS. The value of TBABS was initially set to $N_H = 3.53\times10^{20}$ cm^{-2} (Kalberla et al., 2005), but in the final fit the value was allowed to vary. Fitting the model to the data showed the model lines to be systematically too narrow to account for the observed line ensemble. Therefore, to account for the Doppler broadening, I smoothed the model spectra using a Gaussian function equivalent to σ = 365 km s^{-1} (FWHM = 852 km s^{-1}) for LOWION and σ = 1170 km s^{-1} (FWHM = 2732 km s^{-1}) for HIGHION, The LOWION smoothing is consistent with the measured widths for N VI *f* and O VII *f* (see above). The fitting was allowed to proceed until the reduced χ^2 was minimized; the final model parameters are listed in Table 3. In the process, the outflow velocities for LOWION and HIGHION converged on values of 215 km s^{-1} and 166 km s^{-1}, respectively. However, these values overlap within the uncertainties, as suggested in Section 4.3.2. Also, the fitting returned a Galactic column of $5.43^{+0.44}_{-0.28} \times 10^{20}$ cm^{-2}, somewhat larger than the value from Kalberla et al. (2005). However, there is evidence for absorption by low-ionization gas covering the NLR of NGC 1068 (see Kraemer & Crenshaw 2000; Kraemer et al. 2011), and it is plausible that the extra column of neutral gas is associated with that.

As shown in Figure 4.3, we obtained a reasonable (i.e., reduced χ^2 = 1.99) fit to the data with two components, the relative contributions of which are shown in Figure 4.16. The contributions to χ^2 are shown in Figure 4.17, which illustrates that most of the mismatch to the data is due to under-predicted of the emission below 17Å. In order to determine and compare the predicted emission line fluxes to the intrinsic line luminosity, which is necessary to determine the covering factors of the emission-line gas, n_H must be determined for each component, which requires fixing their radial distances. For the sake of simplicity, I assumed that LOWION and HIGHION are co-located. As a reference point, I assumed they are at a distance R = 50 pc from the central source, which is consistent with the fact that most of the X-ray emission arises within the central 100 pc (see Ogle et al. 2003). Note that the X-ray emission-line ratios are not sensitive to density over the range expected for X-ray emitters in the NLR (e.g., $< 10^6$ cm^{-3}; Porquet & Dubau 2002). Also, I do not have any strong constraints of the location of the emission-line gas, except that the emission is centrally peaked. However, this distance is reasonable given the distribution of scattered continuum (Crenshaw & Kraemer, 2012) and the probability that much of the emission from the inner 30 pc is heavily attenuated (e.g., Kraemer & Crenshaw 2000; Kraemer et al. 2011). Using the value of Q derived in Section 4.5.1.1, I obtained n = 15 cm^{-3} and 275 cm^{-3} for HIGHION and LOWION, respectively. One additional check on whether the models are physically plausible is the requirement that the depth of the model, R = N_H/n, is less than the components radial distance, R (e.g. Blustin et al. 2005, crenshaw2012). For these model parameters, ΔR/R = 0.02 and 0.68 for LOWION and HIGHION, respectively.

Based on the fitting, LOWION and HIGHION contribute 0.96 and 0.04 of O VII f and 0.14 and 0.86 of O VIII Ly-α, respectively. Using these fractional contributions, I computed the predicted emission-line fluxes from each component and the total flux. The former are computed by comparing the predicted O VII f and O VIII Ly-α fluxes to the absorption-corrected fluxes, taking into account the fractional contributions of each component, in order to derive a scaling factor for each component. Then the remaining line fluxes are computed by multiplying the ratios of their fluxes to those of O VII f or O VIII Ly-α by the derived scaling factors. The final values are listed in Table 4.1, along with the observed and absorption-corrected fluxes. The fits for the individual lines are good overall, with the predictions for most of the stronger lines (i.e., with fluxes & 3×10^{-4} photon cm^{-2} s^{-1}) within 30% of the absorption-corrected values. The discrepancies include C V Heβ and Heδ, which are relatively weak and in a region where determining the continuum level is non-trivial and N VII Ly-α is somewhat under-predicted.

In addition to emission lines included in Table 4.1, I also compared the predicted and measured RRCs, using the same relative contributions from the two model components (see Table 4). Although I detected the O VIII RRC, the feature is too heavily blended with the surrounding emission for us to have been able to determine the width and flux accurately. Overall, the predicted fluxes fit the measured values reasonably well. The model-predicted electron temperatures correspond to widths of kT = 4.0 eV and 44.4 eV, for LOWION and HIGHION, repsectively. While the LOWION value is on the same order as the measured values of the He-like RRCs, the HIGHION prediction is several times that of the measured H-like RRCs. This is likely the result of the difficulty in fitting these broader features. However, both the models and data confirm that the emission-line gas possesses temperatures consistent with photoionization.

As noted above, the greatest mismatch between the model and the data is in the region 10-17 Å, which shows a heavy blend of emission lines of Fe XIV-XXIV with those from Ne IX, Ne X, and O VIII (for a more complete identification of the iron lines see Kinkhabwala et al. 2002). HIGHION predicts that the maximum ionization states of iron are spread from Fe XVII to Fe XXI, within the observed range, however the predicted line fluxes are quite weak and essentially make a negligible contribution to the model spectrum (see Figure 4.16). The underprediction may be the result of the incomplete atomic data for iron, specifically rates for fluorescence following inner shell ionization.

4.6.1.1 Model-derived Covering Factors

Having obtained a reasonable fit to the RGS spectrum with my two component model, I calculated the covering factors (C_f) for each component by comparing the emitting area, the ratio of the emission-line luminosities to their model-predicted fluxes, to the surface area of a sphere surrounding the central source. As I mentioned above, I assume that both LOWION and HIGHION are 50 pc from the source, which sets n for each component for the value of U for each component, and thus the predicted emission line-fluxes. Based on our spectral fitting, the total luminosity of the O VII *f* line emitted by LOWION is 2.5×10^{40} ergs s^{-1}. Dividing by the predicted flux, 0.215 ergs cm^{-2} s^{-1}, the total emitting surface area of LOWION is 10^{41} cm^{-2}, which corresponds to a covering factor $C_f = 0.35$. Based again on my spectral fitting, for HIGHION, the total luminosity of O VIII Lyα is 1.5×10^{40} ergs s^{-1}, while the predicted flux is 0.051 ergs cm^{-2} s^{-1}, from which I derived an emitting surface of 2.5×10^{41} cm^{-2} and $C_f = 0.84$. Although the covering factors are physically possible, in the sense that they are less than unity, the value for HIGHION requires that this component subtends a larger solid angle than the emission-line bicone, even if the bicone were filled (e.g. Das et al. 2006). I will revisit this point in Section 4.7.3.

4.6.1.2 UV and Optical Constraints in the X-ray Emission-line Gas

Although the ionization parameters for both emission components are significantly higher than those determined for the UV and optical emission-line gas (e.g. Kraemer et al. 1998, kraemer2000b), except for the "CORONAL" component of the Hot Spot (Kraemer & Crenshaw, 2000), the LOWION model predicts strong O VI $\lambda\lambda$ 1031.9, 1037.6. Scaling the predicted flux by the emitting area determined from the O VII f line, the predicted O VI luminosity is 1.9×10^{41} ergs s^{-1}, which corresponds to an observed flux $F_{ovi} \sim 1.0\times10^{11}$ ergs cm^{-2} s^{-1} (note that the contribution from HIGHION is more than two orders of magnitude less, hence can be ignored).

NGC 1068 was observed with the Hopkins UltraViolet Telescope (HUT), aboard the space shuttle Columbia (Kriss et al., 1992), through two circular apertures of 18" and 30", hence encompassing the region of strong X-ray emission (e.g. Young et al. 2001). They measured $F_{\rm ovi}$ = 3.74 ($\pm$ 3.1) 10^{-12} ergs cm^{-2} s^{-1}. While the emission-line fluxes reported by Kriss et al. were not corrected for extinction, based on the ratio of He II λ 1640 (from HUT) to He II λ4686 (Koski, 1978), they derived an extinction $E_{B-V} = 0.16$, assuming an intrinsic 1640/4686 ratio of 7.0 (Seaton, 1978). Using the UV extinction curve in Seaton (1979), the corrected $F_{ovi} \approx 2.5\times10^{11}$ ergs cm^{-2} s^{-1}, which indicates that LOWION contributes 40% of the O VI emission. Based on this, my model meets the constraints from the UV emission. Also, it is possible that some regions of UV and optical emission are undetectable due to extinction (see discussion in Kraemer et al. 2011), but could be detected in the X-ray, in which case LOWION accounts for an even smaller fraction of the intrinsic UV emission.

Given the model parameters of the Hot Spot CORONAL component (LogU = 0.23; $\log N_{\rm H}$ = 22.6; Kraemer & Crenshaw 2000), it could contribute to the overall X-ray emission. However, neither of our components have similar parameters. Furthermore, while CORONAL was optimized to match the observed [S XII] λ7611, the peak ionization states are S IX and S XV for LOWION and HIGHION, respectively. Finally, forcing the inclusion of a component similar to CORONAL into the spectral fitting produced statistically unacceptable results. This suggests that the conditions that give rise to the [S XII] emission are not typical of the X-ray NLR as a whole.

4.7 Results

4.7.1 Total Mass and Mass-loss Rates

Based on my model results and constraints on the covering factors of each component, I can determine the total mass of the X-ray emission-line gas, M_{tot}, for a given radial distance, R. Assuming the gas lies in shells, the thickness of which are constrained by the model-derived values of N_H, the total mass is given by:

$$M_{tot} = 4\pi\ R^2\ N_H\ \mu\ m_p\ C_f$$

where m_p is the mass of a proton and the factor μ is the mean atomic mass per proton (I assumed = 1.4, primarily from the contribution from helium). For the fiducial distance, R = 50pc, and derived model parameters, I obtained M_{tot} = 8.7×10^4 $M_\odot$ and $4.7\times$ 10^5 $M_\odot$ for LOWION and HIGHION, respectively. Note, given the possibility that the emission-line gas lies at greater radial distance, M_{tot} could be somewhat greater. I estimated the mass loss rates, $\dot{M}$, as follows (Crenshaw et al., 2003):

$$\dot{M} = 4\pi\ R\ N_H\ \mu\ m_p\ C_f\ v$$

where v is the outflow velocity. Using v_{rad} in place of v, I obtain mass loss rates of $\dot{\mathrm{M}} \sim 0.38$ M$_\odot$ yr^{-1} and 0.06 M$_\odot$ yr^{-1} for the two components. Clearly, $\dot{\mathrm{M}}$ would be greater if the gas were at a larger radial distance, as is the case for M$_{\rm tot}$, or if the outflow velocities were greater than v$_r$.

The derived values of M$_{\rm tot}$ and $\dot{\mathrm{M}}$ are roughly the same as those determined from the *Chandra*/HETG spectrum by Kallman et al. (2014), and, based on my estimate of L$_{\rm bol}$, the latter is on the same order as that of the fueling rate. From the results of the STIS long slit spectral analysis (Kraemer & Crenshaw 2000a,b), I estimated that within a single slit position, at PA = 202^o, the total amount of emission-line gas is 6×10^3 M$_\odot$. Scaling this quantity by the ratio of the dereddened [O III] λ5007 flux from the STIS spectra and the [O III] flux in ground-based spectra (Bonatto & Pastoriza, 1997), dereddened as per the discussion in Section 3.2.3, I estimated a total mass of the optical emission-line gas of $\sim 3.8\times10^4$ M$_\odot$. This is on the same order mass of ionized gas determined from spectra obtained with the *Gemini*/Near-Infared Field Spectrograph by Riffel et al. (2014), hence it is unlikely that I have grossly underestimated the mass of optical emission-line, due to regions of heavy extinction (e.g. Kraemer et al. 2011). Therefore, these results indicate that the X-ray emission-line gas is a major, if not dominant, component of ionized gas in the NLR.

4.7.2 Thermal and Pressure Stability

The predicted gas pressures at the ionized faces of LOWION and HIGHION are 3.1×10^7 dyn cm^{-2} and 1.9×10^7 dyn cm^{-2}, respectively, which indicate that, given uncertainties in the model parameters, these components are roughly in pressure equilibrium if co-located. In contrast, the predicted gas pressure for the UV/optical emission-line gas from the Hot Spot is 2.5×10^{9} dyn cm^{-2} (based on the model parameters in Kraemer & Crenshaw (2000)). Therefore, UV/optical knots would not be pressure-confined by the X-ray emission-line gas. In that case, one would expect to see a drop in the density of the optical/UV gas with radial distance. However, given the large pressure differential, the density drop would be much more rapid than observed (Kraemer & Crenshaw, 2000). This suggests other scenarios, such as creation/evaporation of clouds out of/into the X-ray medium (Krolik & Kriss, 2001) or in situ acceleration of gas that has rotated into the illumination cone (Crenshaw et al., 2010), rather than outflow and expansion of individual knots.

In Figure 4.18, I showed the logT- logU/T, or S-Curve, plot generated with my assumed SED and abundances. Note that there is only one region with pronounced negative slopes, indicative of strong instabilities; the overall stability is the result of the high metal abundances in my models (see Bottorff et al. 2000). The insert shows that both components lie on stable, i.e., positive-sloped sections of the S-curve. While HIGHION does lie close to an unstable region, given that the AGN is radiating close to its Eddington limit, it is unlikely that it will experience an ionizing flux increase that would drive it into instability.

4.7.3 Structure of the X-ray NLR

As noted in Section 3.2.2, the model-derived covering factors are physically possible. However, it is difficult to reconcile such large values considering that the optical emission SW of the nucleus is heavily attenuated by the disk of the host galaxy (Kraemer & Crenshaw, 2000) and that X-ray emission from the inner 30 pc appears to be absorbed by gas outside the bicone (Kraemer et al., 2011). Hence, it is likely that there is more X-ray emission line gas than that detected in the RGS spectra. If so, the covering factors could be significantly greater and could easily exceed unity for HIGHION.

Both HIGHION and LOWION are matter-bounded and, in such cases, emission-line fluxes can be increased to an extent by increasing N_H. This would, correspondingly, decrease the required emitting surface areas and, hence, the covering factors. However, in the case of HIGHION, N_H is constrained by the $\Delta R/\mathrm{R}$ condition (see Section 4.6.1). One way around this is if the emission-line gas consists of a number of matter-bounded components at increasing radial distances. As an example, in Figure 4.19, I showed the incident and transmitted continuum for HIGHION; clearly, there is no significant attenuation of the incident continuum, hence highly-ionized gas could exist in the "shadow" of a component similar to HIGHION, i.e., subtending the same solid angle with respect to the ionizing radiation. LOWION also produces weak attenuation. Assuming that density decreases with R, as observed with the optical emission-line gas (Kraemer & Crenshaw, 2000), each additional zone could be at roughly the same ionization state. There is some evidence for this scenario, in the sense that the optical continuum profile shows clear radial structure (Crenshaw & Kraemer, 2000). A series of separate shells would effectively create a large column density without violating the ΔR/R constraint[4], and thereby reduce the required covering factor.

This proposed structure of the NLR has implications for the origin of the polarized optical emission in NGC 1068, which is presumably due to scattering by free electrons. In their analysis of optical polarimetry of NGC 1068, Miller et al. (1991) determined that the temperature of the scattering medium is 3×10^5 K; for comparison, the predicted temperature for HIGHION is 5.15×10^5K. However, the required column density of the medium is $\geq 10^{22}$ cm^{-2} (Pier et al., 1994), or an order of magnitude greater than that of HIGHION. On the other hand, if the emission line region is comprised of a series of zones, described above, the total column density of high-ionization X-ray emission-line gas would be significantly larger than that of HIGHION. Therefore, I suggest that gas with physical conditions similar to those of HIGHION is the source of the scattered/polarized emission.

[4]adding what are essentially identical ATABLES would not change the fit to the RGS spectra hence it is impossible to test this scenario via XSPEC

Table 4.1: Comparison of the Observed and Predicted Emission-line Fluxes.

LineID	Observed[a]	Absorption-corrected	Total Model[b]	Low U[c]	High U[d]
C V Heβ	1.16±0.31	3.24±0.86	1.09	1.09	–
C V Heδ	2.45±1.30	4.62±2.08	0.59	0.59	–
C VI Lyα	9.48±0.41	23.35±1.01	16.57	9.55	7.02
C VI Lyβ	1.76±0.21	3.18±0.38	2.58	0.87	1.71
C VI Lyγ	0.60±0.14	0.95±0.22	1.41	0.53	0.88
C VI Lyδ	1.07±0.16	1.94±0.29	0.87	0.41	0.46
N VI Heγ	0.47±0.14	0.67±0.20	0.42	0.42	–
N VI r	3.32±0.48	6.08±0.87	4.13	3.62	0.51
N VI i	0.93±0.37	1.72±0.68	1.80	1.80	–
N vI f	7.37±0.12	13.20±0.60	9.77	9.77	–
NVII Lyα	6.01±0.26	8.92±0.39	6.45	1.99	4.46
N VII Lyβ	0.95±0.09	1.45±0.16	1.62	0.43	1.19
N VII Lyγ	0.40±0.16	0.53±0.16	0.88	0.27	0.61
N VII Lyδ	0.35±0.10	0.40±0.10	0.51	0.19	0.32
O VII r	4.96±0.28	7.85±0.68	5.30	3.97	1.33
O VII i	1.00±0.44	1.94±0.70	3.13	3.13	–
O VII f	9.25±0.18	14.99±0.29	12.57	12.07	0.50
O VII Heβ	0.73±0.15	0.99±0.22	0.88	0.54	0.34
O VII Heγ	0.67±0.09	0.88±0.14	0.36	0.36	–
O VII Heδ	0.38±0.08	0.49±0.12	0.30	0.30	–
O VIII Lyα	5.37±0.30	7.44±0.64	8.94	1.25	7.69
O VIII Lyβ	0.96±0.44	1.22±0.28	1.59	0.32	1.27
N IX r	1.74±0.13	2.08±0.15	1.46	0.45	1.01
N IX f	1.11±0.15	1.32±0.18	0.79	0.38	0.41
N IX Heβ	0.21±0.09	0.24±0.09	0.45	0.16	0.29
N X Lyα	1.34±0.11	1.52±0.12	2.07	–	2.07
Mg XI rif	0.90±0.17	0.96±0.19	1.46	–	1.46
Mg X Lyα	0.27±0.11	0.29±0.12	0.95	–	0.95

[a]Fluxes obtained by fitting a Gaussian to each line as identified in the combined spectra of RGS 1 and RGS 2; all fluxes × 10^{-4} photons cm^{-2} s^{-1}.

[b]Absorption-corrected line fluxes predicted by CLOUDY in the total model.

[c]Fluxes predicted by CLOUDY for LOWION, after scaling to that of O VII f.

[d]Fluxes predicted by CLOUDY for HIGHION, after scaling to that of O VIII Lyα.

Table 4.2: Observed Energies and Velocity Shifts Relative to Systemic

LineID	$\lambda_{\rm th}{}^a$ (Å)	$E_{\rm th}{}^b$ (eV)	ΔE^c (eV)	Velocity Shift^d (km s^{-1})
C V Heβ	34.9728	354.526	0.444±0.085	-490±80
C V Heδ	32.7542	378.529	0.969±0.205	-680±120
C VI Lyα	33.7342	367.533	0.333±0.019	-270±50
C VI Lyβ	28.4663	435.547	0.582±0.065	-400±70
C VI Lyγ	26.9900	459.369	0.618±0.040	-4000±80
C VI Lyδ	26.3572	470.399	0.459±0.135	-290±10
N VI Heγ	23.7710	521.578	0.685±0.161	-400±110
N VI r	28.7870	430.695	0.376±0.042	-260±60
N VI i	29.0815	426.333	0.342±0.069	-240±70
N VI f	29.5343	419.797	0.495±0.018	-350±60
NVII Lyα	24.7792	500.356	0.318±0.045	-190±70
N VII Lyβ	20.9095	592.957	0.498±0.141	-251±102
N VII Lyγ	19.8261	625.358	0.513±0.161	-250±110
N VII Lyδ	19.3614	640.368	0.841±0.235	-390±130
O VII r	21.6020	573.947	0.483±0.046	-250±80
O VII i	21.8044	568.620	0.539±0.111	-280±90
O VII f	22.1012	560.983	0.708±0.029	-380±70
O VII Heβ	18.6270	665.615	1.516±0.174	-680±120
O VII Heγ	17.7682	697.787	1.414±0.221	-610±130
O VII Heδ	17.3958	712.722	1.145±0.310	-480±150
O VIII Lyα	18.9725	653.493	0.337±0.036	-150±80
O VIII Lyβ	16.0067	774.577	-0.111±0.194	+40±120

^{a}Theoretical wavelengths from NIST/Kentucky atomic database.

^{b} Theoretical line energies.

^{c} $\Delta E = E_{\rm obs}$ - $E_{\rm th}$ with uncertainties of 1σ (68% confidence level).

^{d} The quoted errors are statistical (1σ) and systemic (derived from the centroid position uncertainty), combined in quadrature.

Table 4.3: Photoionization Model Parameters[a]

Component	logU	$\log N_H$	Velocity
LOWION	$-0.05^{+0.02}_{-0.02}$	$20.85^{+0.03}_{-0.05}$	215^{-22}_{+12}
HIGHION	$1.22^{+0.01}_{-0.01}$	$21.2^{+0.00\ d}_{-0.001}$	166^{+23}_{-39}

[a]Fit statistic: $\chi^2 = 9805.83$ using 4926 pulse-height analyzer bins. Reduced $\chi^2 = 1.99508$ for 4915 degrees of freedom.
[b] N_H in units of cm^{-2}.
[c] Velocity offset (km s^{-1} from systemic.
[d] Upper limit fixed based in $\Delta R/R$ constraint (see section 4.6.1).

Table 4.4: Measured and Model-predicted RRC Parameters

Ion	kT (eV)	Flux[a]	Model Total	LOWION	HIGHION
C V	2.39±0.50	11.25±0.90	6.51	6.51	–
C VI	8.13±2.10	9.25±0.91	9.62	2.48	4.03
N VI	1.01±0.33	1.40±0.13	2.56	2.56	–
N VII	6.56±0.30	4.38±0.16	3.03	0.77	2.26
O VII	4.50±0.25	2.97±0.30	4.46	4.15	0.31

[a]All fluxes $\times 10^{-4}$ photons cm^{-2} s^{-1}.

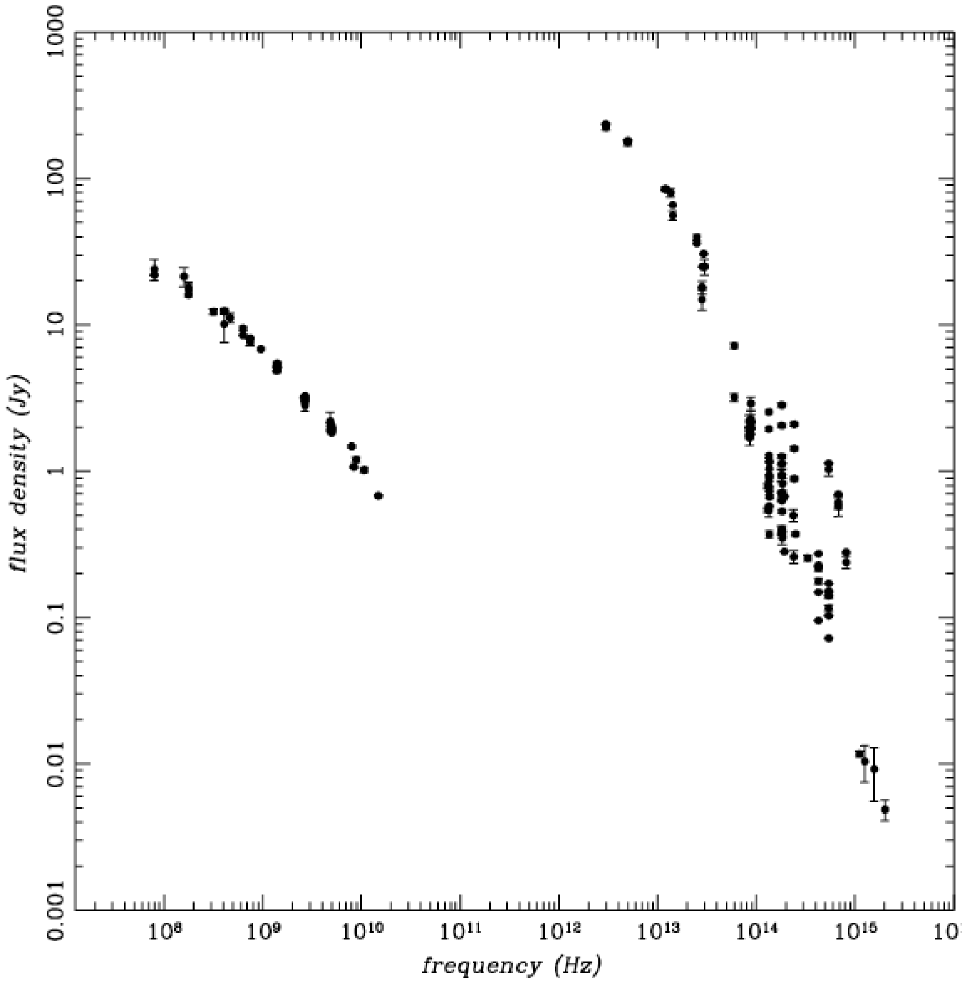

Figure 4.1: The bolometric spectrum of NGC 1068 from radio to gamma rays.

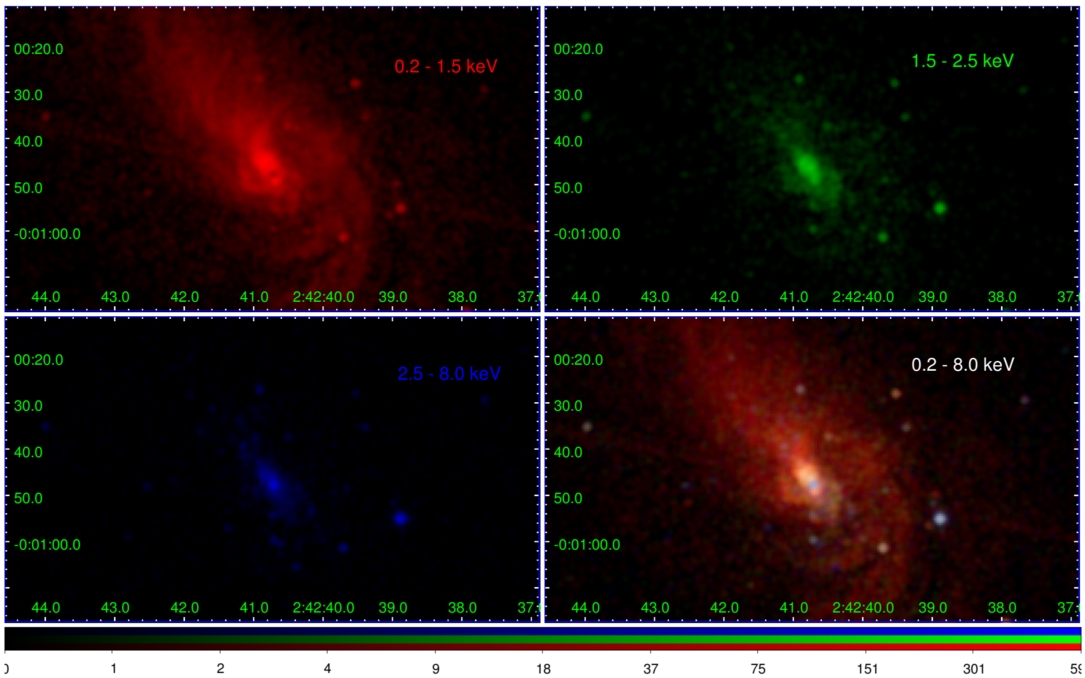

Figure 4.2: The color images of NGC 1068 displayed in soft (0.2-1.5 keV), medium (1.5-2.5 keV) and hard (2.5-8.0 keV) X-ray bands. At the bottom right, all three color images are combined. The X-axis is the right ascension and the y-axis is the declination.

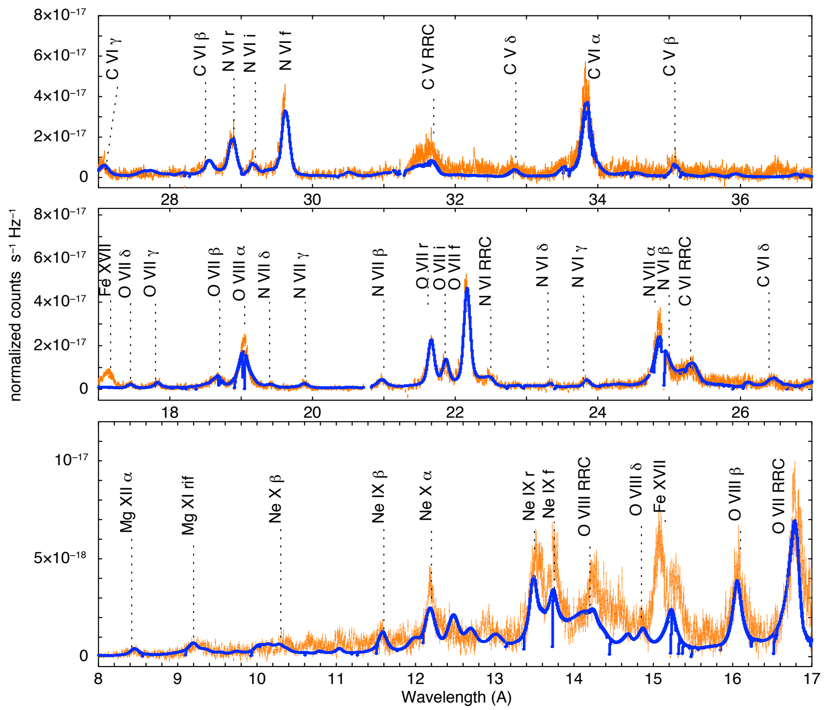

Figure 4.3: Total model comprising both zones (blue) compared to the combined RGS 1 and RGS 2 spectrum (orange). Note that the model produces a fairly good fit, except for $\lambda < 17$Å, as discussed in Section 4.6.1.

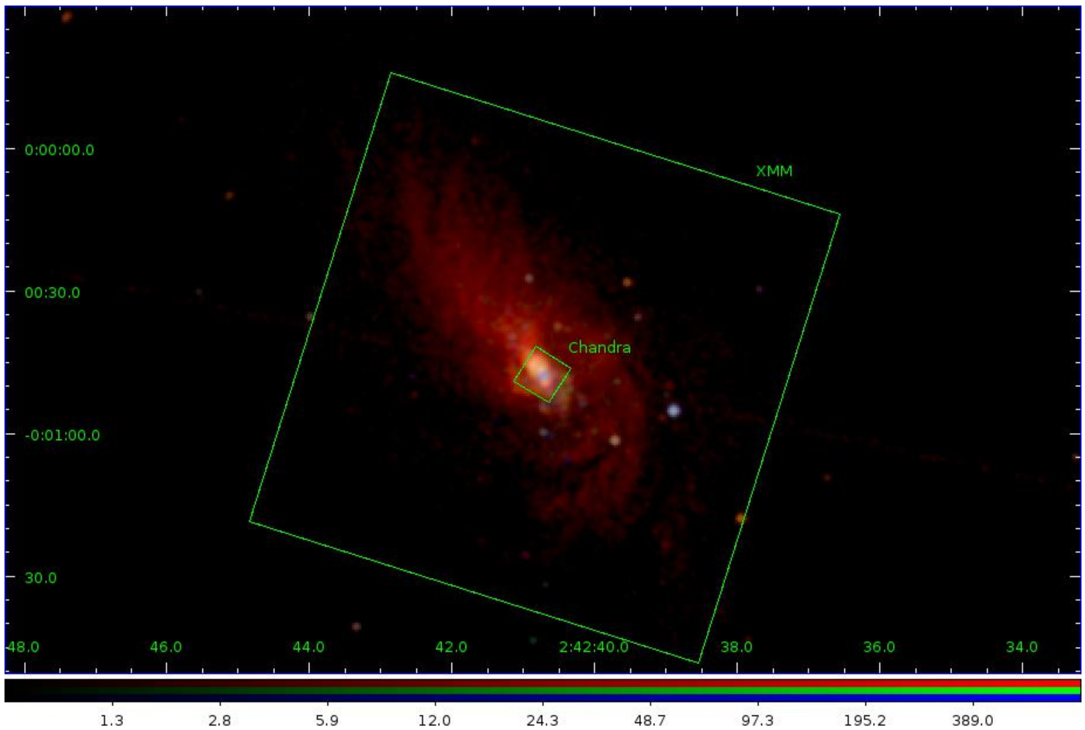

Figure 4.4: *XMM*/RGS and *Chandra* extraction cells, overlaid on the *Chandra*/ACIS image. Declination is along the y axis, right ascension is along the x axis, and the colors in the image correspond to the following: red, 0.2-1.5 keV; green, 1.5-2.5 keV; and blue, 2.5-8.0 keV. The extraction cells are square with size of $\sim 100''$ and $\sim 9''$ for *XMM*/RGS and *Chandra*/HETG, respectively, oriented with respect to the roll angles for these observations (Kallman et al., 2014; Kinkhabwala et al., 2002).

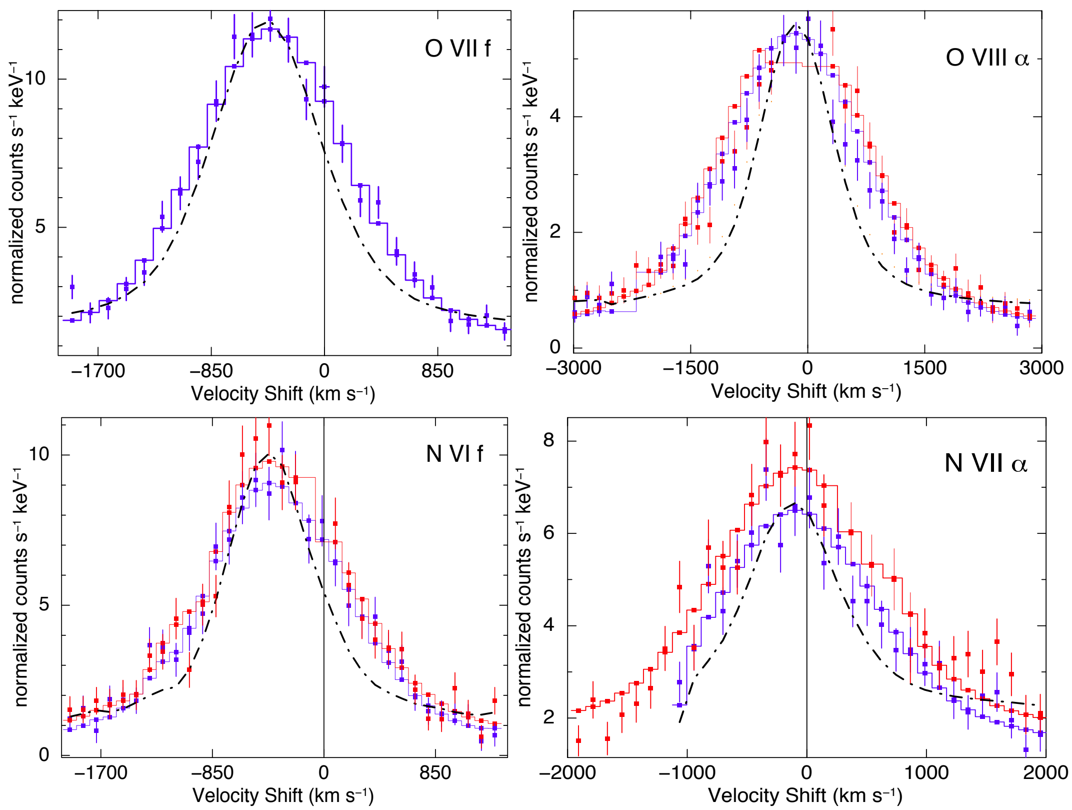

Figure 4.5: RGS 1 (red) and RGS 2 (blue) line profiles for O VII *f*, O VIII Lyα, N VI *f*, and N VII, relative to the nucleus. The systemic velocity of the host galaxy is represented here by the solid line at 0 km s^{-1}. Note the blueshifts of each emission-line peak. Each line is broader that the instrument profile, which is represented by the dotted line.

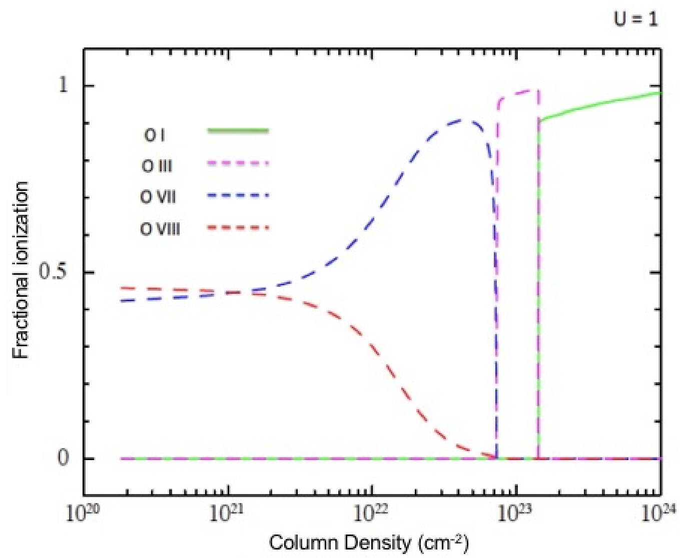

Figure 4.6: Fractional ionization (Y-axis) is plotted against the column density in cm^{-2} (X-axis) for different ions of oxygen. The colors used for different ionization states are labelled. The higher the column density, the greater the distance into a cloud. The low columns are dominated by highly ionized ions of O while low ionized ions are more abundant at higher columns.

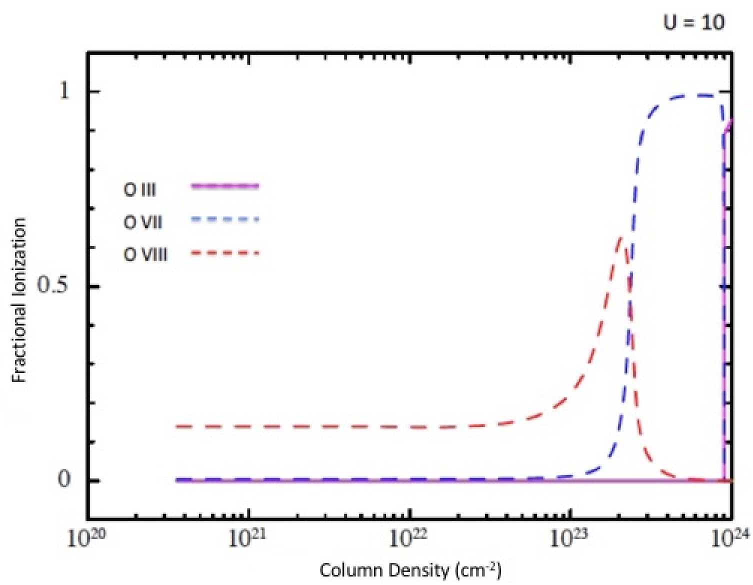

Figure 4.7: Similar to Figure 4.6, but plotted at higher ionization parameter of U = 10. As U increases, the ionization regions of the ions considered here shift towards the last zones of the cloud since completely stripped ion of oxygen prevails over the smaller column densities. This is due to the higher flux of ionizing photons.

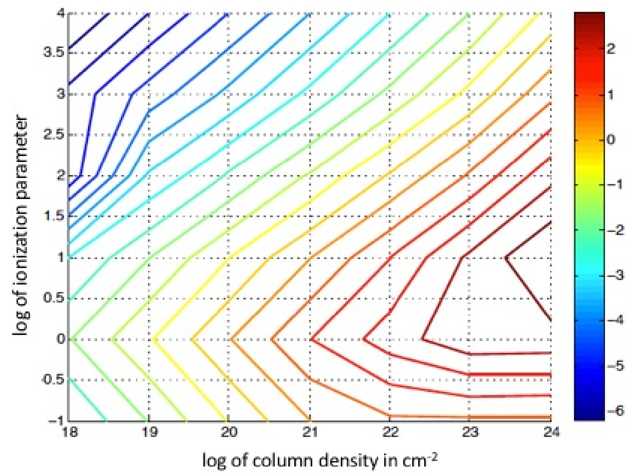

Figure 4.8: The intensity contours of [O vii] (22.10 Å) are displayed, where the abscissa is plotted as the column density in units of cm^{-2} and the ordinate the ionization parameter. Color bars represents the intensity levels of the contour lines in units of ergs cm^{-2} s^{-1}. The sharp turn in the contours names as "sweet spot" represents the highest intensities at given U and N_H. The sweet spot of low ionized [O vii] occurs at U =1.

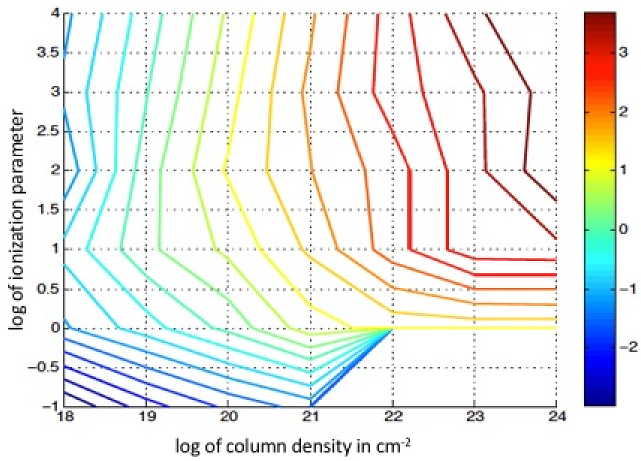

Figure 4.9: Similar to Figure 4.8 but plotted for highly ionized O VIII α (18.98 Å), where the sweet spot occurs stretches between U = 10^0 - 10^2. In the bottom right, at high column densities the photon flux is not sufficient to generate highly ionized O VIII and hence at this parameter space the line intensities predicted by CLOUDY are negligible.

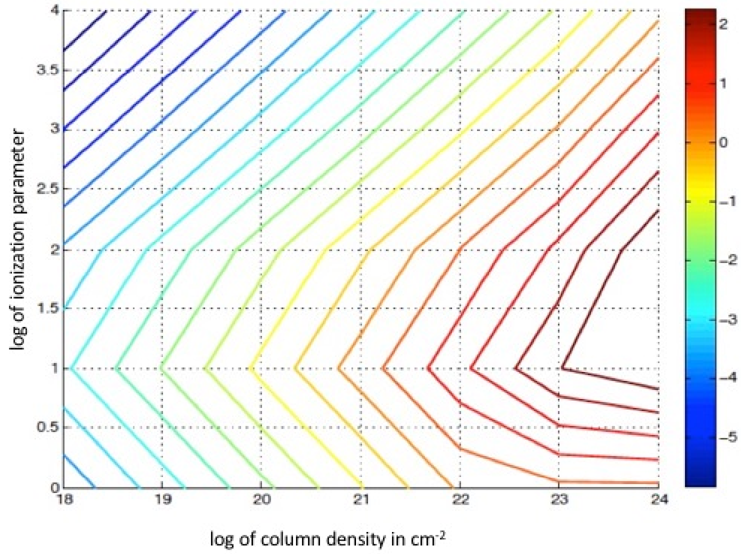

Figure 4.10: Contours similar to above figures are plotted for [Mg XI] (9.23 Å) but differ in the intensity levels of lines at a given parameter space. Because of the high atomic number (high ionization potential) of Mg, the sweet spot occurs at higher U in contrast to O ions.

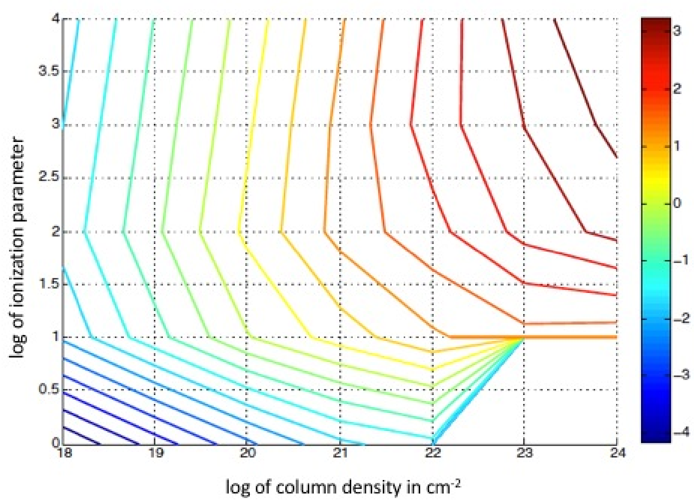

Figure 4.11: The contour lines of H-like Mg XII follow the similar trend as of H-like O VIII (in Figure 4.9).

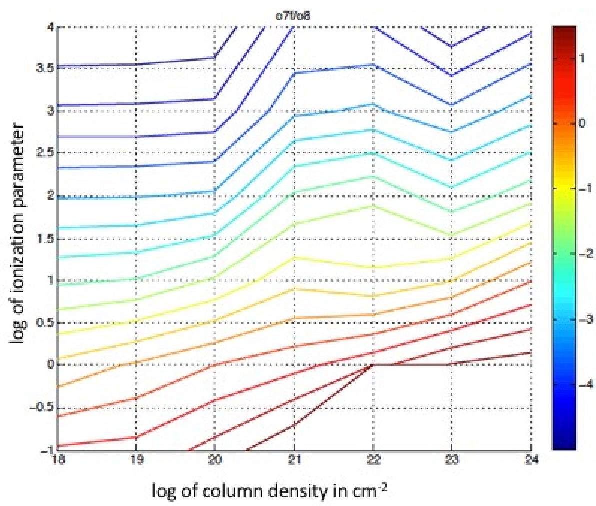

Figure 4.12: Here I plotted the contours of ratios of intensities of [O VII] to O VIII. The abscissa is the column density in units of cm^{-2} and the ordinate the ionization parameter. The intensity ratios decline as U increases, that indicates O VIII is more abundant at higher U. At the right bottom, these ratios are negligible due to the dominance of low ionized ions at higher N_H and lower U. Similarly, on the top of the plot, fully stripped ions are dominating in comparison to low ionized ions and hence make the ratios f [O VII]/O VIII very insignificant.

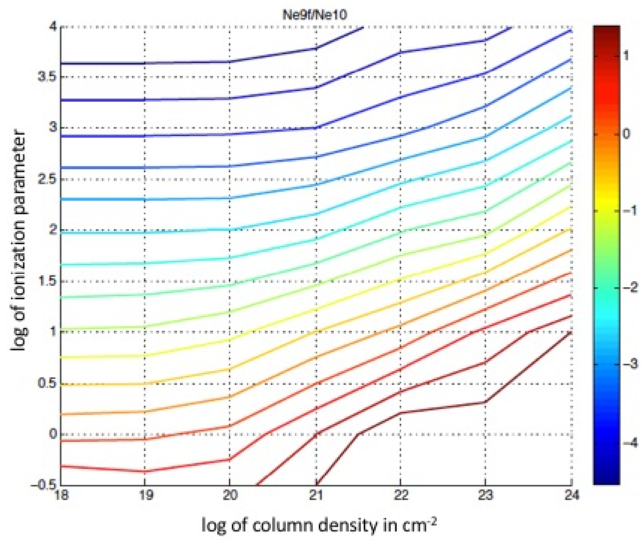

Figure 4.13: Similar to Figure 4.12 but plotted for the ratio of [Ne IX] (13.67 Å) to Ne X (12.14 Å). Similar to the oxygen contours, the bottom right white space on the plot illustrates the region dominated by low-ionized Ne ions. At such higher column densities and low ionization parameters, we do not notice any significant contribution of [Ne IX] and Ne X in that parameter space.

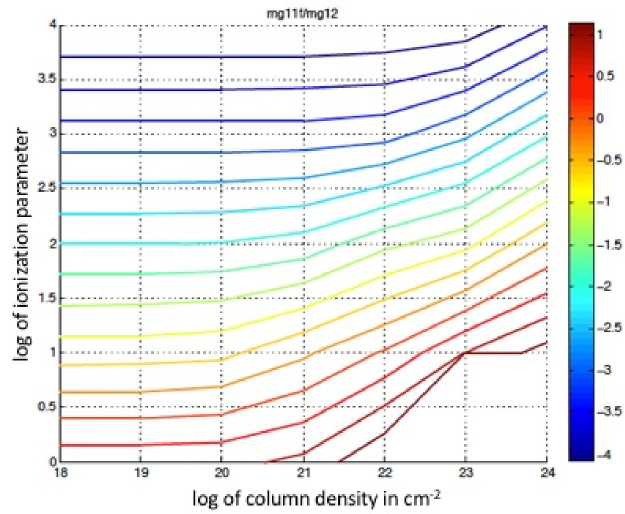

Figure 4.14: Similar to Figure 4.13, the intensity ratio contours of [Mg XI] (9.316 Å) and Mg XII (8.42 Å) are plotted.

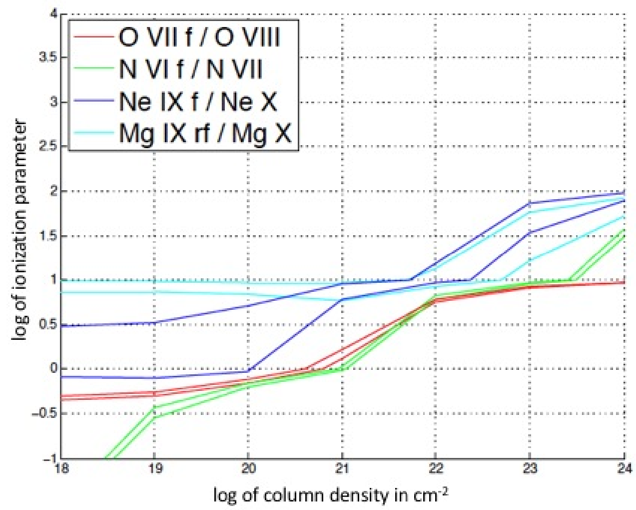

Figure 4.15: Contours of intensity ratios of He- and H-like ions of various elements are combined. N and O ratios tend to overlap over the same region, whereas high-Z Ne and Mg line ratios overlap in the high ionization parameter space. At higher column densities and lower U (bottom right), photon flux is not sufficient to produce these ratios. On the most of the top grid (above U of 2), there is a higher probability of obtaining the fully stripped ions.

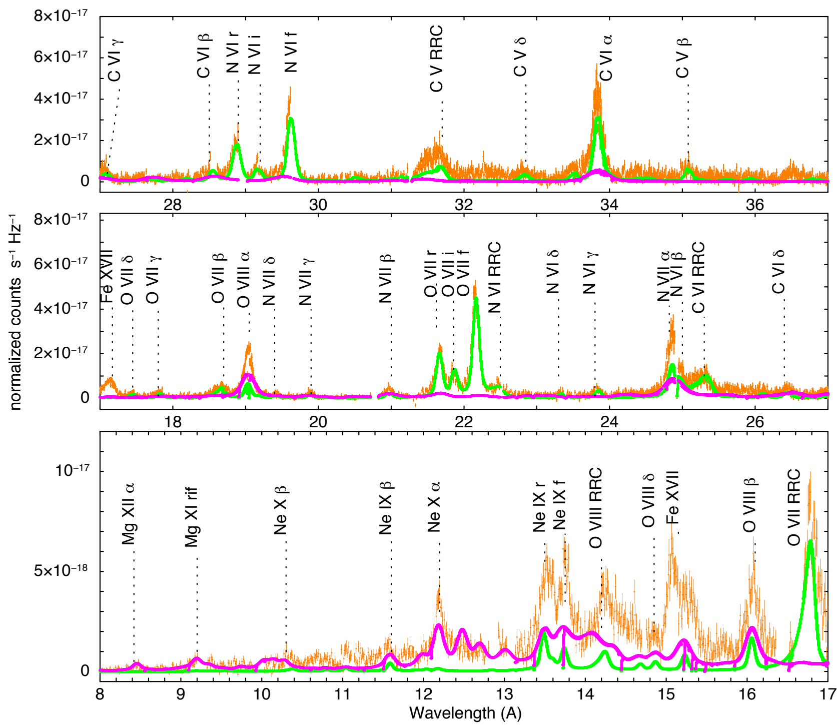

Figure 4.16: Individual model components, LOWION (green) and HIGHION (purple), compared to the combined RGS 1 and RGS 2 spectrum. As noted in the text, LOWION contributes most of the emission from the He-like C, N, and O, while HIGHION contributes most of the H-like N and O and both H- and He-like Ne emission.

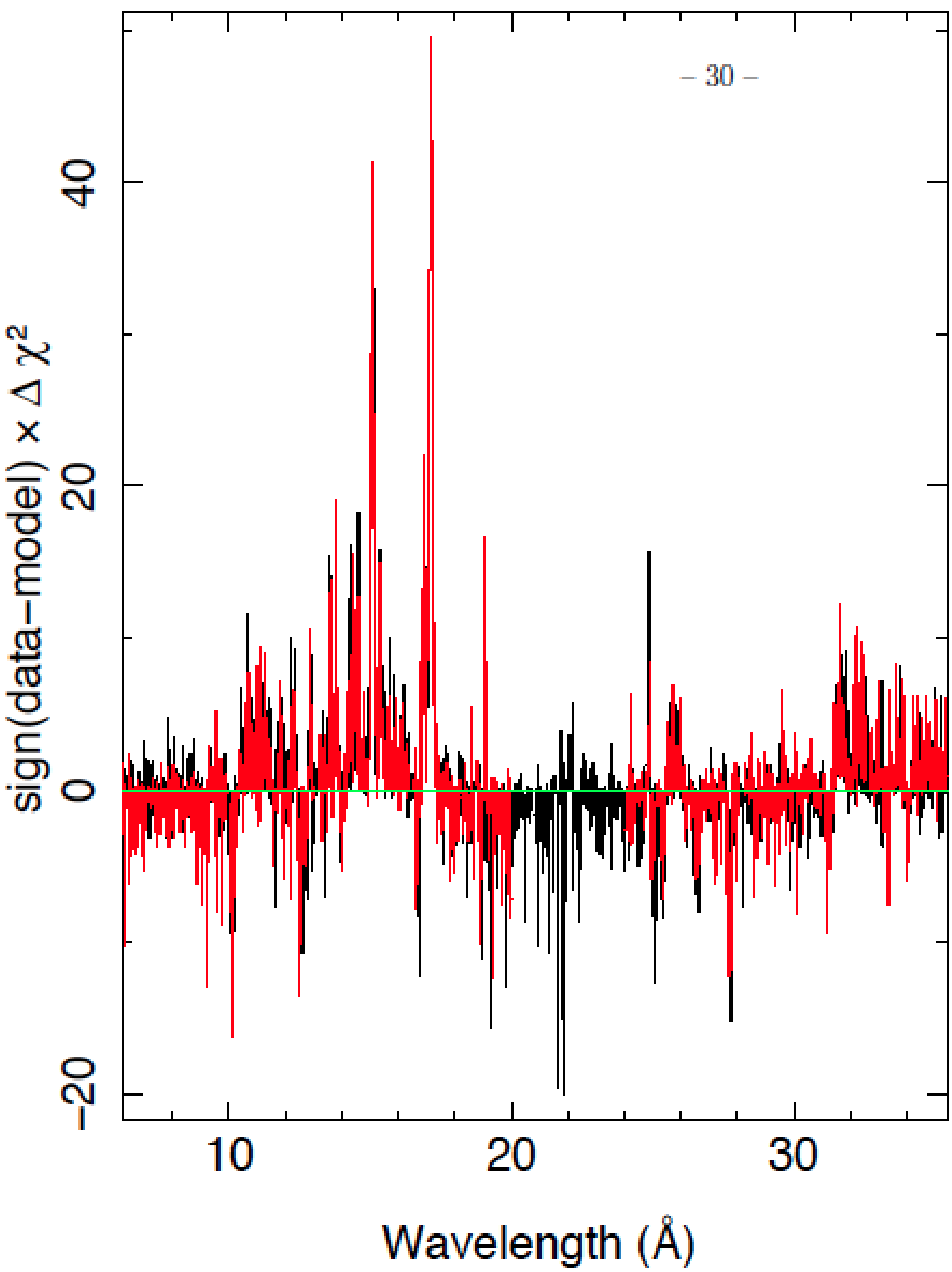

Figure 4.17: Contributions to χ^2 for the data compared to the best-fitting two-zone model from XSPEC, detailed in Section 4.5. RGS 1 data are shown in black, and RGS 2 data are shown in red. The gaps are where the dispersed RGS spectrum falls on a nonoperational CCD chip. The greatest mismatch occurs in the range of 14-17Å and is primarily due to the underprediction of emission lines from M-shell Fe ions.

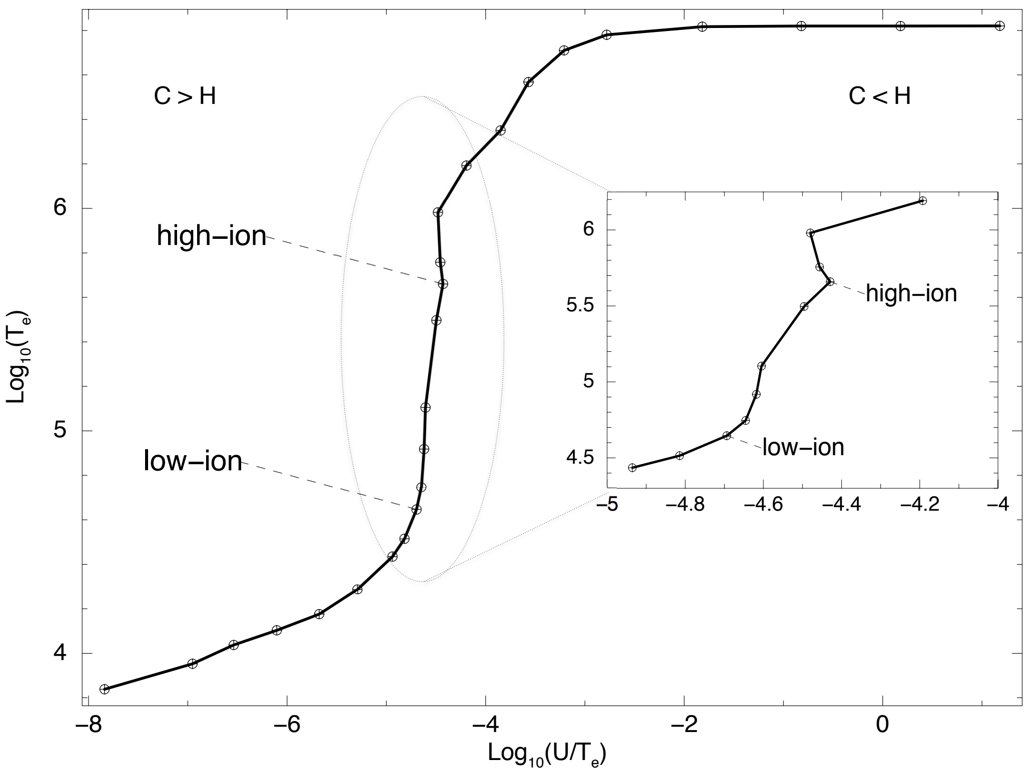

Figure 4.18: Stability curve for a range of ionization parameter from 10^{-3} to 10^{7} and our assumed SED and abundances. The regions at the left and right of the curve are where the cooling and heating dominate, respectively, as indicated. The two gas components identified from our photoionization modeling, LOWION and HIGHION, lie on stable, i.e., positively sloped, portions of the curve (which is most clearly seen via the inset), although the latter is close to an unstable region.

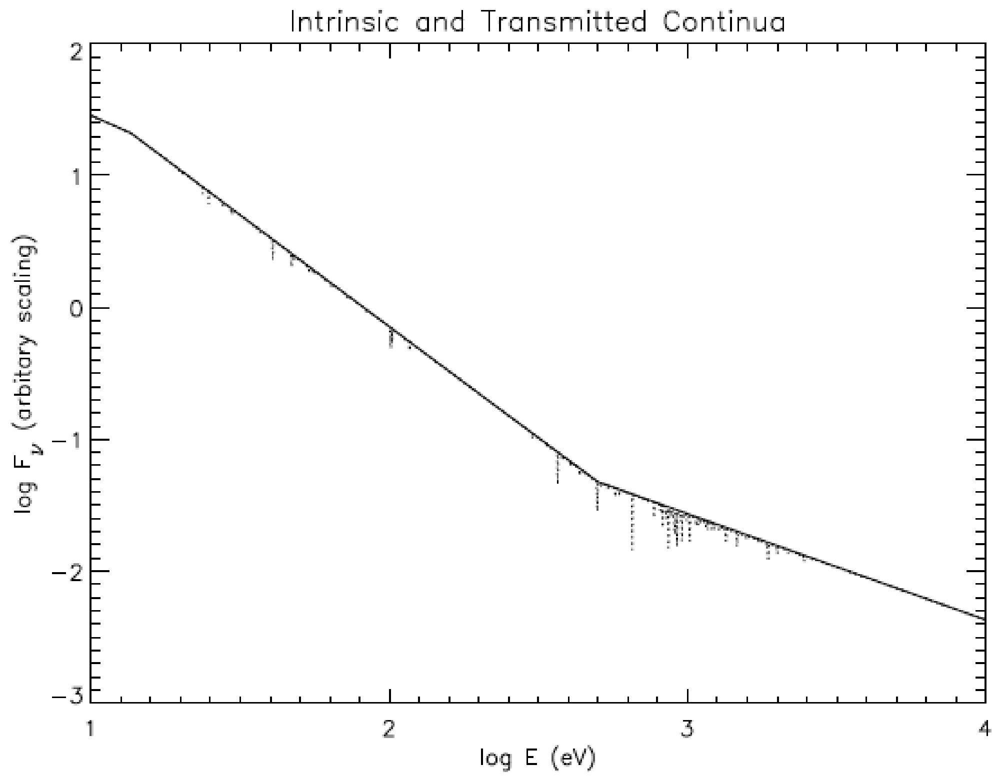

Figure 4.19: Incident (solid line) and transmitted (dotted line) model continua for the component HIGHION. As shown, there is little attenuation of the ionizing radiation as it is transmitted; hence, gas can be in a similar state of ionization in the "shadow" of the component.

Chapter 5: Constraints from the *Chandra* data on the location and geometry of the X-ray reprocessed gas in NGC 1068

5.1 Observations and Data Analysis

The data from the *Chandra* X-ray Observatory presented here are based upon ten observations (Table 5.1) made by the HETG, in conjunction with ACIS in the focal plane. These observations were selected by the similar roll angles of the instrument (hence spectrometer dispersion direction) oriented for optimal study of the extended emission. The HETG consists of a pair of grating arrays, however, only those from HEG are presented here[1].

5.2 Chandra Imaging Analysis

In the process of data reduction, there exists different levels of event files (for details see section 2.4.3). Standard 'level-2' HEG events files were extracted from the archive and processed using the CIAO[2] software package (version 4.6). The total 'good-time' exposure time for the HEG was 439 ks and the average HEG/ACIS

[1]The *Chandra*/HETG Medium Energy Grating (MEG) provides no useful data above 6 keV and so are excluded from this analysis of the Fe K-shell band emission from NGC 1068

[2]http://cxc.harvard.edu/ciao/intro/

count rate was 0.0329 ± 0.0005 cts s^{-1} (over the 16-1.5 Å band.) The background was negligible in these HEG spectra. I added the positive and negative (1st) grating orders of the HEG provided by the *Chandra*/HEG/ACIS instrument configuration. I then summed the spectra to create a spectrum with a 440 ks exposure time and generated appropriate spectral calibration files via CIAO. For the imaging analysis, I summed the data based around detection of the zeroth-order centroid position for each sequence, which provided the best spatial registration of the *Chandra* images.

The first step in this analysis involved merging the event files from all the 10 observations into a single file. Before merging the event files (EVT2) from the 10 observations, the events of each file were reprojected to a common tangent point and new sky coordinates were calculated for each observation, using the original aspect solution. This task was completed using the CIAO tool "REPROJECT_EVENTS" and a new event file was created for each observation by repeating the same task. Finally, all these new events files were merged using the task "DMMERGE". From this merged file, an image can be extracted within a selected energy range using the task "DMCOPY". I extracted multiple images in different energy bands as illustrated in Figures 5.1 and 5.2. All the images were smoothed using a circular Gaussian kernel of radius 3.

5.2.1 Comparison of the images in different wavebands

The motivation for this analysis was to study the spatial dependence of different ions along the extended emission in the NLR of NGC 1068, utilizing the high-resolution images obtained by *Chandra*. In this study, I have chosen the prominent emission lines (having large observed fluxes) identified in the RGS or HETG spectra of NGC 1068. The data used in this analysis were restricted to an energy range of 0.45 - 8.0 keV, avoiding low-count or uncalibrated regimes. Two kinds of image were obtained in this analysis: one for the continua selected around the lines and the other for the emission lines. Of particular interest were the strong H-like and He-like lines: N VI, N VII, O VII, O VIII, Ne IX, Ne X, Mg XI, Mg XII, Si XIII and Si XIV, and Fe K emission lines (6–8 keV).

In Figure 5.1, I plotted the images of the continuum summed over several small bands that were free of lines. At lower energy bands (top two panels), the continuum appears to be extended, whereas at hard X-ray energies it is more intense and concentrated near the nuclear position (as clearly seen in the bottom right panel of Figure 5.1).

In Figure 5.2, I plotted the images in narrow bands dominated by emission lines and in which the continuum contribution is negligible compared to the line flux. The optical NLR emission is extended in the NE direction. The NLR gas extends in the form of a bi-cone, however only the NE cone is strong because the SW cone is directed away from our line-of-sight and consequently is obscured by the plane of the host galaxy (Ogle et al., 2003). Overall, the majority of the emission lines considered in this analysis are extended along the NE cone, except for the Fe K lines (6-8 keV, Figure 5.3) which are concentrated near the position of the nucleus (hidden in this type 2 AGN). Another noticeable difference in the images of Figure 5.2 is that Ne IX triplet lines appear to be more intense (extended red region in the top right panel of Figure 5.2) than other low-Z lines, but this is partly due to being heavily blended with the highly-ionized Fe lines (of inner-shell transitions) in the given energy range.

As noted before, there is extended X-ray emission in NGC 1068, along a position angle of $\sim 40^o$. To study the spatial dependence of the observed ionic species along this extended emission, in Figure 5.3, I showed images in three bands pertinent to the analysis of the spatial properties of the Fe K emission lines and comparison with a key soft-band line. These are the 6-8 keV band which contains the full set of Fe I–XXVI K-shell emission lines, the 6.6-7.0 keV band containing only the Fe XXV & XXVI lines, and the 0.5-0.6 keV band which is dominated by the O VII triplet. In all cases the images have been smoothed using a Gaussian function with a kernel radius of 2.5″, which provided optimum for illustration. Furthermore, to compare the counts, 1D-profile cuts (Figure 5.4) were obtained using a line projected (at 40^o) along the extended emission and centered on the images of O VII and Fe K. As can be seen from these images, and from the 1-dimensional profiles shown in Figure 5.4, the Fe K line emission is more strongly concentrated near the hard X-ray centroid peak compared comparison to the emission from the O VII lines. Specifically, I found that $\sim$70$\pm$8 % of the Fe K emission falls within a circular region of diameter 2″ (120 pc) of the X-ray centroid peak in the 6-8 keV band, confirming the B14 result. For O VII (0.5-0.6 keV), $\sim$64$\pm$11 % of the flux falls within a circular region of diameter 2" of the centroid in that bandpass (which is offset from the hard-band centroid position). The FWHM of the 1D profile for Fe K emission is $\sim 3.35''$ (200 pc), while for O VII we find a FWHM $\sim$ 3.5" (210 pc), whereas the FWHM of the *Chandra*

PSF is $\sim$ 0.5" (31 pc).

The data are inconclusive as to whether the Fe XXV Kα and Fe XXVI Kα emitting regions are spatially resolved (bottom, right panel of Figure 5.3). The spectral analysis of the Fe K lines is detailed in Chapter 6.

Table 5.1: Observations

Mission	ObsID	Roll Angle	Time	Good Time Exposure (sec)
Chandra	332	308.92°	2000-12-04 18:11:52	46290
	9148	312.12°	2008-12-05 08:23:41	80880
	9149	323.65°	2008-11-19 04:49:51	90190
	9150	315.12°	2008-11-27 04:55:36	41760
	10815	323.65°	2008-11-20 16:23:22	19380
	10816	323.65°	2008-11-18 01:18:39	16430
	10817	323.65°	2008-11-22 17:36:37	33180
	10823	315.12°	2008-11-25 18:21:16	35110
	10829	312.12°	2008-11-25 20:16:45	39070
	10830	312.12°	2008-12-03 15:08:36	43600
Suzaku	701039010	248.58°	2007-02-10 00:05:29	203000
NuSTAR	60002030002	304.23°	2012-12-18 16:01:07	115000

Table 5.2: Roll Angles and Physical Coordinates

Roll Angle	ObsID	Nucleus
309°	332	X=4081.4487, Y=4097.9761
312°	9148, 10829, 10830	X=4129.7508, Y=4105.2424
315°	9150, 10823	X=4131.2638, Y=4104.2534
324°	9149, 10815, 10816, 10817	X=4131.5000, Y=4099.0000

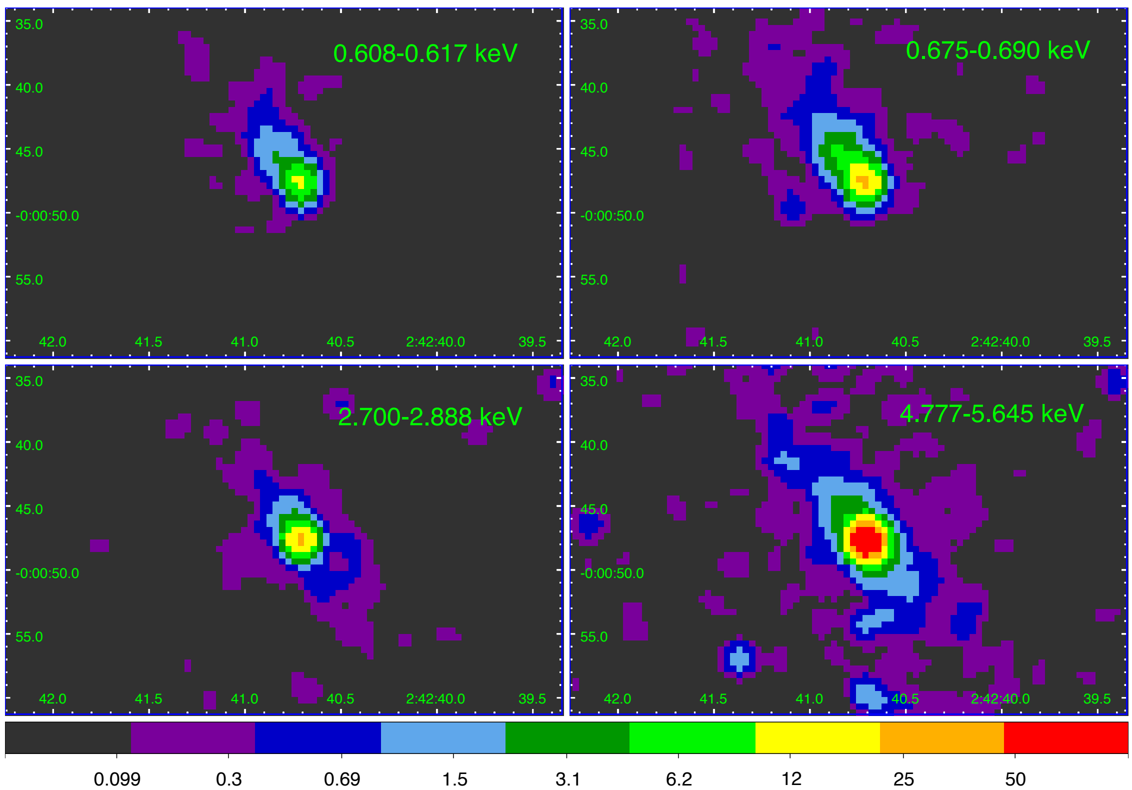

Figure 5.1: *Chandra* X-ray images of the combined 10 observations are plotted in different X-ray energy bands of the continuum selected around the emission lines. Hard X-ray energies (bottom right panel) are more intense and highly concentrated near the nucleus position, symmetrically in the NE and SW cone.

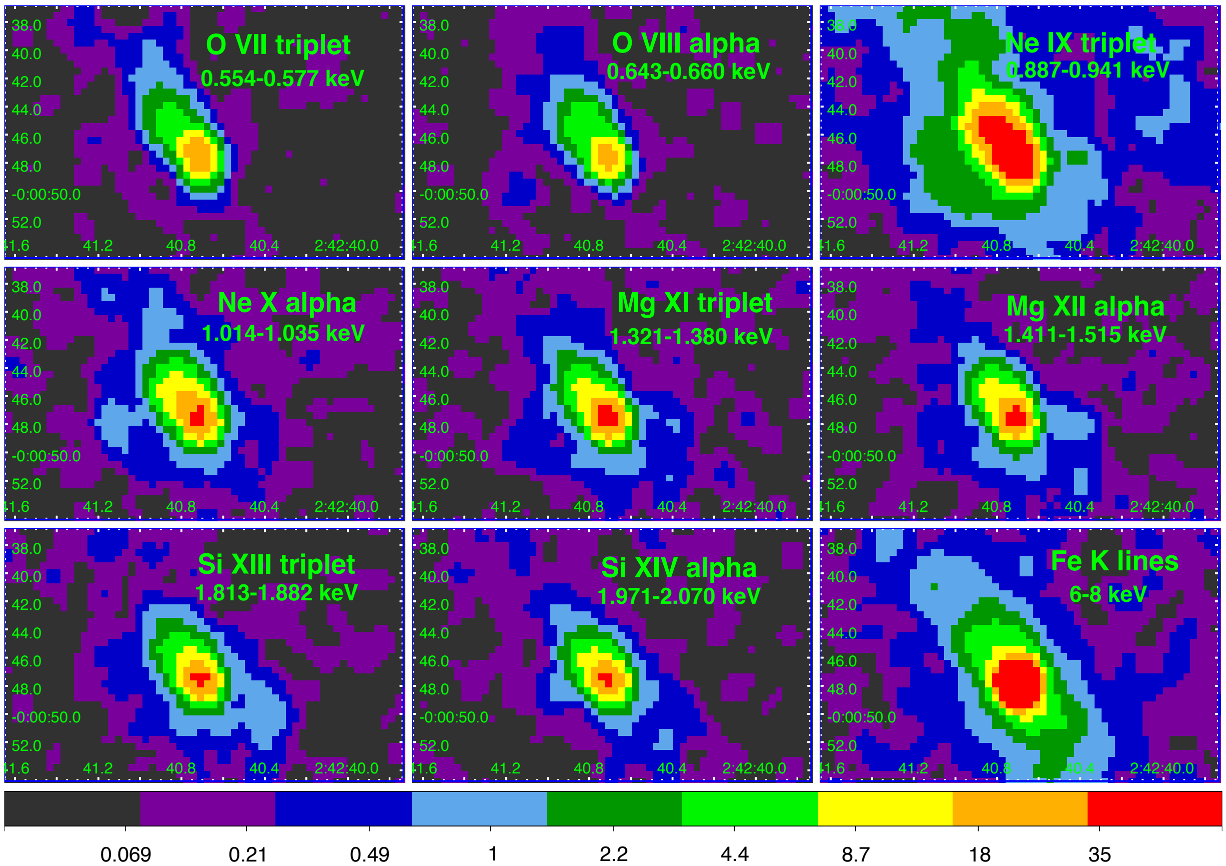

Figure 5.2: *Chandra* X-ray images of the combined 10 observations are plotted at the energy bands of the prominent emission lines as identified in the NLR of NGC 1068. North is up and East is left. The color bar represents the level of intensity of each emission line along the extended emission. Except for the Fe K lines, all other low- and high-atomic number species are extended away from the apparent nucleus position in the NE direction.

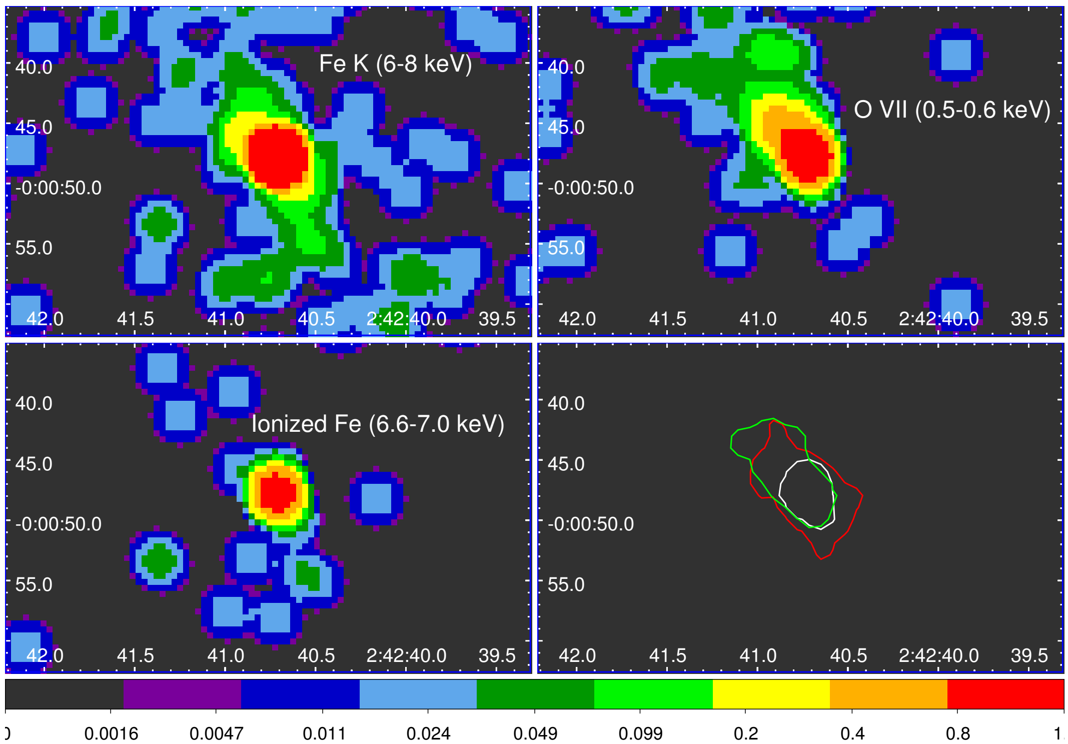

Figure 5.3: X-ray images are plotted over energy ranges dominated by the Fe K and O VII triplet line emission, illustrating the spatial dependence of these. Fe K emission is more concentrated near the hard X-ray centroid peak, in comparison to O VII as also evident from their contours overlaid on the image of their combined energy bands. Ionized Fe lines are barely resolved, as shown in the lower left panel. At the bottom right, the contours plots of Fe K emission (6-8 keV, *red*), O VII triplet (*green*) and ionized Fe (*white*) are superimposed. The coordinates right ascension (X-axis) and declination (Y-axis) are matched in each image. The color bar coding illustrates the spatial dependence of the fraction of flux compared to the peak in each band.

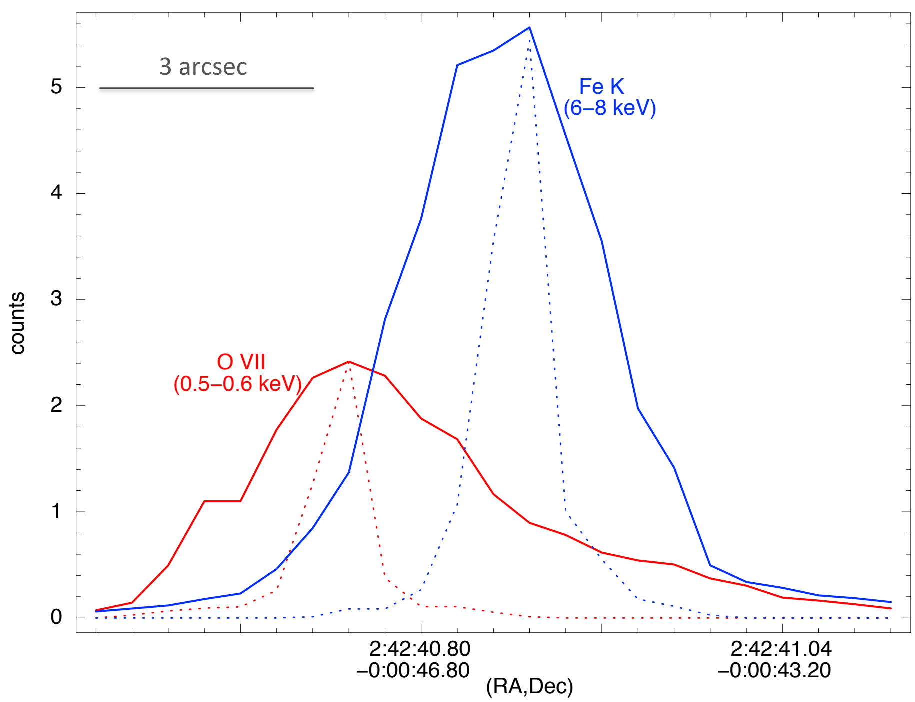

Figure 5.4: 1D profile cuts of O VII (*red*) and Fe K (*blue*) from their respective images as shown in Figure 5.3. The instrumental point spread functions at those energies (*dotted*) are also shown for comparison.

Chapter 6: Reflection and Fe Kα fluorescence

6.1 Introduction to reflection in AGN

The primary X-ray continuum is thought to be produced in a corona and is reprocessed by the circumnuclear material surrounding the black hole on scales up to $\sim$ few$\times$100 pc ($>> 10^7$ gravitational radii). Therefore, the observed spectrum is a blend of intrinsic continuum and reprocessed X-rays which are hard to separate spectroscopically in current X-ray data. Reprocessing imprints diverse atomic features on the observed spectra such as absorption edges, fluorescent emission lines (6-8 keV) and a "reflected" Compton-hump (peaking in the range 20-30 keV).

Fluorescence occurs in two stages, first an X-ray photon is absorbed (photoelectrically) leaving the K-shell vacant after removal of a 1s electron. Then this vacancy can be filled by emitting a K-shell photon (fluorescence) or by another electron (Auger process). In the simplest case, one-third of X-ray photons are absorbed in the Fe K edge ($\sim$ 7.1 keV) and re-emitted as an Fe K emission line at 6.4 keV, which explicitly implies an intimate connection between the bound-free edges and fluorescent lines. The Compton-hump is produced by the combined effects of the photoelectric absorption of low-energy photons and electron down-scattering of high-energy photons (Lightman & White, 1988).

A strong emission line due to neutral line Fe Kα (6.4 keV) was first observed in *Ginga* observations (Koyama et al. 1989 and later, *Chandra*/HETG spectra Ogle et al. 2003). Also evident in the hard X-ray spectrum are lines from the Fe XXV Kα triplet (6.6-6.7 keV) and Fe XXVI Kα (6.97 keV) that show evidence for a distinct, highly-ionized reprocessor (Iwasawa et al., 1997; Matt et al., 1997). Combining data from *ASCA*, *RXTE* and *BeppoSAX*, (Colbert et al., 2002) found the ionized and cold reflection to constitute $\sim \frac{2}{3}$ and $\sim \frac{1}{3}$ of the 2-10 keV luminosity, respectively. The ionized gas was suggested to be located < 0.2 pc from the black hole and the optically thick cold gas to reside in the inner NLR or the inner surface of the torus.

Bauer et al. 2015 (B14, hereafter) conducted a broad band X-ray study of NGC 1068 using data from *NuSTAR, Chandra, XMM-Newton* and *Swift* BAT. They found a complex of three reflectors, with column densities of 1.5×10^{23} cm^{-2}, 5×10^{24} cm^{-2} and 10^{25} cm^{-2}. The Fe lines (neutral and ionized, within 6-8 keV) and the Compton-hump were predominantly fit by the lower and higher column zones, respectively. Moreover, they found $\simeq 30\%$ of Fe Kα flux to be extended beyond 140 pc. They associated this component with their lowest column density reflector and derived a covering factor of 0.13. The ionized Fe emission, which constitutes a major part of the Fe K complex and the overall geometry, was not described in detail. Here I present a combined analysis of the data from NGC 1068 in the 2-200 keV bandpass based upon the archival data from *Chandra*, *Suzaku* and *NuSTAR* observations with the aim of constructing a full model that accounts for the neutral and ionized components of the hard-band reprocessor.

6.2 Observations and Data

6.2.1 Chandra

Chandra observations and data analysis are detailed in Chapter 5. For this analysis, along this extended emission, I defined four extraction regions for the *Chandra* HEG observations, namely Nucleus, NE1, NE2, SW1 (Figure 6.1). Each region had a width of $2.85''$ which corresponds to 171 pc for the assumed distance to NGC 1068. The extracted spectra of all the 10 observations were co-added into a single file for each region. After extracting the spectra from each region, I found the Fe K emission to be concentrated within the extraction region of the Nucleus. In this analysis, I only used the co-added spectra of the Nucleus region.

6.2.2 Suzaku

In this analysis, I used a 2007 Feb 10 observation (see Table 5.1) of NGC 1068 with a total exposure time $\sim$ 203 ks. The XIS cleaned event files for the instruments (XIS 0, 1 and 3) created by *Suzaku* pipeline processing were further reduced using the HEAsoft (v6.12) software. The total exposure time for the summed XIS data was 125 ks and for both the PIN and GSO it was 39 ks. The source and background spectrum were extracted assuming a circular region of radius $\sim 170''$. The background spectrum was extracted from a source-free region. The required XIS spectral files were extracted using XSELECT and then added using the ADDASCASPEC task, along with their background files and response matrices. Similarly, PIN and GSO spectral, background and response files were generated following the standard data reduction techniques[1]. The total source count rates were 93.6±0.7 %, 11.1±1.6 %, 0.20±0.02 % for the XIS013, PIN, and GSO instruments respectively.

6.2.3 NuSTAR

I used the archived data from 2012 Dec 18 observation (see Table 5.1) of NGC 1068 with a total time exposure of $\sim$ 60 ks. Taking the level 2 calibrated and screened event files we ran the task NuPRODUCTS within the NuSTARDAS software (v1.4.1) package to obtain the required source spectrum with its corresponding calibration files for each FPMA and FPMB module. The total summed exposure time for FPMA+FPMB was 115 ks. The source and background spectra were extracted using a circular region of radius 80″. The background data were extracted from a region far away from the source but on the same detector. In this analysis, we used spectra data covering 3–55 keV. The upper limit for useful data was set by systematic uncertainties found during on-orbit calibration. The source comprised of 87 % (FPMA) & 86 % (FPMB) of the total rate for the *NuSTAR* instruments.

6.3 Spectral Fitting

I fit the combined spectra from *Chandra* (HEG), *Suzaku* (XIS013, PIN & GSO) and *NuSTAR* (FPMA+FPMB) spanning an energy range 2-200 keV using the XSPEC analysis package (Arnaud, 2010), The HEG and XIS013 spectral data

[1]http://heasarc.gsfc.nasa.gov/docs/suzaku/analysis/abc/

were binned at HWHM (half width at half maximum of the spectral resolution for each instrument). All binned spectral data contained more than 20 counts per channel, allowing use of the χ^2 statistic for spectral fitting.

6.3.1 Deconvolving the Neutral and Ionized Fe lines

As noted above, the 6-8 keV band contains a multitude of potential emission lines of iron spanning Fe I-XXVI. The HEG has the spectral resolution (FWHM$\sim$1800 km s^{-1} at 6 keV) to be able to resolve some of these lines. To that end I performed an analysis of the HEG data in two steps. First, I fit two Gaussian profiles fixed at the rest energies of Fe Kα and Kβ for neutral gas. The normalization of Fe Kβ was fixed at 10% of Fe Kα (Palmeri et al., 2003) and their line widths were tied. We added three more Gaussians for the ionized Fe XXV *r, f* and Fe XXVI Kα lines. The region 6.42-6.8 keV contains a broad blend of lines likely from inner-shell transitions (e.g. Fe II-XVII, Figures 6.2–6.5), centered close to the Fe XXV Kα triplet (Kallman et al., 2004). Owing to blending of several components close to the Fe XXV Kα lines, I was unable to get constraints on the line widths and velocity shifts in that region. However, I was able to deconvolve the 6.97 keV Fe XXVI Kα line component from 7.05 keV Fe Kβ. Therefore, for the ionized gas, I based our line width and velocity shift measurements on the Fe XXVI alone.

6.3.2 Velocity Constraints

There were no significant velocity shifts relative to the systemic velocity for Fe Kα, Fe XXV r and Fe XXVI Kα. The bulk velocity shift (σ) for the neutral Fe Kα, Kβ emitter was constrained to the range 0-170 km s^{-1}, where a positive velocity would correspond to inflow. The limit for the ionized gas traced by Fe XXVI was $\pm$660 km s^{-1}. The line widths and fluxes are provided in Table 6.1; the errors were calculated within 68% confidence level. For verification, I fit the combined spectra of HEG and XIS (Figure 6.4) confirming consistency with the best-fit parameters obtained in the analysis of the HEG data alone.

6.3.3 Model Fitting

I tested various combinations of models to account for the important features in the spectrum, i.e. the shape of the underlying continuum, Fe K emission lines (6-8 keV) and the Compton-hump. My analysis procedure is similar to that described in B14, hence I discussed only the critical steps. As consistent with the values used in previous analysis (Chapter 4), all the models in this analysis assumed a Galactic column=5.43×10^{20} cm^{-2} (Kraemer et al., 2015), an X-ray continuum having photon index Γ=2, a host galaxy redshift=0.003793 equivalent to 1137$\pm$3 km s^{-1} (Huchra et al., 1999) and solar atomic abundances (Anders & Grevesse, 1989). I achieved my primary goal, deriving constraints on the neutral and ionized reprocessors, from our measurements of the neutral Fe Kα and the Fe XXVI lines.

6.3.3.1 The Neutral Component

I used the Compton-thick neutral X-ray reflection model "MYTorus" (Yaqoob, 2012) which provides individual table models for the transmitted continuum, Compton-scattered continuum and the fluorescent emission lines. In its default (coupled) mode, the column densities, inclination angles and normalizations of the transmitted and scattered components are tied such that the reprocessing represents that from a solid toroidal geometry. In the decoupled mode I can derive different line(s)-of-sight and global average column densities for the two components (Murphy & Yaqoob, 2009). No coupled model fit the data satisfactorily. However, the spectra were well-constrained in the decoupled mode using three Compton-scattered components and our model in the XSPEC was structured as follows:

$$
\begin{aligned}
\text{model} \;=\;& \text{constant} < 1 > *\text{tbabs} < 2 > (\text{powerlaw} < 3 > \\
& +\text{atable}\{\text{MYTorus\_transmitted\_component}\} < 4 > \\
& +\text{atable}\{\text{MYTorus\_scattered\_component}\} < 5 > +\text{pexriv} < 6 > \\
& +\text{gsmooth} < 7 > *\text{atable}\{\text{MYTorus\_scattered\_linetable}\} < 8 > \\
& +\text{zgauss} < 9 > +\text{zgauss} < 10 > +\text{zgauss} < 11 > +\text{zgauss} < 12 > \\
& +\text{zgauss} < 13 >)
\end{aligned}
$$

where $< 1 >$ is the PIN to XIS cross calibration constant, $C_{\mathrm{PIN:XIS}}$, $< 2 >$ is the Galactic column density, the other constants ($< 4 > = < 6 > = < 8 > = 1$) are scalars for the MYTorus table models. $< 10 >$ provides the Gaussian smoothing parameters of the Gaussian width at 6 keV and the index for width variation with energy, applied to the MYTorus line table. The five Gaussians ($< 12 > - < 16 >$) were fit to the lines from Si XIV, S XV, S XVI, Fe XXV Kα and Fe XXVI Kα at 2.3 keV, 2.45 keV, 2.63 keV, 6.70 keV and 6.97 keV respectively. $< 9 >$ represents the ionized reflection model PEXRIV (Magdziarz & Zdziarski, 1997). PEXRIV represents reflection assuming a slab geometry, and uses the ionization parameter ξ.

The inclination angles of the three scattered components were fixed at 0^{o}, 0^{o} and 90^{o} respectively and characterized by column-densities (N_H): $\sim$1.5$\times$10^{23} cm^{-2}, $\sim$5$\times$10^{24} cm^{-2} and $\sim$10^{25} cm^{-2} (as in B14). These low, medium and high column scatterers provided reasonable fits to the Fe K region, extended emission and the Compton-hump.

6.3.3.2 The Ionized Component

As noted, the complex region of Fe K contains both neutral and ionized emission lines, predominantly Fe Kα, Kβ and Fe XXV, XXVI respectively. Since the MYTorus model represents the neutral gas, the ionized Fe XXV and XXVI must be modeled separately. To model the ionized reflector I used the ionized reflection model PEXRIV (Magdziarz & Zdziarski, 1997) together with XSTAR (Kallman et al., 2004). To constrain ξ and N_H for the ionized Fe lines only, I generated an additive ATABLE using XSTAR for use in XSPEC. I assumed a range of $\mathrm{N_H}$:10^{18-24} cm^{-2} and log(ξ):1-3.7. I found the observed ratio of Fe XXV Kα and Fe XXVI Kα to be consistent with N_H =1.5$\times$10^{23} $^{+2\times10^{23}}_{-9\times10^{22}}$ cm^{-2} and log(ξ)=$3^{+0.12}_{-0.06}$, assuming that both lines are being emitted in the same component. While such a solution fitted the lines, the ATABLE component underpredicted the observed scattered continuum because XSTAR does not do a full treatment of Compton scattering. To correct for this, I assumed that the scattered continuum scales simply with the column density and added an appropriate amount of PEXRIV to complete the model for the ionized reflector by scaling the normalization of that component to the ionized lines.

6.4 Discussion

In Chapter 5, I performed a spatially-resolved HEG imaging analysis of the extended NLR emission finding Fe K-shell emission (6-8 keV) to be concentrated within ~ 170 pc of the nucleus. My spectral model for the Fe K emission (Figure 6.5) is composed of one ionized and two neutral Compton-scattered components.

6.4.1 Ionization structure of the reprocessing gas

Multiple components contribute to the reprocessing of the X-ray continuum. My fit required two low-column Compton-scattered components (assumed to be oriented face-on) and these represent the reflected light from the 'far side' of the toroidal bowl. My neutral gas component, inclined perpendicular to our line-of-sight, blocks a direct view of the continuum and reflection. Setting up the model in this way, I mimic a geometry for the neutral gas that is consistent with a clumpy torus. My model geometry is depicted in Figure 6.6, where the neutral and ionized gas clumps form a bowl-shaped structure, building on the previous suggestion by

Konigl & Kartje (1994). When observed through an unobscured line-of-sight, the reflection from the inner surface of the far-side obscuring material produces the observed Fe K lines, along with the extended emission.

A similar geometric picture was suggested by Colbert et al. 2002 (see their Figures 8 & 9) who proposed a sight-line to an ionized reflector that skimmed through the edge of the torus while the continuum was blocked from direct view by that torus. My picture is a little more complex, with continuum, neutral and ionized reflection all being viewed through clumpy toroidal gas (Figure 6.6). I note that the bowl shape of our model is not a unique solution for these data, other geometries such as a funnel, may provide good fits to the data.

The presence of Fe XXV Kα and Fe XXVI Kα means that the iron must be in gas phase (not in grains), therefore, I compared the dust sublimation radius ($r_{\rm sub}$) with my derived distances. I estimated the radial distances of the neutral and ionized reflectors to be $\sim 0.032^{+0.015}_{-0.010}$ pc and $0.016^{+0.084}_{-0.010}$ pc, assuming the line broadening arises from Keplerian motions. The dust sublimation radius was estimated assuming the following (from Barvainis, 1987; Hönig & Beckert, 2007)

$$r_{sub} = 0.4\text{pc} \times L_{45}^{1/2} T_{sub;1500K}^{-2.8} a_{0.05}^{-1/2} \tag{6.1}$$

where I used $L = 10^{44.2}$ ergs s^{-1} (see Chapter 4), $T_{sub} = 1500$ K (sublimation temperature, Jaffe et al. 2004), $a = 0.05\mu$m (size of the dust particle, Mathis et al. 1977). I found $r_{sub} > 0.16$ pc, a factor of ten larger than the radius of the ionized reflector and a factor of five larger than the radius of the neutral reflector. The size

Table 6.1: Fitted parameters for Fe K line emission

Line ID	Energy (keV)	Line Width (σ) (km s^{-1})	Flux ($\times 10^{-5}$ photons cm^{-2} s^{-1})
Fe I Kα	6.40	1500$\pm$300	4.57$\pm$0.41
Fe XXV Kα	6.7	4500$\pm$1500	$\leq$4.01$\pm$0.43
Fe XXVI Kα	6.97	2000$\pm$1200	1.04$\pm$0.28

Table 6.2: Reprocessor Model Components

Model[a]	Component	N_H (cm^{-2})	i[b]	norm[c]
MYTorus	transmitted (neutral)	10^{25} (fixed)	90 (fixed)	7.17$\pm$1.026 $\times 10^{-2}$
MYTorus	scattered (neutral)	$5^{+4}_{-3}\times 10^{24}$	0 (fixed)	6.83$\pm$0.750 $\times 10^{-3}$
PEXRIV	reflected (ionized)	6×10^{23} (fixed)	0 (fixed)	1.56$\pm$0.021 $\times 10^{-4}$

[a]Galactic column was fixed at 5.43×10^{20} cm^{-2}. The photon index was fixed at 2.0. The ionization parameter in this PEXRIV model was fixed at 1000. The overall fit produced reduced $\chi^2 = 1.16$ for $dof = 3181$

[b]Inclination angle in degrees

[c]in units of photons keV^{-1}cm^{-2}s^{-1}

estimates for the Fe K emission were much larger in the work of B14, because those authors included some of the extended Fe K emission in their estimate. Here I am constraining the size of the dominant and relatively compact Fe K line-emitting gas.

Assuming $L_{ion}=10^{44.2}$ ergs s^{-1} (Kraemer et al., 2015) and log(ξ)=3, the hydrogen density n is $\sim 6.5\times 10^7\ ^{+4.0\times 10^8}_{-6.3\times 10^7}$ cm^{-3}. This is consistent with the density of the warm reflector ($< 10^{5.5}$ cm^{-3}) found in Colbert et al. (2002).

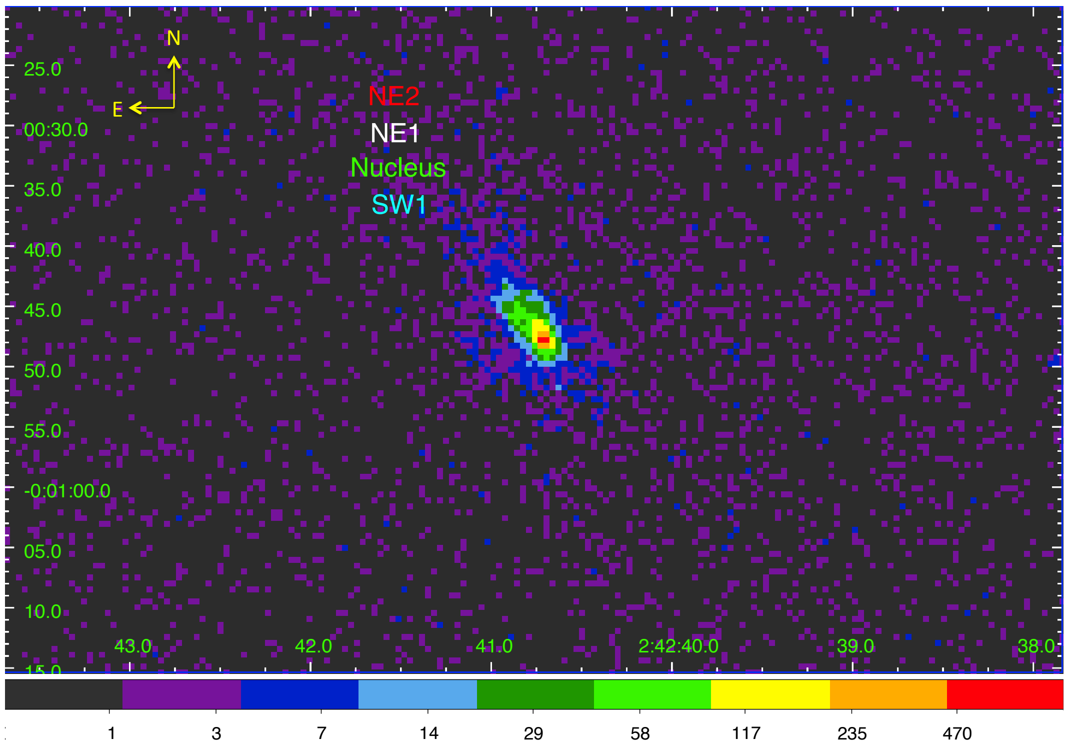

Figure 6.1: Zeroth-order image from the coadded *Chandra* HEG observations listed in Table 1 color coded by the total number of counts per pixel with the extraction regions (each 2.85″ wide) used here superimposed. The abscissa is plotted as Right Ascension and the ordinate as Declination.

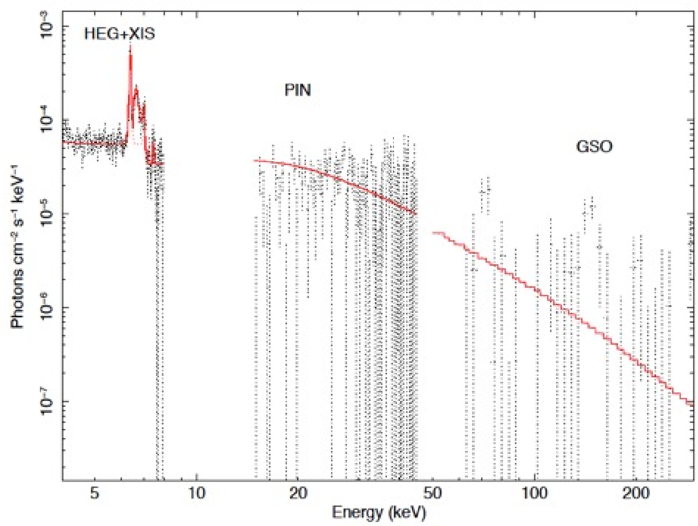

Figure 6.2: As a preliminary test, the combined spectra from HEG, XIS, PIN and GSO are fit with the reflection model PEXMON. The inclination angle and the energy cut-off used in this fit were 80° and 500 keV. The reduced χ^2 was 1.35.

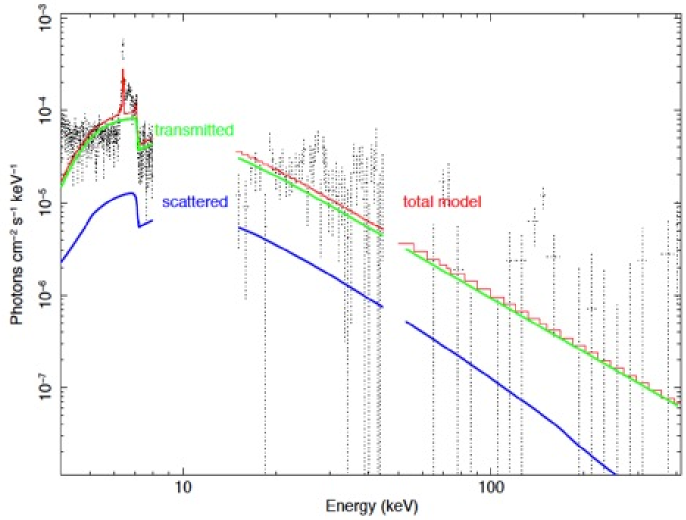

Figure 6.3: The same data as shown in Figure 6.2 are modeled with neutral Compton-scattered components of MYTorus model, in its coupled mode (see text for details). The reduced χ^2 was 4.6.

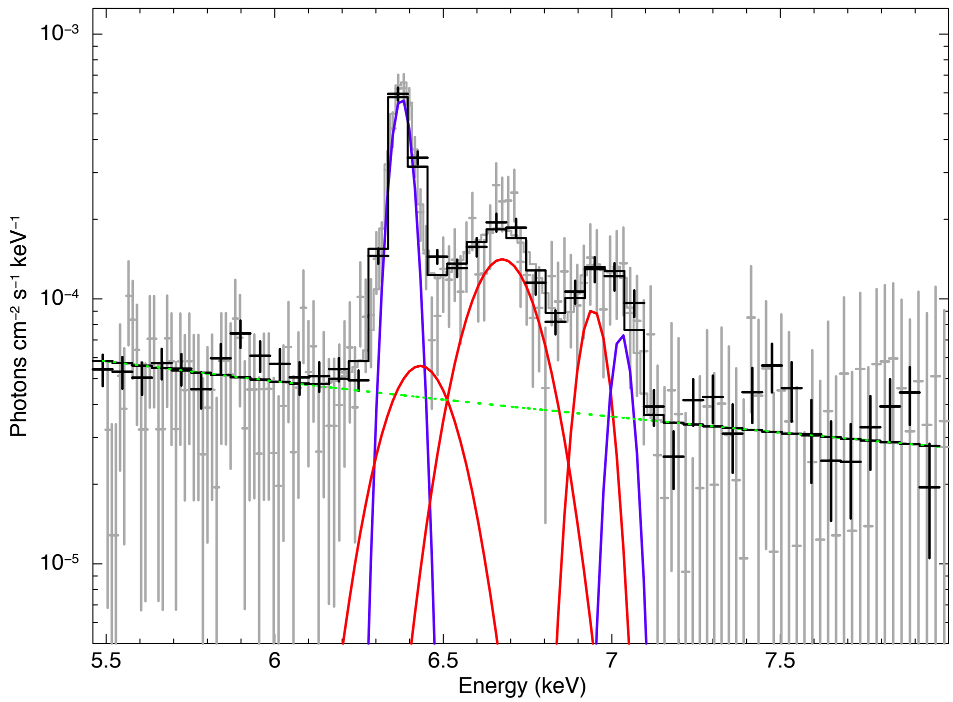

Figure 6.4: Gaussian fits to the neutral (*blue*) and ionized (*red*) Fe lines, as shown in the overlapped spectra obtained from HEG (*grey*) and XIS (*black*). The abscissa is plotted as rest energy. The dotted line shows the power law fit to the underlying continuum at Γ=2. The best-fit parameters are quoted in Table 6.1. See text for details.

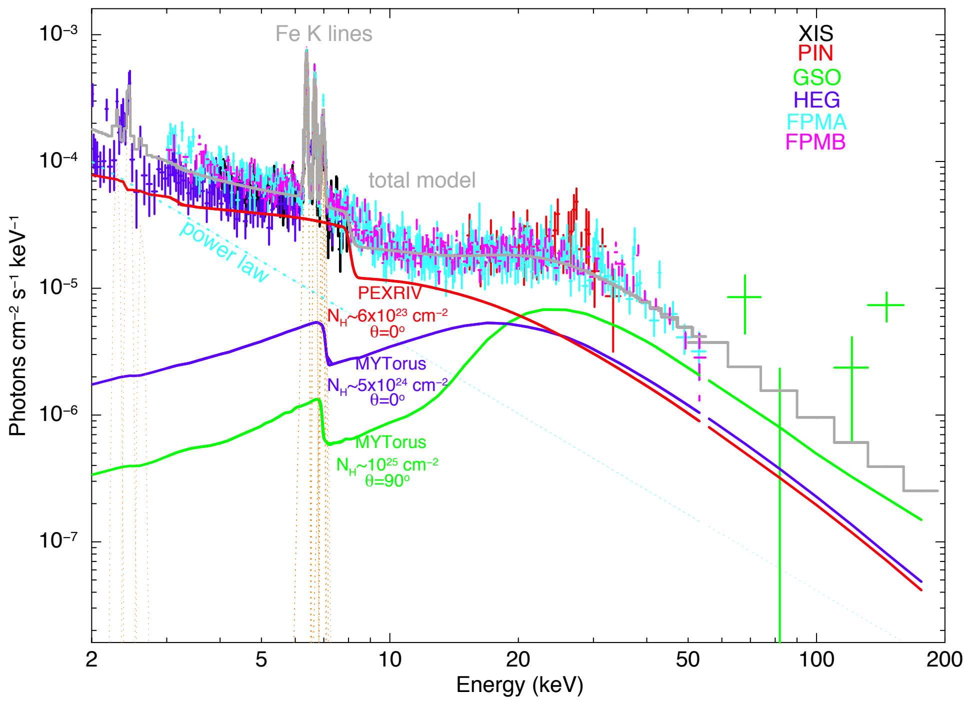

Figure 6.5: The final model (*grey*), a composite of one ionized reflection model PEXRIV (*red*) and two neutral Compton-scattered components MYTorus (*blue, green*), fits fairly well to the combined spectra of HEG, XIS, PIN, GSO, FPMA and FPMB. The abscissa is plotted as rest energy. All of the emission lines in *dotted grey* are modeled with Gaussian profiles fixed at their rest energies, except for the neutral Fe lines (Kα, Kβ) which are modeled using MYTorus line table.

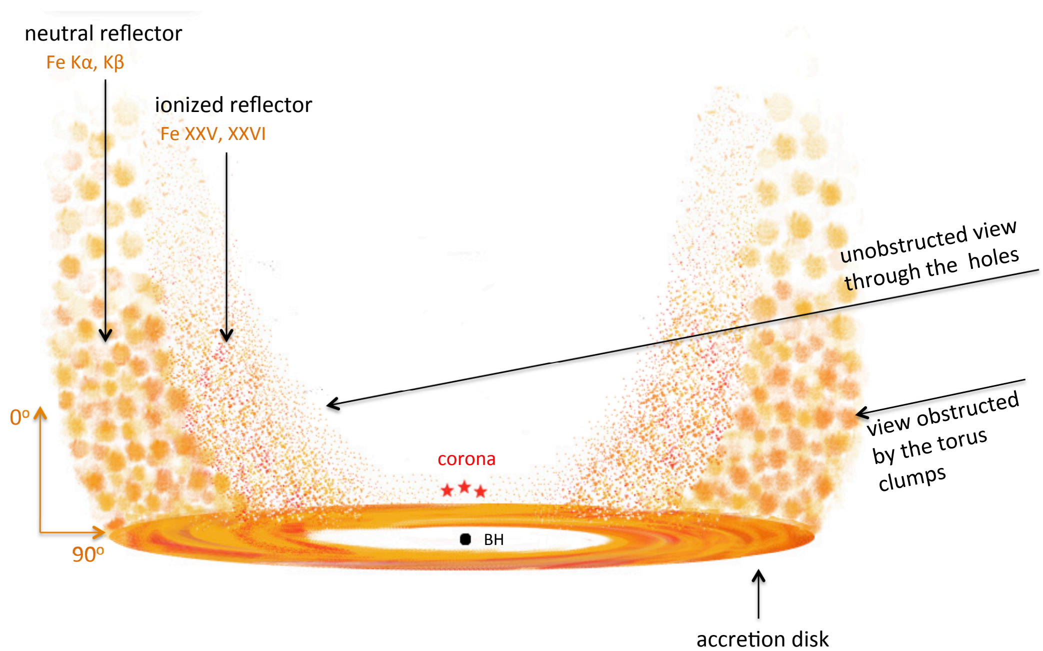

Figure 6.6: Schematics of the neutral and ionized reflectors extending outwards in a clumpy and bowl-shaped structure. The unobstructed line-of-sight (through a hole) reveals the Fe K line emission from the illuminated far-side reflection off the obscuring gas (at face-on viewing angle). The broad Compton-hump is produced when the line-of-sight intercepts the optically thick gas clumps (at edge-on viewing angle). The degree of ionization decreases as moving away from the central engine in a direction parallel or perpendicular to the accretion disk.

Chapter 7: Conclusions and new perspectives

7.1 Overview

In this thesis, I constrained the physical conditions in the X-ray emission-line gas in the NLR in NGC 1068. I used the soft, medium and hard X-ray data from the *XMM*, *Chandra*, *Suzaku* and *NuSTAR* observatories and divided the analysis in two parts.

First, I constrained the physical parameters (e.g. column density, ionization parameter, hydrogen density, covering factor, mass loss rate, etc.) in the extended NLR gas (> 30 pc away from the central engine), and based this analysis on the strong H-like and He-like emission lines observed in the soft X-ray spectrum of NGC 1068. In the second part of my research, I concentrated on the origin of the neutral and ionized Fe K lines within 6–8 keV, which represent the cold and hot reflectors, respectively, in NGC 1068. The measured distances of the reflectors place them much closer (< 1 pc) to the continuum source.

7.2 Recap of the XNLR results obtained using RGS/*XMM-Newton*

I analyzed an archival XMM-Newton/RGS spectrum of the Seyfert 2 galaxy NGC 1068, which was previously published by Kinkhabwala et al. (2002). In the process, I first remeasured the emission-line fluxes, widths and radial velocities, and the fluxes and widths of RRCs, and, overall, obtained similar values to those of Kinkhabwala et al. (2002). I generated photoionization models, using CLOUDY (Ferland et al., 2013), and fit the emission-line spectrum with two components characterized by two different sets of physical parameters.

My main results are as follows.

1. Overall the X-ray emission-lines have radial velocities blue-shifted with respect to the systemic velocity of the host galaxy. The outflow velocities of the two zones LOWION and HIGHION are 215 km s^{-1} and 166 km s^{-1}, respectively. The velocities and FWHM are consistent with that of O [III] 5007, which suggests that the X-ray gas is part of the mass outflow through the NLR.

2. Based on my preliminary modeling results, I determined the abundances of heavy elements in the emission-line gas to be overall 1.5 $\times$ solar. However, the carbon and nitrogen abundances are 3.2 and 6 times solar, respectively. One possibility is that an early period of star-formation produced much of the excess carbon, which was followed by conversion of carbon into nitrogen in a more recent period. Kallman et al. (2014) also suggested non-standard abundances for the emission-line gas, but did not discuss possible connections with the star-formation history for NGC 1068.

3. I was able to fit most of the strong emission lines with two components,

LOWION and HIGHION, characterized by logU = -0.05 and 1.22, and logN_H = 20.85 and 21.2, respectively. The LOWION produces most of the emission from He-like C, N, and O lines, while the HIGHION produces the H-like N, O, and Ne and most of the He-like Ne lines. The predicted electron temperature for LOWION is consistent with the measured widths of He-like RRCs, however the electron temperature of HIGHION is several times higher than that derived from the H-like RRCs, which I attribute to uncertainties in the width measurements. Overall, the emission lines and RRCs are consistent with photoionization, albeit with a small contribution from photoexcitation for the resonance lines.

4. The covering factors determined for LOWION and HIGHION were 0.35 and 0.84, which, while physically possible (< 1, the total solid angle), are high given the likelihood that a fraction of the X-ray emission is undetected due to absorption by material in the disk of the host galaxy or surrounding the NLR. However, assuming that there exist multiple zones (more gas emission) of highly ionized gas, which cannot be distinguished here, the covering factors can be reduced.

5. I estimated the total mass and mass outflow rates for LOWION to be 8.7×10^4 $M_\odot$ and 0.38 $M_\odot$ yr^{-1}, for HIGHION these values are 4.7×10^5 $M_\odot$ and 0.06 $M_\odot$ yr^{-1}. Interestingly, the X-ray emission line gas likely represents the component having the largest mass in the NLR, in contrast to other components discussed in e.g. Armentrout et al. (2007), for the Seyfert 1 galaxy NGC 4151.

6. The ionization state and temperature of HIGHION are consistent with those of the scattering medium in which the polarized optical emission arises (Miller et al. 1991; Kraemer & Crenshaw 2000), although its column density is an order of

magnitude too small. However, if there is more X-ray emitting gas present with higher N_H, as noted in item 4., the total column density of high-ionization gas could be sufficient to produce the scattered light. The radial profile of the continuum radiation (Crenshaw & Kraemer, 2000) is consistent with such a scenario. Therefore, I suggest that the scattered emission arises in the X-ray emission-line gas, in agreement with Ogle et al. (2003).

7.3 Location and geometry of the neutral and ionized reflectors in the circumnuclear regions of NGC 1068

I analyzed the combined spectra of the Seyfert 2 galaxy NGC 1068 obtained by *Chandra* (HEG), *Suzaku* (XIS013+PIN+GSO) and *NuSTAR* (FPMA+FPMB). In this study, I concentrated on the origin of the neutral and ionized Fe K lines.

From imaging analysis and spatially-resolved spectroscopy using *Chandra* data, I confirmed the B14 result, that $\sim 70\%$ of the Fe K line emission is concentrated within 120 pc of the X-ray centroid position.

I modeled the combined X-ray spectral data with one ionized (warm) and two neutral (cold) Compton-scattered components having column densities of $\sim 6\times10^{23}$ cm^{-2}, 5×10^{24} cm^{-2} and 10^{25} cm^{-2}, respectively. The Compton-hump (above 10 keV) is predominantly produced in the high column reflector whereas the Fe K emission arises in the low column components. The ionized (Fe XXV, XXVI) lines are produced in highly ionized gas ($\log\,\xi = 3$) with a high column density ($> 10^{23}$ cm^{-2}). The data are consistent with reflection of the primary X-ray continuum from the inner far-side of a clumpy torus, where the neutral and ionized reflectors are located at distances of $\sim 0.032^{+0.015}_{-0.010}$ pc and $0.016^{+0.084}_{-0.010}$ pc, respectively, from the central source. This clumpiness of the obscuring material has recently been confirmed by Marinucci et al. (2016). In my model, the ionized gas resides on the illuminated face of the torus shielding the neutral gas.

Finally, putting together the results of these two analyses in one "big picture", with the corresponding physical parameters and distances of all the gas components, I summarize these results in Figure 7.1. The nuclear continuum is reprocessed in the warm plasma lying close to the central engine (< 30 pc) and the soft X-ray emission is produced in the NLR (spanning 100s of parsecs) through photoionization/recombination processes. This warm gas is found to be consistent with the warm absorbing medium, which is viewed as the warm absorber in the line-of-sight in Seyfert 1 galaxies (Kinkhabwala et al., 2002). In Seyfert 2 NGC 1068, the inner portion of the ionization cone ("warm absorbers") is viewed through the holes in the torus.

7.4 Future Work

The studies presented in this thesis have opened several research lines to be explored in the future. For instance, in the RGS spectrum of the NLR, the emission lines of the heavy atomic number species e.g. Ne, Mg, S and Si are not fully resolved, which limits the diagnostics of the very highly ionized gas. However, these lines are well resolved in the HEG spectra, which further indicates the presence of the third gas component with very high ionization parameter and column density. The implications of the RGS models to these heavy-Z emission lines can provide tight constraints on the elemental abundances. Furthermore, with the current instrumentation, the Fe K emission lines within 6–8 keV, especially Fe XXV triplet, and the primary continuum are difficult to resolve.

The X-ray Calorimeter Spectrometer onboard *Hitomi* provides a high energy resolution of 4.2 eV (FWHM) at 6 keV. Above 2 keV, the spectral resolution of the Soft X-ray Spectrometer is an order of magnitude higher than the HETG aboard the *Chandra* observatory, hence providing better constraints, than any previous mission, on the Fe K emission lines, the compton-hump and the hard X-ray tail of the spectrum. *Hitomi* would provide the simultaneous detection of the different absorption components in the range of soft X-rays to hard X-rays (E$\sim$0.5–10 keV).

In Figure 7.2, I simulated an SXS observation of NGC 1068 in the waveband of $\sim$ 3–15 Å (4–0.8 keV) using a 200 ks exposure time based upon my best RGS model. Comparing with the RGS data, the clearly resolved highly ionized emission lines of heavy-Z species would enable us to obtain tight constraints on the physical parameters of very highly ionized X-ray gas which gives rise to the scattering emission. For instance, in the simulated spectrum (of 200 ks SXS exposure) in the range of 6–8 keV (Figure 7.3) the double-peaked structure of the neutral Fe Kα emission line is well resolved. Moreover, Fe Kβ, which was blended with Fe XXVI in the *Chandra* observation, can be clearly seen in Figure 7.3. The Fe K line energy will be resolved to $\sim \pm 20\%$, as determined by fitting the simulation. Deconvolving the Fe K complex lines in the range of 6–8 keV is very important to determine the ionization structure of the torus in detail.

In the RGS data, the heavy-Z lines of Mg XII α and Si XIV α were not very well-resolved and hence were not constrained having large uncertainties (1σ) on their velocity shifts, e.g. the measured velocity shift of Mg XII α was -277^{+388}_{-619} km s^{-1}. In contrast, from the *Hitomi* simulated spectrum (Figure 7.2), I fit the simulated SXS observations of the emission lines of Mg XII α and Si XIV α with Gaussians and obtained their corresponding velocity shifts, reducing the uncertainties to $+58\pm54$ km s^{-1} and -84^{+97}_{-28} km s^{-1}, respectively. These relatively redshifted highly ionized lines indicate the presence of a third zone, lying close to central engine, which may also be linked to the warm absorbing X-ray gas zones known as the ultra fast outflows (UFOs, e.g. Tombesi et al. 2010).

My work on NGC 1068 revealed the overall properties of NGC 1068, including a high mass accretion rate, super-solar abundances, large amounts of highly ionized gas and molecular gas (e.g. Riffel et al. 2014), and active star-formation (Bruhweiler et al., 2001) may be connected to its stage of activity. That is, NGC 1068 is in an early part of its active phase, at which time the AGN is being rapidly fueled but before the inner nucleus has been cleared. Detailed study of nearby sources such as NGC 1068 is important, as it allows us to build a model that is likely generally applicable to AGN.

Future work using satellites such as *Hitomi*, will allow refinement of the conditions and locations of the circumnuclear gas.

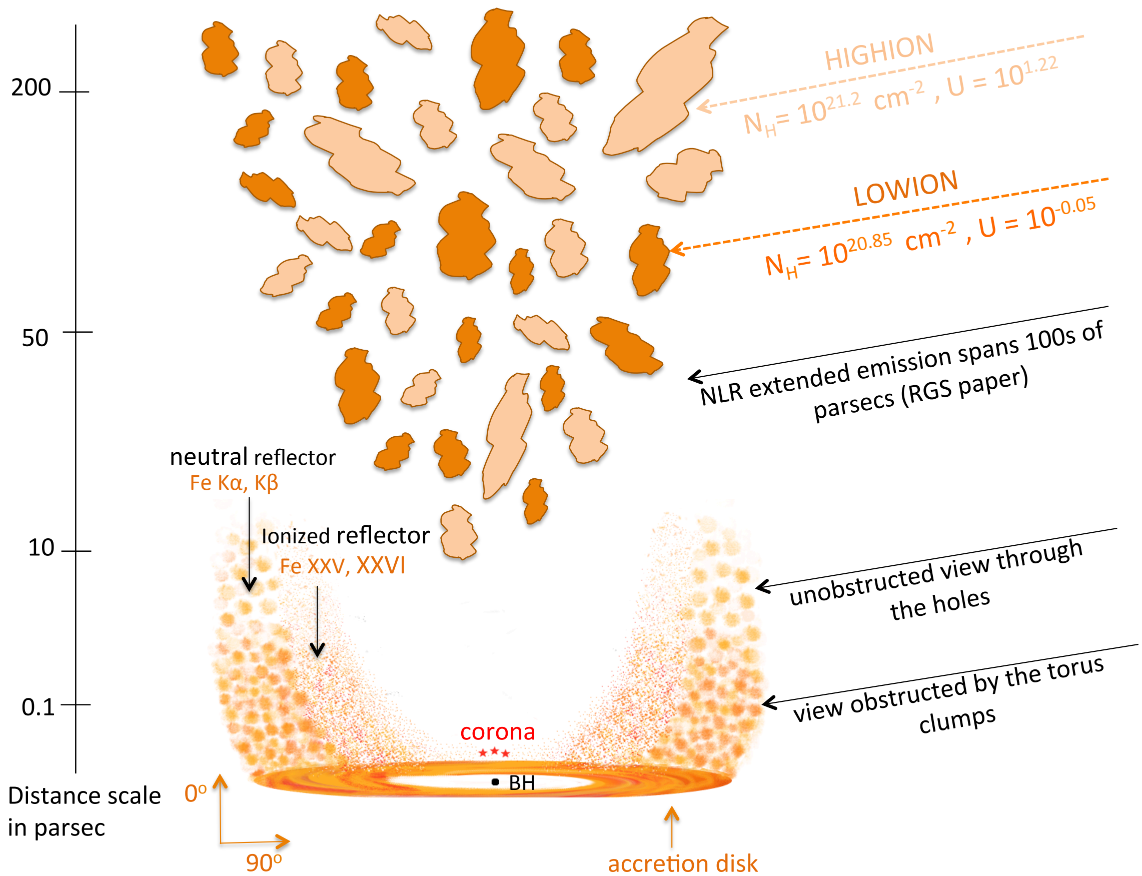

Figure 7.1: A schematic representation of the apparent morphology of the circumnuclear regions in the NLR of the Seyfert 2 galaxy NGC 1068. The NLR extended emission lies at distances of hundreds of parsecs, dominated by two gas components represented as LOWION and HIGHION with their respective physical parameters. The Fe K lines and the primary continuum are being emitted at sub-parsec scales, very close to the central continuum source, and ultimately are reflected in the NLR, as illustrated in this figure by the neutral and ionized reflectors. The reflection occurs at the inner far-side of a clumpy torus.

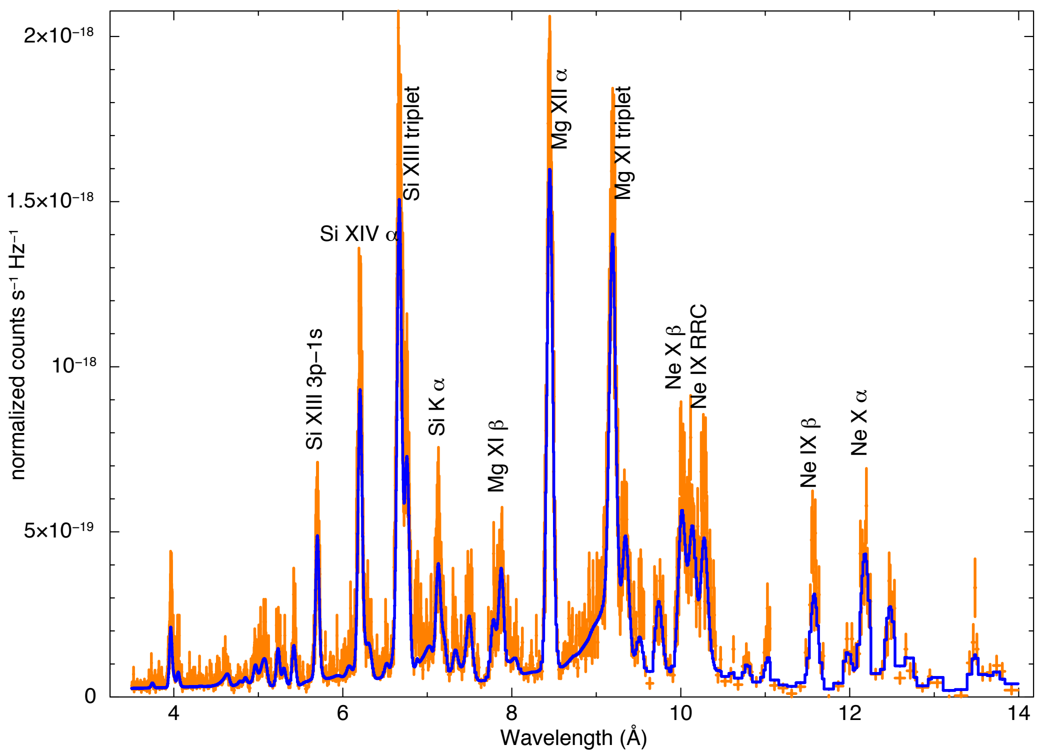

Figure 7.2: The NGC 1068 observation (*orange*) simulated with the SXS instrument aboard upcoming X-ray observatory *Astro-H*, for a 200 ks exposure time and is fit with our best RGS model (*blue*).

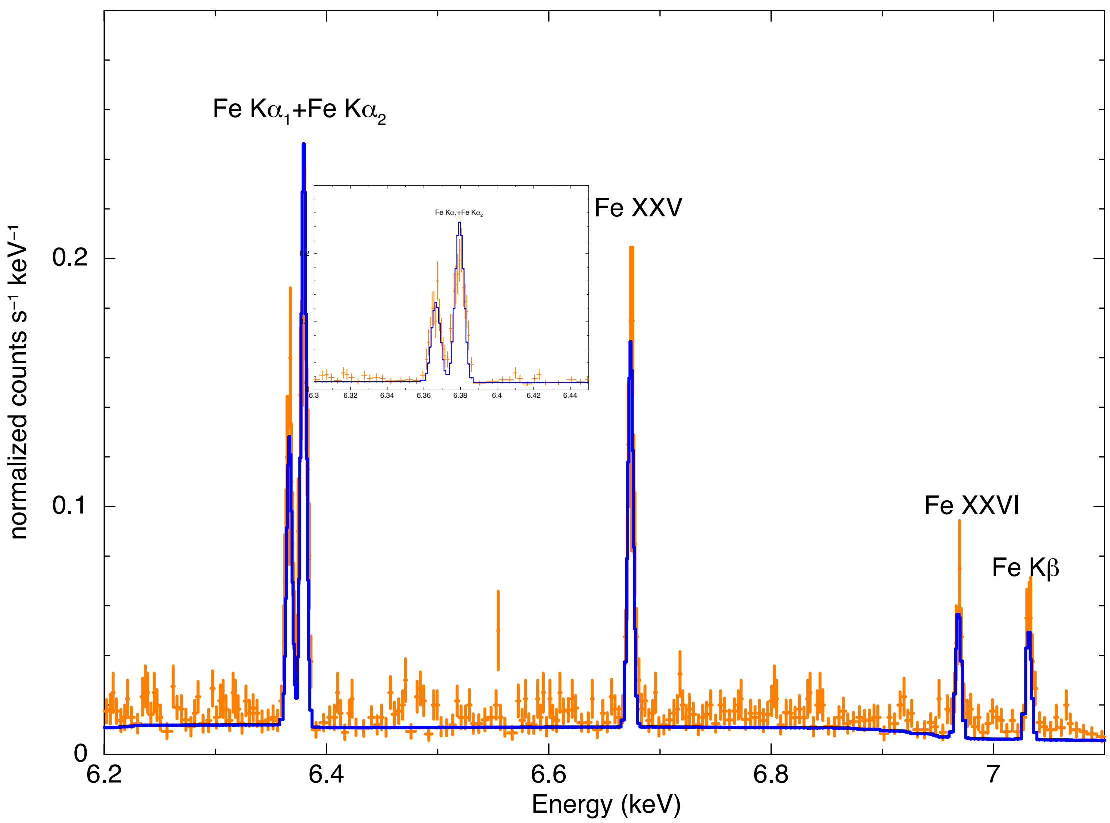

Figure 7.3: The NGC 1068 observation (*orange*) simulated with the SXS instrument aboard upcoming X-ray observatory *Astro-H*, for a 200 ks exposure time and is fit with our best model (*blue*). The double-peaked structure of the neutral Fe Kα is clearly resolved, as shown in the insert.

Bibliography

Alloin, D. 2006, Physics of Active Galactic Nuclei at all Scales, 693,

Anders, E., & Grevesse, N. 1989, GCA, 53, 197

Antonucci, R. R. J. 1983, BAAS, 15, 976

Antonucci, R. R. J., & Miller, J. S. 1985, ApJ, 297, 621

Antonucci, R. 1993, ARAA, 31, 473

Armentrout, B. K., Kraemer, S. B., & Turner, T. J. 2007, ApJ, 665, 237

Arnaud, K. A. 2010, Bulletin of the American Astronomical Society, 42, 668

Asplund, M., Grevesse, N., & Sauval, A. J. 2005, Cosmic Abundances as Records of Stellar Evolution and Nucleosynthesis, 336, 25

Awaki, H., Terashima, Y., Hayashida, K., & Sakano, M. 2001, PASJ, 53, 647

Bauer, F. E., Arévalo, P., Walton, D. J., et al. 2015, ApJ, 812, 116

Baldwin, J. A., Wilson, A. S., & Whittle, M. 1987, ApJ, 319, 84

Barvainis, R. 1987, ApJ, 320, 537

Binney, J., & Merrifield, M. 1998, Galactic astronomy / James Binney and Michael Merrifield. Princeton, NJ : Princeton University Press, 1998. (Princeton series in astrophysics) QB857 .B522 1998 ($35.00), Bland-Hawthorn, J., Gallimore, J. F., Tacconi, L. J., et al. 1997, APSS, 248, 9

Blustin, A. J., Page, M. J., Fuerst, S. V., Branduardi-Raymont, G., & Ashton, C. E. 2005, AAP, 431, 111

Bonatto, C. J., & Pastoriza, M. G. 1997, ApJ, 486, 132

Bottorff, M. C., Korista, K. T., & Shlosman, I. 2000, ApJ, 537, 134

Bowen, I. S. 1927, PASP, 39, 295

Brinkman, A. C., Kaastra, J. S., van der Meer, R. L. J., et al. 2002, AAP, 396, 761

Bruhweiler, F. C., Miskey, C. L., Smith, A. M., Landsman, W., & Malumuth, E. 2001, ApJ, 546, 866

Burke, B. E., Mountain, R. W., Daniels, P. J., Cooper, M. J., & Dolat, V. S. 1993, procspie, 2006, 272

Capetti, A., Axon, D. J., & Macchetto, F. D. 1997, ApJ, 487, 560

Canizares, C. R., Davis, J. E., Dewey, D., et al. 2005, PASP, 117, 1144

Carigi, L., Peimbert, M., Esteban, C., & García-Rojas, J. 2005, ApJ, 623, 213

Cecil, G., Bland, J., & Tully, R. B. 1990, ApJ, 355, 70

Colbert, E. J. M., Weaver, K. A., Krolik, J. H., Mulchaey, J. S., & Mushotzky, R. F. 2002, ApJ, 581, 182

Crenshaw, D. M., & Kraemer, S. B. 2000, ApJ, 532, L101

Crenshaw, D. M., & Kraemer, S. B. 2000, ApJ, 532, L101

Crenshaw, D. M., Kraemer, S. B., Schmitt, H. R., et al. 2010, ApJ, 139, 871

Crenshaw, D. M., & Kraemer, S. B. 2012, ApJ, 753, 75

Crenshaw, D. M., Kraemer, S. B., & George, I. M. 2003, ARAA, 41, 117

Crenshaw, D. M., Schmitt, H. R., Kraemer, S. B., Mushotzky, R. F., & Dunn, J. P. 2010, ApJ, 708, 419

Crenshaw, D. M., Kraemer, S. B., Schmitt, H. R., et al. 2010, AJ, 139, 871

Das, V., Crenshaw, D. M., Kraemer, S. B., & Deo, R. P. 2006, AJ, 132, 620

Das, V., Crenshaw, D. M., & Kraemer, S. B. 2007, ApJ, 656, 699

Dickey, J. M., & Lockman, F. J. 1990, ARAA, 28, 215

Dopita, M. A., & Sutherland, R. S. 2003, Astrophysics of the diffuse universe, Berlin, New York: Springer, 2003. Astronomy and astrophysics library, ISBN 3540433627,

Edelson, R. A., Alexander, T., Crenshaw, D. M., et al. 1996, ApJ, 470, 364

Edelson, R., & Nandra, K. 1999, ApJ, 514, 682

Elitzur, M. 2005, arXiv:astro-ph/0512025

Elitzur, M., Kimball, A. E., Ivezic, Z., & Nenkova, M. 2006, Bulletin of the American Astronomical Society, 38, #149.08

Emmering, R. T., Blandford, R. D., & Shlosman, I. 1992, ApJ, 385, 460

Esteban, C., García-Rojas, J., Peimbert, M., et al. 2005, ApJl, 618, L95

Evans, I. N., Ford, H. C., Kinney, A. L., et al. 1991, apjl, 369, L27

Everett, J. E., & Murray, N. 2007, apj, 656, 93

Fabian, A. C., Kunieda, H., Inoue, S., et al. 1994, PASJ, 46, L59

Fabian, A. C., Iwasawa, K., Reynolds, C. S., & Young, A. J. 2000, PASP, 112, 1145

Fath, E. A. 1909, Popular Astronomy, 17, 504

Ferland, G. J., Korista, K. T., Verner, D. A., et al. 1998, PASP, 110, 761

Ferland, G. J., Porter, R. L., van Hoof, P. A. M., et al. 2013, RMXAA, 49, 137

Ferrarese, L., & Ford, H. 2005, ssr, 116, 523

Forman, W., Jones, C., Cominsky, L., et al. 1978, ApJS, 38, 357

Friedman, H., Lichtman, S. W., & Byram, E. T. 1951, Physical Review, 83, 1025

Gabriel, A. H., & Jordan, C. 1969, MNRAS, 145, 241

Gallimore, J. F., Baum, S. A., O'Dea, C. P., Brinks, E., & Pedlar, A. 1994, ApJl, 422, L13

Gallimore, J. F., Axon, D. J., O'Dea, C. P., Baum, S. A., & Pedlar, A. 2006, AJ, 132, 546

George, I. M., & Fabian, A. C. 1991, MNRAS, 249, 352

George, I. M., Turner, T. J., Netzer, H., et al. 1998, ApJS, 114, 73

Giacconi, R., Gursky, H., Paolini, F. R., & Rossi, B. B. 1962, Physical Review Letters, 9, 439

Giacconi, R., Gursky, H., Paolini, F. R., & Rossi, B. B. 1962, Physical Review Letters, 9, 439

Gondoin, P., Barr, P., Lumb, D., et al. 2001, AAP, 378, 806

Goodman, J., & Lee, H. M. 1989, ApJ, 337, 84

Green, A. R., McHardy, I. M., & Lehto, H. J. 1993, MNRAS, 265, 664

Greenhill, L. J., & Gwinn, C. R. 1997, APSS, 248, 261

Grevesse, N., & Sauval, A. J. 1998, SSR, 85, 161

Grimes, J. P., Kriss, G. A., & Espey, B. R. 1999, ApJj, 526, 130

Halpern, J. P. 1984, ApJ, 281, 90

Harrison, F. A., Craig, W. W., Christensen, F. E., et al. 2013, ApJ, 770, 103

Helfer, T. T., & Blitz, L. 1995, ApJ, 450, 90

Henry, R. B. C., Edmunds, M. G., K&oumlppen, J. 2000, ApJ, 541, 660

Hinshaw, G., Weiland, J. L., Hill, R. S., et al. 2009, ApJS, 180, 225

Ho, L., Kormendy, J., & Murdin, P. 2000, Encyclopedia of Astronomy and Astrophysics, 2365

Holweger, H. 2001, Joint SOHO/ACE workshop "Solar and Galactic Composition", 598, 23

Hönig, S. F., & Beckert, T. 2007, MNRAS, 380, 1172

Hubble, E. P. 1926, ApJ, 64, 321

Huchra, J. P., Vogeley, M. S., & Geller, M. J. 1999, VizieR Online Data Catalog, 212, 10287

Inoue, H., & Matsumoto, C. 2003, PASJ, 55, 625

Iwasawa, K., Fabian, A. C., & Matt, G. 1997, MNRAS, 289, 443

Jaffe, W., Meisenheimer, K., Röttgering, H., Leinert, C., & Richichi, A. 2004, The Interplay Among Black Holes, Stars and ISM in Galactic Nuclei, 222, 37

Jogee, S. 2006, Physics of Active Galactic Nuclei at all Scales, 693, 143

Kalberla, P. M. W., Burton, W. B., Hartmann, D., et al. 2005, AAP, 440, 775

Kallman, T. R., Palmeri, P., Bautista, M. A., Mendoza, C., & Krolik, J. H. 2004, ApJS, 155, 675

Kallman, T., Evans, D. A., Marshall, H., et al. 2014, ApJ, 780, 121

Kinkhabwala, A., Sako, M., Behar, E., et al. 2002, ApJ, 575, 732

Konigl, A., & Kartje, J. F. 1994, ApJ, 434, 446

Kormendy, J. 1979, ApJ, 227, 714

Kormendy, J. 1982, ApJ, 257, 75

Kormendy, J., & Richstone, D. 1995, ARAA, 33, 581

Koyama, K., Inoue, H., Tanaka, Y., et al. 1989, PASJ, 41, 731

Koyama, K., Tsunemi, H., Dotani, T., et al. 2007, PASJ, 59, 23

Koski, A. T. 1978, ApJ, 223, 56

Kraemer, S. B., Ruiz, J. R., & Crenshaw, D. M. 1998, ApJ, 508, 232

Kraemer, S. B., & Crenshaw, D. M. 2000, ApJ, 544, 763

Kraemer, S. B., & Crenshaw, D. M. 2000, ApJ, 532, 256

Kraemer, S. B., Schmitt, H. R., Crenshaw, D. M., et al. 2011, ApJ, 727, 130

Kraemer, S. B., Sharma, N., Turner, T. J., George, I. M., & Crenshaw, D. M. 2015, ApJ, 798, 53

Kriss, G. A., Davidsen, A. F., Blair, W. P., Ferguson, H. C., & Long, K. S. 1992, ApJl, 394, L37

Kraemer, S. B., Sharma, N., Turner, T. J., George, I. M., & Crenshaw, D. M. 2015, ApJ, 798, 53

Krolik, J. H. 1999, Active galactic nuclei : from the central black hole to the galactic environment /Julian H. Krolik. Princeton, N. J. : Princeton University Press, c1999.,

Krolik, J. H., & Kriss, G. A. 2001, ApJ, 561, 684

Lutz, D., Sturm, E., Genzel, R., et al. 2000, ApJ, 536, 697

Lightman, A. P., & White, T. R. 1988, ApJ, 335, 57

Magdziarz, P., & Zdziarski, A. A. 1997, X-Ray Imaging and Spectroscopy of Cosmic Hot Plasmas, 617

Maiolino, R., & Rieke, G. H. 1995, ApJ, 454, 95

Mathis, J. S., Rumpl, W., & Nordsieck, K. H. 1977, ApJ, 217, 425

Matt, G., Guainazzi, M., Frontera, F., et al. 1997, AAP, 325, L13

Melendez, M., Kraemer, S. B., Deo, R. P., et al. 2007, Bulletin of the American Astronomical Society, 39, 854

Murphy, K. D., & Yaqoob, T. 2009, MNRAS, 397, 1549

Nandra, K., O'Neill, P. M., George, I. M., & Reeves, J. N. 2007, MNRAS, 382, 194

Nenkova, M., Ivezić, Ž., & Elitzur, M. 2002, ApJl, 570, L9

Netzer, H., & Peterson, B. M. 1997, Astronomical Time Series, 218, 85

Maeder, A., & Meynet, G. 1989, AAP, 210, 155

Marinucci, A., Bianchi, S., Matt, G., et al. 2016, MNRAS, 456, L94

Meléndez, M., Kraemer, S. B., Armentrout, B. K., et al. 2008, ApJ, 682, 94

Miller, J. S., Goodrich, R. W., & Mathews, W. G. 1991, ApJ, 378, 47

Miller, J. S., & Antonucci, R. R. J. 1983, ApJl, 271, L7

Mihara, T., Matsuoka, M., Mushotzky, R. F., et al. 1994, PASJ, 46, L137

Nandra, K., & Pounds, K. A. 1992, NAT, 359, 215

Nandra, K., Fabian, A. C., George, I. M., et al. 1993, MNRAS, 260, 504

Netzer, H. 1993, ApJ, 411, 594

Netzer, H. 1996, ApJ, 473, 781

Ogle, P. M., Brookings, T., Canizares, C. R., Lee, J. C., & Marshall, H. L. 2003, AAP, 402, 849

Ogle, P. M., Marshall, H. L., Lee, J. C., & Canizares, C. R. 2000, apjl, 545, L81

Orr, A., Molendi, S., Fiore, F., et al. 1997, AAP, 324, L77

Osterbrock, D. E. 1985, Astrophysics of Active Galaxies and Quasi-Stellar Objects, 111

Otani, C., Kii, T., Reynolds, C. S., et al. 1996, PASJ, 48, 211

Palmeri, P., Mendoza, C., Kallman, T. R., Bautista, M. A., & Meléndez, M. 2003, aap, 410, 359

Peimbert, M. 1967, ApJ, 150, 825

Peterson, B. M., Ferrarese, L., Gilbert, K. M., et al. 2004, ApJ, 613, 682

Pier, E. A., Antonucci, R., Hurt, T., Kriss, G., & Krolik, J. 1994, ApJ, 428, 124

Planesas, P., Scoville, N., & Myers, S. T. 1991, ApJ, 369, 364

Pogge, R. W. 1988, ApJ, 328, 519

Porquet, D., & Dubau, J. 2002, SF2A-2002: Semaine de l'Astrophysique Francaise, 371

Porter, R. L., Ferland, G. J., Kraemer, S. B., et al. 2006, PASP, 118, 920

Pounds, K. A., Nandra, K., Fink, H. H., & Makino, F. 1994, MNRAS, 267, 193

Ptak, A., Yaqoob, T., Serlemitsos, P. J., Mushotzky, R., & Otani, C. 1994, APJl, 436, L31

Reynolds, C. S. 1997, MNRAS, 286, 513

Reeves, J. N., Nandra, K., George, I. M., et al. 2004, ApJ, 602, 648

Riffel, R. A., Vale, T. B., Storchi-Bergmann, T., & McGregor, P. J. 2014, MNRAS, 442, 656

Remillard, R. A., Bradt, H. V. D., Brissenden, R. J. V., et al. 1993, AJ, 105, 2079

Stirpe, G. M., Winge, C., Altieri, B., et al. 1994, ApJ, 425, 609

Schödel, R., Ott, T., Genzel, R., et al. 2002, NAT, 419, 694

Seaton, M. J. 1978, MNRAS, 185, 5P

Seaton, M. J. 1979, MNRAS, 187, 73P

Savage, B. D., & Mathis, J. S. 1979, ARAA, 17, 73

Scoville, N. Z., Matthews, K., Carico, D. P., & Sanders, D. B. 1988, ApJl, 327, L61

Seyfert, C. K. 1943, ApJ, 97, 28

Shields, G. A., & Oke, J. B. 1975, ApJ, 197, 5

Shlosman, I., Frank, J., & Begelman, M. C. 1989, NAT, 338, 45

Sofue, Y. 1991, PASJ, 43, 671

Takahashi, T., Mitsuda, K., Kelley, R., et al. 2014, procspie, 9144, 914425

Tombesi, F., Cappi, M., Reeves, J. N., et al. 2010, AAP, 521, A57

Tucker, W., Giacconi, R., & Cordova, F. A. 1985, SKYTEL, 70, 442

Tully, R. B., Rizzi, L., Shaya, E. J., et al. 2009, AJ, 138, 323

Turner, T. J., George, I. M., & Mushotzky, R. F. 1993, ApJ, 412, 72

Turner, T. J., George, I. M., Nandra, K., & Mushotzky, R. F. 1997, ApJS, 113, 23

Turner, T. J., Kraemer, S. B., Mushotzky, R. F., George, I. M.,

Turner, T. J., Kraemer, S. B., George, I. M., Reeves, J. N.,

Turner, T. J., & Miller, L. 2009, AAPR, 17, 47 & Bottorff, M. C. 2005, ApJ, 618, 155

Turner, T. J., & Pounds, K. A. 1989, MNRAS, 240, 833 & Gabel, J. R. 2003, apj, 594, 128

Tucker, W., Kellogg, E., Gursky, H., Giacconi, R., & Tananbaun, H. 1973, ApJ, 180, 715

Walker, M. F. 1968, ApJ, 151, 71

Unger, S. W., Pedlar, A., Axon, D. J., et al. 1987, MNRAS, 228, 671

Wilms, J., Allen, A., & McCray, R. 2000, ApJ, 542, 914

Whittle, M. 1992, ApJS, 79, 49

Wilson, A. S., & Ulvestad, J. S. 1982, ApJ, 263, 576

Yaqoob, T., Serlemitsos, P., Mushotzky, R., et al. 1994, PASJ, 46, L173

Yaqoob, T. 2012, MNRAS, 423, 3360

Young, A. J., Wilson, A. S., & Shopbell, P. L. 2001, ApJ, 556, 6

Yu, Q., & Tremaine, S. 2002, MNRAS, 335, 965